

Charged Loops at the Cosmological Collider with Chemical Potential

Arushi Bodas ^{a,b} **Edward Broadberry** ^c **Raman Sundrum** ^c **Zhaohui Xu**^c

^a*Enrico Fermi Institute, University of Chicago, Chicago, IL 60637, USA*

^b*Particle Theory Department, Fermilab, Batavia, Illinois 60510, USA*

^c*Maryland Center for Fundamental Physics, Department of Physics, University of Maryland, College Park, MD 20742, USA*

E-mail: arushib@uchicago.edu, edbroad@umd.edu, raman@umd.edu,
zhxu1226@umd.edu

ABSTRACT: Cosmological collider physics allows the detection of heavy particles at inflationary scales through their imprints on primordial non-Gaussianities. We study the chemical potential mechanism applied to a pair of charged scalars. We analytically evaluate the resulting one-loop contribution to the bispectrum, using the spectral decomposition. In this way we are able to determine the parametric dependences for both the signal and the background. We show that a signal strength $f_{\text{NL}} \sim \mathcal{O}(0.01)$ can be obtained within theoretical control, potentially reachable by 21 cm tomography. As an application we consider the colored Higgs bosons in SU(5) supersymmetric orbifold grand unification with masses $M \lesssim 10^{15}$ GeV.

Contents

1	Introduction	2
2	Preliminaries	5
2.1	Primordial non-Gaussianity	5
2.2	In-in formalism and mode functions	7
3	Charged-pair Chemical Potential Model and Spectral Decomposition	8
3.1	Chemical potential for a pair of charged scalars	9
3.2	One-loop diagram under spectral representation	10
3.3	Central result for the signal	14
4	Systematic Computation: Tree-level Model Revisited	18
4.1	Perturbative expansion under late-time-finite basis	18
4.2	Contributions from B_{-+}	21
4.3	Contributions from B_{++}	24
5	Systematic Computation: One-loop Model	26
5.1	Signal from the threshold limit	26
5.2	Resonance backgrounds	29
5.3	Beyond stationary phase approximation	32
5.4	Combinatorial backgrounds from permuted diagrams	36
5.5	Higher order corrections at one-loop	38
6	Signal Size and Constraints	42
7	Application: Colored Higgs in SUSY Orbifold GUTs	46
7.1	SUSY inflation and the fifth dimension	46
7.2	Realizing the chemical potential	49
8	Discussion and Conclusions	51
A	Integrals and Identities Involving Special Functions	52
B	Asymptotic Expansions of $\tilde{\mathbf{F}}_{i\mu}^s(p)$	53
C	Spectral Density in Non-relativistic Limit of de Sitter Spacetime	54
D	Exact Form of $B_{++,A}$	56
E	Full Evaluation of the One-loop Model	59

1 Introduction

Heavy particles produced on-shell during inflation, if they decay into inflatons, could have imprinted themselves on cosmological observables such as the Cosmic Microwave Background (CMB) and Large Scale Structure (LSS) [1–6]. The mechanism, dubbed *cosmological collider physics*, offers an alternative approach to search for new particles. Compared to terrestrial colliders at the TeV-scale, the “cosmological collider” probes inflationary energy scales, possibly as high as $\sim 10^{14}$ GeV. Therefore, with increasing sensitivity from upcoming LSS experiments [7–12] and future 21 cm tomography [13–15], there is a possibility to detect heavy particles far beyond the reach of upcoming colliders.

In the minimal version of cosmological collider physics particles are created by the expansion of spacetime, characterized by the inflationary Hubble energy scale, H . During inflation, this could be as large as [16]

$$H < 2.5 \times 10^{-5} M_{\text{pl}} \approx 6 \times 10^{13} \text{ GeV}. \quad (1.1)$$

If the heavy particles can decay into inflatons, they will give the following non-zero contribution to the non-Gaussianity (NG) in the 3-point correlator of the comoving curvature perturbation, \mathcal{R} , [1, 3, 5]

$$\frac{\langle \mathcal{R}_{\mathbf{k}_1} \mathcal{R}_{\mathbf{k}_2} \mathcal{R}_{\mathbf{k}_3} \rangle'}{\langle \mathcal{R}_{\mathbf{k}_1} \mathcal{R}_{-\mathbf{k}_1} \rangle' \langle \mathcal{R}_{\mathbf{k}_3} \mathcal{R}_{-\mathbf{k}_3} \rangle'} \sim e^{-\pi\mu} \left(\frac{k_3}{k_1} \right)^{-3/2-i\mu} + \text{c.c.}, \quad \mu := \sqrt{\frac{M^2}{H^2} - \frac{9}{4}}, \quad (1.2)$$

in the squeezed limit, $k_1 \sim k_2 \gg k_3$. Depending on the value of the heavy mass M , this signal can be either oscillatory ($M > 3H/2$), or a fractional power-law ($M < 3H/2$). Both behaviors, especially the oscillatory one, cannot be mimicked by local contact interactions of inflatons, and can serve as strong evidence for particle production.

Despite the exciting opportunity in this direction, eq. (1.2) contains an exponential suppression $e^{-\pi\mu}$ for $M > 3H/2$, which leads to a very narrow observable mass window for oscillatory signals. Fortunately, this suppression can be overcome through an extension of the minimal mechanism, where the kinetic energy of the inflaton background can give rise to a *chemical potential* for heavy fields through a dimension-5 coupling [17–24]:

$$\mathcal{L} \supset \frac{1}{\Lambda} \nabla_\mu \phi J^\mu \supset \lambda J^0 \quad (1.3)$$

with the chemical potential defined by $\lambda := \dot{\phi}_0/\Lambda$, and J^μ is a non-conserved current made from the heavy fields. In order to maintain in effective field theory control, Λ^2 is required to

be larger than $\dot{\phi}_0$, i.e. the chemical potential is bounded by $\lambda < \sqrt{\dot{\phi}_0}$ where [16]

$$\dot{\phi}_0 \approx (60H)^2. \quad (1.4)$$

The chemical potential leads to unsuppressed particle production for all fields in J whose masses, $M < \lambda$. This can greatly widen the mass window for oscillatory signatures. The simplest signals of this type, both theoretically and phenomenologically, appear at tree-level, and have been explored in ref. [22, 24].

Loop level processes for cosmological correlators are poorly understood, because we usually lack the theoretical control required to calculate them. However, since the inflatons on the external legs are neutral, one-loop processes can be important because particles with non-trivial quantum numbers must be produced and annihilated in pairs. Consequently, including one-loop effects can broaden the range of new physics targets to include charged particles and fermions.

There have been several efforts towards computing loops during inflation:

- Rough estimates based on “loop factors \times propagators \times vertices” have been accomplished in [18, 20–22]. There are also approximate one-loop calculations based on a late-time expansion of propagators in [20, 25]. Nonetheless, as mentioned in [20], these results cannot predict the extra parametric dependence on the chemical potential, λ , and the particles masses coming from the loop integrals.
- In [26], a numerical calculation of a one-loop process was performed. It is found that the brute-force method is time-consuming because of the high dimensionality and the oscillatory nature of the integrand. Furthermore, the underlying physics is less clear than in an analytic calculation.
- There are also analytic results in [27–31]. In particular, ref. [27, 30] applied the *spectral decomposition* technique to one-loop corrections to the power spectrum, while ref. [29] further applied this to a particular one-loop contribution to the bispectrum without chemical potential, reducing it to a one-dimensional integral over the invariant mass or a sum over residues. However, most models will also produce triangle diagrams which cannot be captured by spectral decomposition, a problem which has not so far been addressed. Compared to the numerical approach, this method relies on de Sitter isometry, which is broken down to scale invariance by the inflaton background.

In this paper we evaluate the 3-point correlator in a model where the chemical potential effect is perturbative, such that we can still take advantage of the de Sitter isometry. Furthermore, in this particular model all leading order effects can be computed using the spectral representation.

It turns out that in the limit of heavy particles with a large chemical potential, the signal size from the loop process has a surprisingly simple form: for two scalars with masses M_1 ,

M_2 , the amplitude for the 3-point function is related to the amplitude that one would obtain from the tree level exchange of a single scalar by

$$\begin{aligned} \langle \mathcal{R}_{\mathbf{k}_1} \mathcal{R}_{\mathbf{k}_2} \mathcal{R}_{\mathbf{k}_3} \rangle'_{1\text{-loop,signal}} &\simeq \frac{e^{3\pi i/4}}{2\pi^{3/2}} \sqrt{\frac{M_1 M_2}{M_{12}}} \left(\frac{2M_{12}}{\lambda + M_{12}} \frac{2k_3}{k_1} \right)^{-3/2} \\ &\times \langle \mathcal{R}_{\mathbf{k}_1} \mathcal{R}_{\mathbf{k}_2} \mathcal{R}_{\mathbf{k}_3} \rangle'_{\text{tree}}|_{M=M_{12}} \end{aligned} \quad (1.5)$$

in the squeezed limit, where $M_{12} := M_1 + M_2$ and λ is the chemical potential. A quick derivation of this relation is given in section 3.3. In addition to an oscillatory signal, the model predicts the existence of a smooth background. We also evaluate the analytic background, showing that it comes from the resonance limit in the corresponding effective tree-level model. By obtaining the correct parametric dependence on both the chemical potential and the masses, we remove one obstacle for future phenomenological studies in this direction.

As a phenomenological application we consider the prospect of detecting the colored Higgs of supersymmetric SU(5) orbifold grand unification. The framework of grand unification is a well motivated scenario for physics beyond the standard model. In GUTs there exist new particles with masses around the scales that cosmological collider physics can probe [32–34]. However, the simple models of grand unification are in tension with proton decay bounds, which can be avoided in the higher dimensional “orbifold GUTs” [35–37]. The cosmological collider signatures of orbifold GUTs have been investigated in [24, 38], while the idea of detecting supersymmetry in general has been considered in [39, 40]. In ref. [24], the authors also considered the signal from an orbifold SUSY GUT with a chemical potential. However, they looked at tree level exchanges, which require the heavy particle to be neutral. This is not possible at tree level with the simple SU(5) gauge group, but required more exotic grand unification, e.g. trinification. The fact that we can calculate a loop level process allows us to consider the simpler SU(5) gauge group. We find that the one-loop signal could be within the sensitivity of future 21 cm experiments.

The rest of the paper is organized as follows. In section 2, we introduce our notation and review the necessary background. Section 3 elaborates on the implementation of a chemical potential and the method of spectral representation, which is crucial for evaluating loop diagrams involving a pair of charged scalars. We also present an intuitive calculation of the non-analytic part of the bispectrum, which constitutes the cosmological collider signal. sections 4 and 5 then provide a more systematic evaluation of both the non-analytic contribution and the smooth analytic background. In section 6, we analyze theoretical and observational constraints and estimate the maximum signal strength achievable. As a concrete application of our chemical potential model, we assess the detectability of the colored Higgs bosons predicted by the SU(5) orbifold SUSY GUT model in section 7. We conclude with a discussion of future directions in section 8. The appendices contain supplementary material relevant to our calculations.

2 Preliminaries

In this section, we define our notation and briefly review the in-in formalism for cosmological correlators. The mostly plus signature $(-, +, +, +)$ for the metric is used throughout this paper.

2.1 Primordial non-Gaussianity

During slow-roll inflation the spacetime is approximately described by the de Sitter metric:

$$\begin{aligned} ds^2 &= -dt^2 + e^{2Ht} d\mathbf{x}^2, \\ &= \frac{-d\eta^2 + d\mathbf{x}^2}{H^2\eta^2}, \end{aligned} \quad (2.1)$$

where t is the proper time, H is the Hubble parameter during inflation and $\eta = -e^{-Ht}/H$ is the conformal time.

Inflation is usually realized by a scalar field ϕ called the “inflaton”. It can be decomposed into a homogeneous classical background, ϕ_0 , that controls the inflation dynamics, plus a quantum fluctuation, $\delta\phi$, that is responsible for the primordial fluctuations after inflation. In the spatially flat gauge, $\delta\phi$ is related to the gauge-invariant comoving curvature perturbation, \mathcal{R} , by [41]

$$\mathcal{R} = -H \frac{\delta\phi}{\dot{\phi}_0} \quad (2.2)$$

with the overdot representing the derivatives with respect to the proper time t . Since the inflationary dynamics is invariant under spatial translation, any momentum-space correlators contain a total-momentum δ -function:

$$\langle \mathcal{R}_{\mathbf{k}_1} \mathcal{R}_{\mathbf{k}_2} \cdots \mathcal{R}_{\mathbf{k}_n} \rangle = (2\pi)^3 \delta(\mathbf{k}_1 + \mathbf{k}_2 + \cdots + \mathbf{k}_n) \cdot \langle \mathcal{R}_{\mathbf{k}_1} \mathcal{R}_{\mathbf{k}_2} \cdots \mathcal{R}_{\mathbf{k}_n} \rangle'. \quad (2.3)$$

Starting from the 2-point correlation function, current CMB data favors a nearly scale-invariant primordial power spectrum given by

$$\mathcal{P}_{\mathcal{R}}(k) := \langle \mathcal{R}_{\mathbf{k}} \mathcal{R}_{-\mathbf{k}} \rangle' = \frac{H^4}{2\dot{\phi}_0^2 k^3} \left(\frac{k}{k_*} \right)^{n_s-1}. \quad (2.4)$$

The scalar spectral index, n_s , has been measured to be around 0.96 at the reference comoving momentum scale, $k_* \approx 0.05 \text{ Mpc}^{-1}$. In this paper, we assume exact scale invariance during inflation as an approximation i.e. we will treat H and $\dot{\phi}_0$ as constants. From now on we work in units with $H = 1$ in all equations unless stated otherwise. Note that with these two assumptions, the *spacetime scale transformation*:

$$\eta, \mathbf{x} \mapsto \lambda\eta, \lambda\mathbf{x} \quad (2.5)$$

remains to be a good symmetry.

While scale invariance forces $\mathcal{P}_{\mathcal{R}}(k)$ to be proportional to $1/2k^3$, higher-point correlation functions, such as the primordial bispectrum $\langle \mathcal{R}_{\mathbf{k}_1} \mathcal{R}_{\mathbf{k}_2} \mathcal{R}_{\mathbf{k}_3} \rangle'$, may contain more intricate momentum dependence. The bispectrum is conventionally normalized relative to the size of the power spectrum in defining the NG as [42]

$$\begin{aligned} F(k_1, k_2, k_3) &:= \frac{5}{6} \frac{\langle \mathcal{R}_{\mathbf{k}_1} \mathcal{R}_{\mathbf{k}_2} \mathcal{R}_{\mathbf{k}_3} \rangle'}{\mathcal{P}_{\mathcal{R}}(k_1)\mathcal{P}_{\mathcal{R}}(k_2) + \mathcal{P}_{\mathcal{R}}(k_2)\mathcal{P}_{\mathcal{R}}(k_3) + \mathcal{P}_{\mathcal{R}}(k_3)\mathcal{P}_{\mathcal{R}}(k_1)} \\ &= -\frac{10}{3} \dot{\phi}_0 \cdot \frac{k_1^3 k_2^3 k_3^3}{k_1^3 + k_2^3 + k_3^3} B(k_1, k_2, k_3), \end{aligned} \quad (2.6)$$

where $B(k_1, k_2, k_3) = \langle \delta\phi_{\mathbf{k}_1} \delta\phi_{\mathbf{k}_2} \delta\phi_{\mathbf{k}_3} \rangle'$ is the 3-point correlator of the inflaton fluctuations. The current bound from Planck on the 3-point correlator in the equilateral configuration [43] is

$$f_{\text{NL}} := F(k, k, k) \lesssim \mathcal{O}(10), \quad (2.7)$$

where the detailed value depends on the shape of the NG. Meanwhile, future LSS experiments are expected to be able to probe these signals at $f_{\text{NL}} \sim \mathcal{O}(1)$ [7], and more futuristic 21 cm tomography can further bring this precision down to $f_{\text{NL}} \sim \mathcal{O}(0.01)$ [13–15].

The characteristic cosmological collider signal appears in the squeezed limit $k_1 \sim k_2 \gg k_3$. We define the squeezing parameter p and the angle parameter χ to characterize the shape of the squeezed triangle up to similarity as follows:

$$p := \frac{k_1 + k_2}{k_3}, \quad \chi := \frac{k_1 - k_2}{k_3}. \quad (2.8)$$

The corresponding momentum triangle is illustrated in figure 1. In the limit $p \gg 1$, $\chi =$

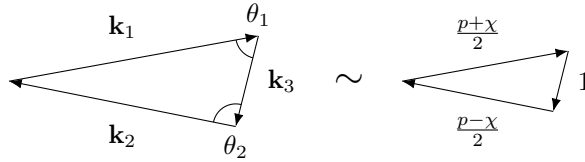


Figure 1. The shape of the momentum triangle and the two parameters. In the squeezed limit $p \gg 1$, the angle parameter $\chi \simeq \cos \theta_1 \simeq -\cos \theta_2$.

$\cos \theta_1 + \mathcal{O}(p^{-1}) = -\cos \theta_2 + \mathcal{O}(p^{-1})$, whereas triangular inequality implies $p \geq 1$ and $|\chi| \leq 1$ regardless of whether the squeezed limit is taken. Under the (p, χ) parametrization, eq. (2.6) becomes

$$\begin{aligned} F(k_1, k_2, k_3) &= -\frac{10}{3} \dot{\phi}_0 \cdot \frac{4}{p^3 + 3\chi^2 p + 4} \cdot k_1^3 k_2^3 B(\mathbf{k}_1, \mathbf{k}_2, \mathbf{k}_3) \\ &\xrightarrow{p \rightarrow \infty} -\frac{40}{3} \dot{\phi}_0 \cdot p^{-3} \cdot k_1^3 k_2^3 B(\mathbf{k}_1, \mathbf{k}_2, \mathbf{k}_3). \end{aligned} \quad (2.9)$$

Since the angular dependence does not play a significant role in scalar models, $\chi = 0$ is

illustrated in all the plots unless otherwise stated.

2.2 In-in formalism and mode functions

In inflationary cosmology, we are mostly interested in the *in-in* correlators, i.e., the expectation values of operators at a specific time (t_0) in the vacuum state [44]:

$$\langle \Omega_- | \mathcal{O}_H(t_0) | \Omega_- \rangle = \langle 0 | \left(\bar{T} e^{i \int_{-\infty+}^{t_0} H_{\text{int}}(t) dt} \right) \mathcal{O}_I(t_0) \left(T e^{-i \int_{-\infty-}^{t_0} H_{\text{int}}(t) dt} \right) | 0 \rangle, \quad (2.10)$$

where $\infty_{\pm} := \infty(1 \pm i\epsilon)$ contains the $i\epsilon$ -prescription, which we leave implicit in all expressions henceforth, and T (\bar{T}) represents time (anti-time) ordering. This differs from the usual in-out correlators by having the anti-time ordered exponential. After expanding the two exponentials in power, one can evaluate in-in correlators using ordinary Feynman rules with two sets of vertices from the time ordered exponential (denoted as $+$) and the anti-time ordered exponential (denoted as $-$) respectively. Meanwhile, depending on the types of vertices connected in eq. (2.10), there are four sets of propagators:

$$\begin{aligned} G_{++}(t_1, t_2) &:= \langle 0 | T[\phi(t_1)\phi(t_2)] | 0 \rangle, \\ G_{--}(t_1, t_2) &:= \langle 0 | \bar{T}[\phi(t_1)\phi(t_2)] | 0 \rangle, \\ G_{-+}(t_1, t_2) &:= \langle 0 | \phi(t_1)\phi(t_2) | 0 \rangle, \\ G_{+-}(t_1, t_2) &:= \langle 0 | \phi(t_2)\phi(t_1) | 0 \rangle. \end{aligned} \quad (2.11)$$

The G_{++} propagator is identical to the Feynman propagator in the usual in-out formalism, while other propagators are either its hermitian conjugate (G_{--}) or can be obtained from its analytic continuation (G_{-+} and G_{+-}).

In de Sitter spacetime it is simpler to work with conformal time, η , and comoving spatial momentum. To calculate the matrix elements in eq. (2.11) for scalar fields, we represent the scalar field operator in terms of creation and annihilation operators as

$$\phi(\mathbf{k}, \eta) = f_k(\eta) a_{\mathbf{k}} + \bar{f}_k(\eta) a_{-\mathbf{k}}^{\dagger}, \quad [a_{\mathbf{k}'}, a_{\mathbf{k}}^{\dagger}] = (2\pi)^3 \delta^3(\mathbf{k}' - \mathbf{k}), \quad (2.12)$$

where the mode function $f_k(\eta)$ is a normalized solution to the free field equation

$$\begin{cases} \left(\partial_{\eta}^2 - \frac{2}{\eta} \partial_{\eta} + k^2 + \frac{M^2}{\eta^2} \right) f_k = 0, \\ -i(f_k \partial_{\eta} \bar{f}_k - \bar{f}_k \partial_{\eta} f_k) = \eta^2. \end{cases} \quad (2.13)$$

With this representation, the four propagators in eq. (2.11) are given by

$$\begin{aligned}
G_{++}(k, \eta_1, \eta_2) &:= f_k(\eta_1) \bar{f}_k(\eta_2) \theta(\eta_1 - \eta_2) + \bar{f}_k(\eta_1) f_k(\eta_2) \theta(\eta_2 - \eta_1), \\
G_{--}(k, \eta_1, \eta_2) &:= \bar{f}_k(\eta_1) f_k(\eta_2) \theta(\eta_1 - \eta_2) + f_k(\eta_1) \bar{f}_k(\eta_2) \theta(\eta_2 - \eta_1), \\
G_{-+}(k, \eta_1, \eta_2) &:= f_k(\eta_1) \bar{f}_k(\eta_2), \\
G_{+-}(k, \eta_1, \eta_2) &:= \bar{f}_k(\eta_1) f_k(\eta_2),
\end{aligned} \tag{2.14}$$

where θ is the Heaviside step function. To fix the solution, we must further impose the *Bunch-Davies* initial condition at $\eta \rightarrow -\infty$:

$$f_k(\eta) \sim e^{-ik\eta}, \quad \eta \rightarrow -\infty. \tag{2.15}$$

This choice ensures that the spacetime contains no particles in the infinite past. The solution to eq. (2.13) is then given by

$$f_k(\eta) = \sqrt{\frac{\pi}{4}} e^{\pi i/4 - \pi \mu/2} (-\eta)^{3/2} H_{i\mu}^{(1)}(-k\eta), \tag{2.16}$$

where $H^{(1)}$ is the Hankel function of first kind and μ is the de Sitter mass parameter defined by

$$i\mu := \begin{cases} i\sqrt{M^2 - \frac{9}{4}}, & M > 3/2, \\ \sqrt{\frac{9}{4} - M^2}, & M < 3/2. \end{cases} \tag{2.17}$$

In the special case of the inflaton, we have $M = 0$ and

$$f_k(\eta) = \frac{i}{\sqrt{2k^3}} (1 + ik\eta) e^{-ik\eta}. \tag{2.18}$$

The primordial fluctuations are measured at the end of inflation, i.e., $\eta \rightarrow 0$, so we also need the bulk-to-boundary propagators for the inflaton:

$$D_{\pm}(k, \eta) := G_{+\pm}(k, 0, \eta) = \frac{1}{2k^3} (1 \mp ik\eta) e^{\pm ik\eta}. \tag{2.19}$$

In particular, the leading-order inflaton power spectrum is given by

$$\mathcal{P}_{\phi}(k) := \langle \delta\phi_{\mathbf{k}} \delta\phi_{-\mathbf{k}} \rangle' = D_+(k, 0) = \frac{1}{2k^3}. \tag{2.20}$$

3 Charged-pair Chemical Potential Model and Spectral Decomposition

In this section we construct a model for a pair of complex scalars (χ_1 and χ_2) with a chemical potential, and opposite charges under all symmetry groups. We then derive the Källén-

Lehmann representation for the 3-point correlation function, and discuss some features of the spectral density.

3.1 Chemical potential for a pair of charged scalars

For two complex scalar fields, χ_1 , and, χ_2 , a chemical potential-like coupling is achieved by coupling their U(1) currents to the derivative of the inflaton field, ϕ , as follows [22]:

$$\mathcal{L} \supset \sum_{I=1,2} \frac{1}{2\Lambda} \nabla_\mu \phi J_I^\mu, \quad J_I^\mu := i(\bar{\chi}_I \nabla^\mu \chi_I - \chi_I \nabla^\mu \bar{\chi}_I). \quad (3.1)$$

After plugging in the classical background, ϕ_0 , the Lagrangian density contains a term $\frac{\lambda}{2} J_0$ for each field, giving a chemical potential difference of

$$\lambda := \frac{\dot{\phi}_0}{\Lambda}, \quad (3.2)$$

between χ_1, χ_2 and their conjugates $\bar{\chi}_1, \bar{\chi}_2$. An alternative way to write the chemical potential of eq. (3.1) is through the following Lagrangian:

$$\begin{aligned} \mathcal{L}_\chi &\supset - \sum_{I=1,2} \left[\left(\nabla^\mu + i \frac{\nabla^\mu \phi}{2\Lambda} \right) \bar{\chi}_I \left(\nabla_\mu - i \frac{\nabla_\mu \phi}{2\Lambda} \right) \chi_I + M_I^2 |\chi_I|^2 \right] \\ &= - \sum_{I=1,2} \left[|\nabla \chi_I|^2 + M_I^2 |\chi_I|^2 - \frac{1}{2\Lambda} \nabla_\mu \phi J_I^\mu + \frac{1}{4\Lambda^2} (\nabla \phi)^2 |\chi_I|^2 \right], \end{aligned} \quad (3.3)$$

which gives the same dimension-5 interaction up to a dimension-6 coupling.

In the form of eq. (3.3), it is clear that the chemical potential has no nontrivial effect if the full theory is invariant under the following U(1)_A symmetry:

$$\text{U}(1)_A : \quad \chi_1 \rightarrow \chi_1 e^{i\theta}, \quad \chi_2 \rightarrow \chi_2 e^{i\theta}. \quad (3.4)$$

In this case a field redefinition $\chi_I \rightarrow \chi_I e^{i\phi/2\Lambda}$ could eliminate the chemical potential term, while leaving any non-derivative couplings of χ_I invariant. Absent any further symmetry considerations, the lowest dimensional symmetry-breaking term would be a linear term in χ_I , leading to the model discussed in ref. [22], where a heavy particle is exchanged at tree-level. In this paper we will focus on charged scalars, where we assume that χ_1 and χ_2 have opposite charges under all other symmetries. For example if the scalars are also charged under some other U(1)_V, they should transform under its action as¹

$$\text{U}(1)_V : \quad \chi_1 \rightarrow \chi_1 e^{i\theta}, \quad \chi_2 \rightarrow \chi_2 e^{-i\theta}. \quad (3.5)$$

¹One can also build a model with $\chi_1 = \chi_2 = \chi$ as a single complex scalar. In this case the same argument applies if χ is odd under a \mathbb{Z}_2 symmetry, or it transforms under a nontrivial real representation of some symmetry group. Equivalently, one can start with two real scalars with the same set of symmetries, in which the U(1)_A breaking term $\alpha \chi^2$ naturally comes from the mass splitting between the two real scalars.

In this case, the lowest dimensional term that breaks $U(1)_A$ is given by $\chi_1\chi_2$ and we arrive at the following Lagrangian:

$$\mathcal{L}_\chi = - \sum_{I=1,2} \left[|\nabla\chi_I|^2 + M_I^2 |\chi_I|^2 - \underbrace{\frac{1}{2\Lambda} \nabla_\mu \phi J_I^\mu}_{\text{chemical potential}} + \frac{1}{4\Lambda^2} (\nabla\phi)^2 |\chi_I|^2 \right] - \underbrace{\alpha\chi_1\chi_2 - \bar{\alpha}\bar{\chi}_1\bar{\chi}_2}_{\text{explicit } U(1)_A}. \quad (3.6)$$

The flatness of the inflaton potential is preserved due to the derivative ϕ couplings.

The role of the explicit $U(1)_A$ breaking term is more apparent after the field redefinition $\chi_I \mapsto \chi_I e^{i\phi/2\Lambda}$, where the Lagrangian in eq. (3.6) becomes

$$\begin{aligned} \mathcal{L}_\chi &= - \sum_{I=1,2} \left(|\nabla\chi_I|^2 + M_I^2 |\chi_I|^2 \right) - \alpha\chi_1\chi_2 e^{i\phi/\Lambda} - \bar{\alpha}\bar{\chi}_1\bar{\chi}_2 e^{-i\phi/\Lambda}, \\ &= - \sum_{I=1,2} \left(|\nabla\chi_I|^2 + M_I^2 |\chi_I|^2 \right) - \alpha\chi_1\chi_2 e^{i\lambda t} e^{i\delta\phi/\Lambda} - \bar{\alpha}\bar{\chi}_1\bar{\chi}_2 e^{-i\lambda t} e^{-i\delta\phi/\Lambda}. \end{aligned} \quad (3.7)$$

The $U(1)_A$ breaking term effectively acts as an external source that injects (extracts) energy of order λ into (from) the system and creates (annihilates) $\chi_1\chi_2$ pairs. The Lagrangian in this basis still contains a shift symmetry for the inflaton:

$$\phi \rightarrow \phi + c, \quad \chi_I \rightarrow \chi_I e^{ic/2\Lambda}. \quad (3.8)$$

This symmetry plays the same role as the original shift symmetry in preserving the flatness of the inflaton potential.

3.2 One-loop diagram under spectral representation

The time-dependent coupling in eq. (3.7) explicitly breaks de Sitter covariance down to scale invariance. However, the breaking effects will remain in control if the mixing, α , can be treated perturbatively. Since $\chi_1\chi_2$ are created and annihilated in pairs, the leading-order contribution to the bispectrum is $\mathcal{O}(\alpha^2)$ at one-loop, as illustrated in figure 2. In the in-in formalism, it is given by

$$\begin{aligned} \langle \delta\phi_{\mathbf{k}_1} \delta\phi_{\mathbf{k}_2} \delta\phi_{\mathbf{k}_3} \rangle &= |\alpha|^2 \sum_{s_1, s_2 = \pm} (-is_1)(-is_2) \int \sqrt{-g_1} d^4x_1 \int \sqrt{-g_2} d^4x_2 (-\eta_1)^{-i\lambda} (-\eta_2)^{i\lambda} \\ &\quad \times \left\langle \delta\phi_{\mathbf{k}_1} \delta\phi_{\mathbf{k}_2} \delta\phi_{\mathbf{k}_3} \cdot e^{i\delta\phi(x_1)/\Lambda} e^{-i\delta\phi(x_2)/\Lambda} \right\rangle_{s_1 s_2} \langle \mathcal{O}(x_1) \bar{\mathcal{O}}(x_2) \rangle_{s_1 s_2}, \end{aligned} \quad (3.9)$$

where $\mathcal{O} = \chi_1\chi_2$ and the two signs $s_1, s_2 = +/-$ indicate whether the vertex comes from the time or anti-time ordered exponential. At leading order, the two correlators of $\delta\phi$ and χ_I can be evaluated as in the free field theory, where the second correlator gives rise to a loop in momentum space:

$$\langle \mathcal{O}(\mathbf{k}, \eta_1) \bar{\mathcal{O}}(\mathbf{k}, \eta_2) \rangle'_{s_1 s_2} = \int \frac{d^3\mathbf{q}}{(2\pi)^3} G_{s_1 s_2}(|\mathbf{q}|, \eta_1, \eta_2; \mu_1) G_{s_1 s_2}(|\mathbf{k} - \mathbf{q}|, \eta_1, \eta_2; \mu_2), \quad (3.10)$$

is the de Sitter spectral density of \mathcal{O} . Equivalently³:

$$\langle \mathcal{O}(x_1) \bar{\mathcal{O}}(x_2) \rangle_{s_1 s_2} = \int_0^\infty \rho_{\mathcal{O}}^{\text{dS}}(\mu) \langle \chi_\mu(x_1) \bar{\chi}_\mu(x_2) \rangle_{s_1 s_2} d\mu, \quad (3.15)$$

where χ_μ is a fictitious scalar with mass parameter μ . We then arrive at the following relationship between the one-loop correlator and a fictitious tree-level correlator:

$$B_{1\text{-loop}}(k_1, k_2, k_3) = \int_0^\infty \rho_{\mu_1 \mu_2}^{\text{dS}}(\mu) B_{\text{tree}}(k_1, k_2, k_3; \mu) d\mu, \quad (3.16)$$

This is shown diagrammatically as in figure 3.

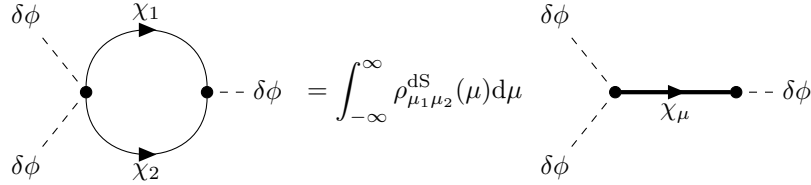


Figure 3. The spectral representation of the 3-point correlator at one-loop. This diagram only shows one of the ways $\delta\phi$ can contract with $e^{\pm i\delta\phi/\Lambda}$.

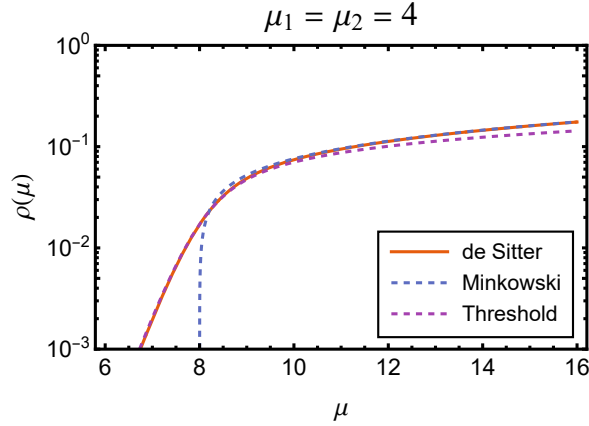


Figure 4. The de Sitter spectral density eq. (3.17) compared with the Minkowski spectral density eq. (3.19), and the near-threshold approximation eq. (3.21), for $\mu_1 = \mu_2 = 4$.

The corresponding de Sitter spectral density for $\mathcal{O} = \chi_1 \chi_2$ has been evaluated and has a

³This form of spectral decomposition is only correct when either at least one scalar has $M_I \geq 3/2$, or if both scalars have $M_I < 3/2$ then they must satisfy

$$\sqrt{\frac{9}{4} - M_1^2} + \sqrt{\frac{9}{4} - M_2^2} \leq \frac{3}{2}.$$

For these values of M_I , the multi-particle states all have $M \geq 3/2$.

surprisingly simple form [45–47]⁴:

$$\rho_{\mu_1\mu_2}^{\text{dS}}(\mu) = \frac{1}{8\pi^4} \frac{\mu \sinh \pi\mu}{\pi} \frac{\prod_{\epsilon_1, \epsilon_2 = \pm} \Gamma\left[\frac{3}{4} + \frac{i}{2}\epsilon(\mu + \epsilon_1\mu_1 + \epsilon_2\mu_2)\right]}{\Gamma\left(\frac{3}{2} - i\mu\right)\Gamma\left(\frac{3}{2} + i\mu\right)}. \quad (3.17)$$

In this paper we will not go through the derivation of this expression, but only discuss some of its features:

- At small distances the spacetime curvature is unimportant and we should expect that eq. (3.17) recovers its Minkowski form. This is achieved by taking the limit $\mu, \mu_1, \mu_2 \gg 1$, where all gamma functions in eq. (3.17) can be replaced by their Stirling approximation. One obtains

$$\begin{aligned} \rho_{\mu_1\mu_2}^{\text{dS}}(\mu) &\simeq \frac{1}{8\pi^2\mu} \prod_{\epsilon_1, \epsilon_2 = \pm} \sqrt{|\mu + \epsilon_1\mu_1 + \epsilon_2\mu_2|} \\ &\times \begin{cases} 1, & \mu > \mu_{12}, \\ e^{-\pi(\mu_{12} - \mu)}, & |\mu_1 - \mu_2| < \mu < \mu_{12}, \\ e^{-2\pi(\max\{\mu_1, \mu_2\} - \mu)}, & \mu < |\mu_1 - \mu_2|, \end{cases} \end{aligned} \quad (3.18)$$

where $\mu_{12} := \mu_1 + \mu_2$. For comparison, we quote the Minkowski spectral density for $\mathcal{O} = \chi_1\chi_2$:

$$\rho_{M_1M_2}^{\text{Mink}}(M) = \frac{1}{8\pi^2M} \prod_{\epsilon_1, \epsilon_2 = \pm} \sqrt{M + \epsilon_1M_1 + \epsilon_2M_2} \cdot \theta(M - M_1 - M_2). \quad (3.19)$$

The comparison between the two spectral densities is presented in figure 4. For $\mu_1, \mu_2 \gg 1$, the two spectral densities are close for $\mu - \mu_1 - \mu_2 \gg 1$, while they have major difference for $\mu < \mu_1 + \mu_2$. In particular, the Minkowski spectral density eq. (3.19) has a sharp cutoff at $\mu = \mu_1 + \mu_2$, whereas the de Sitter spectral density decays exponentially for $\mu < \mu_1 + \mu_2$.

- As will be shown in the next section, the oscillatory signal is determined by the *threshold limit* of the spectral density, i.e. $\mu = \mu_{12} + \varepsilon$ with $\varepsilon = \mathcal{O}(1) \ll \mu_1, \mu_2$. In this limit all gamma functions in eq. (3.17) can be approximated except

$$\Gamma\left[\frac{3}{4} \pm \frac{i}{2}(\mu - \mu_{12})\right] = \Gamma\left(\frac{3}{4} \pm \frac{i\varepsilon}{2}\right), \quad (3.20)$$

⁴We are also aware of another expression for the spectral density in terms of the hypergeometric function ${}_7F_6$ in [27, 29]. It can be numerically verified that our spectral density is related to the spectral density in [29], denoted as $P_{\mu_0}^{\text{dS}}(\mu)$, through the following equation:

$$\rho_{\mu_0\mu_0}^{\text{dS}}(\mu) = \frac{2\mu}{\pi} \text{Im } P_{\mu_0}^{\text{dS}}(\mu).$$

giving

$$\rho_{\mu_1\mu_2}^{\text{dS}}(\mu_{12} + \varepsilon) \simeq \frac{1}{4\pi^3} \sqrt{\frac{\mu_1\mu_2}{\mu_{12}}} \Gamma\left(\frac{3}{4} + \frac{i\varepsilon}{2}\right) \Gamma\left(\frac{3}{4} - \frac{i\varepsilon}{2}\right) e^{\pi\varepsilon/2}. \quad (3.21)$$

This form of the spectral density is plotted in figure 4, showing good agreement with the general form for small values of μ . It also differs from the flat space case eq. (3.19), where one has

$$\rho_{\mu_1\mu_2}^{\text{Mink}}(M_{12} + E) \simeq \frac{1}{4\pi^2} \sqrt{\frac{M_1 M_2}{M_{12}}} \sqrt{2E} \cdot \theta(E). \quad (3.22)$$

This difference is important in our chemical potential model because we will show later that the proper time elapsed from the creation to the annihilation of the heavy particle(s) is larger than H^{-1} in the squeezed limit. Consequently, the particle(s) can see the curvature in the time direction and distinguish de-Sitter from flat spacetime. Eq. (3.21) can be better understood by deriving it from the non-relativistic limit of de Sitter spacetime. Since this deviates from the main purpose of this paper, we leave the discussion in appendix C.

- As a function of complex μ , $\rho_{\mu_1\mu_2}^{\text{dS}}(\mu)$ is meromorphic, and only has contains simple poles at

$$\mu = \pm\mu_1 \pm \mu_2 \pm \left(\frac{3}{2} + 2\mathbb{N}\right)i. \quad (3.23)$$

Meanwhile, the late-time behavior of the mode function eq. (2.16) is given by

$$f_k(\eta; \mu) = \sum_{k=0}^{\infty} \left[A_k(-\eta)^{\Delta^+ + 2k} + B_k(-\eta)^{\Delta^- + 2k} \right], \quad \begin{cases} \Delta^+ := \frac{3}{2} + i\mu, \\ \Delta^- := \frac{3}{2} - i\mu. \end{cases} \quad (3.24)$$

Consequently, poles in the upper half plane corresponds to the μ values when $\Delta^+ = \Delta_1^\pm + \Delta_2^\pm$. From the dS/CFT perspective, these poles can further be attributed to different late-time operators appearing in the operator product expansion of $\chi_1\chi_2$ [47].

3.3 Central result for the signal

A systematic calculation of all contributions to the one-loop bispectrum will be carried out in the next section. However, in this section we give a quick derivation of the non-analytic piece in the squeezed limit. This piece is the oscillatory signal in cosmological collider physics. Our starting point will be the tree-level amplitude in (3.16), which is given by

$$\begin{aligned} B_{\text{tree}}(k_1, k_2, k_3; \mu) &= |\alpha|^2 \sum_{s_1, s_2} (is_1)(is_2) \int \sqrt{-g_1} d^4x_1 \int \sqrt{-g_2} d^4x_2 (-\eta_1)^{-i\lambda} (-\eta_2)^{i\lambda} \\ &\times \left\langle \delta\phi_{\mathbf{k}_1} \delta\phi_{\mathbf{k}_2} \delta\phi_{\mathbf{k}_3} \cdot e^{i\delta\phi(x_1)/\Lambda} e^{-i\delta\phi(x_2)/\Lambda} \right\rangle_{s_1 s_2} \langle \chi_\mu(x_1) \bar{\chi}_\mu(x_2) \rangle_{s_1 s_2}. \end{aligned} \quad (3.25)$$

The amplitude for the fictitious scalar has been computed in ref. [22] as part of a tree-level model. The dominant contribution comes from the $(-+)$ diagram.

In the left panel of figure 5 we plot the integrand in eq. (3.16) for the $(-+)$ diagram. The integrand has the form of an oscillatory function multiplied by a smooth function. In

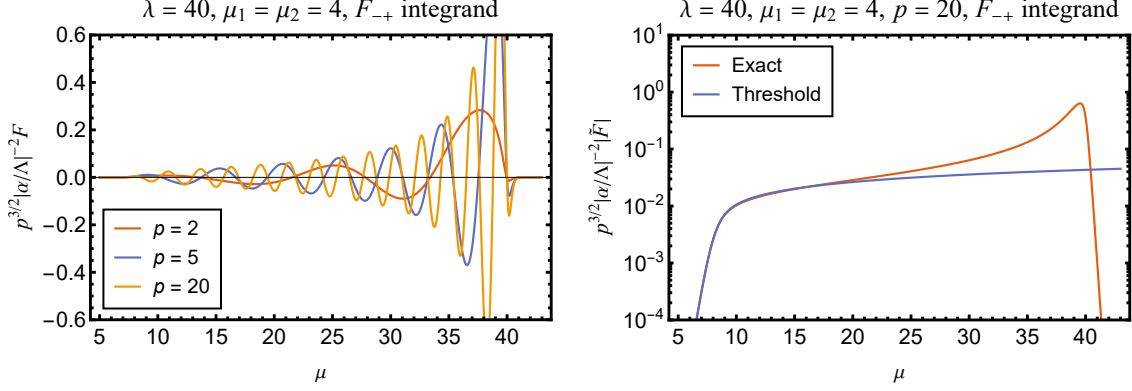


Figure 5. (Left) The integrand in eq. (3.16) for $\lambda = 40$, $\mu_1 = \mu_2 = 4$ and various p . The normalized bispectrum eq. (2.6) is used instead as the y -axis when making the plot. (Right) The magnitude of the integrand for $p = 20$. The orange line represents the exact integrand while the blue line represents the modified integrand to extract the near-threshold approximation in eq. (3.30).

particular, as we will see shortly, the phase does not have a stationary point. However, the smooth envelope changes rapidly around $\mu = \lambda$, and $\mu = \mu_{12}$. Near $\mu = \lambda$, the tree-level amplitude B_{tree} peaks and then decays exponentially once $\mu > \lambda$. Near $\mu = \mu_{12}$, the spectral density also decays exponentially for $\mu < \mu_{12}$. The integral is therefore dominated by the two regions where $\mu \simeq \mu_{12}, \lambda$.

For values of the mass parameter, $\mu \lesssim \lambda$, the squeezed limit tree level amplitude can be approximately calculated in the *Stationary Phase Approximation* (SPA), and it is given by [22]

$$B_{\text{tree,SPA}}(k_1, k_2, k_3; \mu) = \frac{\pi}{16k_1^3 k_2^3} \frac{|\alpha|^2}{\Lambda^3} \frac{\lambda^{1/2} \mu^{-1/2}}{\lambda^2 - \mu^2} p^{3/2 - i(\lambda - \mu)} e^{i\vartheta_*(\lambda, \mu)} + \text{c.c.}, \quad (3.26)$$

where the phase ϑ_* is given by⁵

$$\vartheta_*(\lambda, \mu) := \lambda \log 2\lambda + \mu \log 2\mu - (\lambda + \mu) \log(\lambda + \mu). \quad (3.27)$$

Plugging this into eq. (3.16), we obtain

$$B_{1\text{-loop}}(k_1, k_2, k_3) \sim \int_0^\infty \rho_{\mu_1 \mu_2}^{\text{dS}}(\mu) B_{\text{tree}}^{(\text{SPA})}(k_1, k_2, k_3; \mu)$$

⁵Ref. [22] does not present an expression for this phase as it is unimportant for their computation. We will derive it in section 4.2.

$$\sim \frac{\pi}{16k_1^3 k_2^3} \frac{|\alpha|^2}{\Lambda^3} \int_0^\lambda \frac{\lambda^{1/2} \mu^{-1/2}}{\lambda^2 - \mu^2} p^{3/2-i(\lambda-\mu)} e^{i\vartheta_*(\lambda,\mu)} \rho_{\mu_1\mu_2}^{\text{dS}}(\mu) d\mu. \quad (3.28)$$

Note that the superficial divergence when $\mu \rightarrow \lambda$ is an artifact of SPA and does not exist in the exact expression.

The full phase⁶

$$\vartheta(\lambda, \mu, p) := -(\lambda - \mu) \log p + \vartheta_*(\lambda, \mu), \quad \frac{\partial \vartheta}{\partial \mu} = \log \frac{2\mu p}{\lambda + \mu} > 0 \quad (3.29)$$

does not, as we mentioned before, have a stationary point on its own. Inspection of eq. (3.28) tells us that the non-analyticity is proportional to $p^{-i(\lambda-\mu)}$. Thus, only the $\mu \rightarrow \mu_{12}$ limit contribution has oscillating behavior as a function of p .

To isolate this limit, we consider a modified integral:

$$B_{1\text{-loop}}^{(\mu_{12})}(k_1, k_2, k_3) \simeq B_{\text{tree}}^{(\text{SPA})}(k_1, k_2, k_3; \mu_{12}) \int_{-\infty}^{\infty+} \rho_{\mu_1\mu_2}^{\text{dS}}(\mu_{12} + \varepsilon) \beta^{i\varepsilon} d\varepsilon, \quad (3.30)$$

$$\beta := \exp\left(\frac{\partial \vartheta}{\partial \mu}\right) \Big|_{\mu=\mu_{12}} = \frac{2\mu_{12}p}{\lambda + \mu_{12}}. \quad (3.31)$$

As shown in the right panel of figure 5, this new integral leaves the envelope of the integrand near $\mu \simeq \mu_{12}$ unmodified, but also lets it continues to oscillate beyond $\mu = \lambda$, eliminating the contribution near that limit. To simplify the calculation, we have also expanded the full phase eq. (3.29) to linear order around $\mu = \mu_{12}$.

We can now further approximate $\rho_{\mu_1\mu_2}^{\text{dS}}(\mu)$ by eq. (3.21) and obtain an approximate form for the signal

$$\begin{aligned} B_{1\text{-loop,sq}}^{(\mu_{12})}(k_1, k_2, k_3) &\simeq \frac{1}{2\pi^{3/2}} \sqrt{\frac{\mu_1\mu_2}{\mu_{12}}} \left(\frac{2\mu_{12}p}{\lambda + \mu_{12}} \right)^{-3/2} e^{3\pi i/4} B_{\text{tree}}^{(\text{SPA})}(k_1, k_2, k_3; \mu_{12}) \\ &= \frac{1}{32\sqrt{\pi} k_1^3 k_2^3} \frac{|\alpha|^2}{\Lambda^3} \frac{\lambda^{1/2} \mu_{12}^{-1/2}}{\lambda^2 - \mu_{12}^2} \sqrt{\frac{\mu_1\mu_2}{\mu_{12}}} \\ &\quad \times \left(\frac{2\mu_{12}}{\lambda + \mu_{12}} \right)^{-3/2} p^{-i(\lambda-\mu_{12})} e^{i\vartheta_*(\lambda,\mu_{12})+3\pi i/4}. \end{aligned} \quad (3.32)$$

Here we have used the Gamma function integral identity in eq. (A.8) to perform the integral over ε . Matching to the bispectrum parametrized by eq. (2.6), the non-analytic piece of the

⁶Even for moderate p , ϑ is given by eq. (4.22) and its derivative is given by

$$\frac{\partial \vartheta}{\partial \mu} = \frac{1}{2} \log \frac{\lambda + \mu - px_*}{\lambda - \mu - px_*} - \log \frac{\lambda + \mu}{\lambda - \mu} > 0,$$

where $x_* = x_*^-$ is given by eq. (4.19). The latter is clearly positive-definite.

signal is given by

$$F_{1\text{-loop,sq}}^{(\mu_{12})}(k_1, k_2, k_3) = \tilde{F}_{1\text{-loop,sq}}^{(\mu_{12})}(k_1, k_2, k_3) + \text{c.c.}, \quad (3.33)$$

$$\tilde{F}_{1\text{-loop,sq}}^{(\mu_{12})}(k_1, k_2, k_3) \simeq f_{\text{oscil}}(\lambda, \mu_1, \mu_2) p^{-3-i(\lambda-\mu_{12})}, \quad (3.34)$$

where the function, f_{oscil} , is given by

$$f_{\text{oscil}} = -\frac{5}{12\sqrt{\pi}} \frac{|\alpha|^2}{\Lambda^2} \frac{\lambda^{3/2} \mu_{12}^{-1/2}}{\lambda^2 - \mu_{12}^2} \sqrt{\frac{\mu_1 \mu_2}{\mu_{12}}} \left(\frac{2\mu_{12}}{\lambda + \mu_{12}} \right)^{-3/2} e^{i\vartheta_*(\lambda, \mu_{12}) + 3\pi i/4}. \quad (3.35)$$

Before going through a more systematic derivation, we list some important features of the signal here:

- The β -factor defined in eq. (3.30) has a clear physical meaning: it measures the proper time lapse between the creation and annihilation of the heavy particle(s) in its own reference frame. This can be seen by noting that the μ -dependence in the phase $\vartheta(\lambda, \mu, p)$ comes from the time evolution of the heavy particle(s), thus

$$\log \beta = \frac{\partial}{\partial \mu_{12}} \int_{\eta_{1*}}^{\eta_{2*}} E(\eta) \frac{d\eta}{(-\eta)} = \int_{\eta_{1*}}^{\eta_{2*}} \frac{\mu_{12}}{E(\eta)} \frac{d\eta}{(-\eta)} = \Delta T, \quad (3.36)$$

where

$$E(\eta) := \sqrt{k_3^2 \eta^2 + \mu_{12}^2} \quad (3.37)$$

is the local energy of the heavy particle(s). This shows that $e^{\Delta T}$ is proportional to the squeeze parameter p in the squeezed limit.

- Compared to the $p^{-3/2}$ dilution in tree-level exchanges, the one-loop signal decays faster as p^{-3} . This is because $p^{-3/2}$ is a result of the matter-like dilution of the heavy particle between its production and decay. Due to the presence of two heavy particles in the loop, the cost of dilution is doubled.
- At large p the oscillation frequency of the one-loop amplitude is the same as would be obtained from a tree-level exchange, except for a phase shift $3\pi i/4$. As has been discussed in ref. [28], this phase can be used to separately determine λ and μ from the data, when combined with the oscillating frequency. In ref. [22, 24], it is also suggested that such separation can be achieved by measuring the frequency of the non-analytic component as a function of p for small to moderate values of p . For this purpose, we will also derive the SPA approximation for the signal applicable to moderate p in section 5.1.

In this section we have approximately calculated the non-analytic piece of the bispectrum, but we did note that the integral in eq. (3.16) has a large contribution from the region $\mu \rightarrow \lambda$. In this region the contribution is neither oscillatory, nor suppressed. Therefore, this model

is a good case study where the exchange of the heavy scalars provides both the signal and background.

The following two sections will be dedicated to a systematic calculation of all one-loop contributions to the bispectrum, including the backgrounds.

4 Systematic Computation: Tree-level Model Revisited

In this section we will evaluate the tree-level amplitude eq. (3.25) systematically. The amplitude eq. (3.25), when evaluated by series expanding $e^{\pm i\delta\phi/\Lambda}$, contains late-time divergence in individual contributions. We will perform a change of basis in the effective tree-level Lagrangian to eliminate this divergence explicitly. Besides the results in ref. [22], we will also derive some extra quantities necessary for the one-loop calculation, such as the full form of the phase in eq. (4.22), the improved approximated form in eq. (4.20), and the contributions from the $(++)$ -diagrams in section 4.3.

4.1 Perturbative expansion under late-time-finite basis

In ref. [22], the amplitude eq. (3.25) is evaluated by series expanding $e^{\pm i\delta\phi/\Lambda}$. This gives rise to two diagrams, shown in figure 6. It turns out that both diagrams contain divergence in the late-time region. To understand its origin note that, at leading order in α , the tree-level amplitude can be derived from the following Lagrangian:

$$\begin{aligned}\mathcal{L}_\chi &= -|\nabla\chi_\mu|^2 - M^2|\chi_\mu|^2 - \alpha_\mu\chi_\mu e^{i\phi/\Lambda} - \bar{\alpha}_\mu\bar{\chi}_\mu e^{-i\phi/\Lambda}, \\ &= -|\nabla\chi_\mu|^2 - M^2|\chi_\mu|^2 - \alpha_\mu(-\eta)^{-i\lambda}\chi_\mu e^{i\delta\phi/\Lambda} - \bar{\alpha}_\mu(-\eta)^{i\lambda}\bar{\chi}_\mu e^{-i\delta\phi/\Lambda},\end{aligned}\quad (4.1)$$

where $t = -\log(-\eta)$ and $M^2 = \mu^2 + 9/4$. Note that the μ -dependent coupling α_μ should account for the variation in spectral density: by matching to the tree-level result, we should have

$$|\alpha_\mu|^2 = \rho_{\mu_1\mu_2}^{\text{ds}}(\mu) |\alpha|^2. \quad (4.2)$$

In the rest of this section, we will drop the subscript μ on χ_μ and α_μ for simplicity.

The Lagrangian in eq. (4.1) is invariant under

$$\phi \rightarrow \phi + c, \quad \chi \rightarrow \chi e^{ic/\Lambda}, \quad (4.3)$$

following from eq. (3.8), which ensures no late-time divergence. However, the shift symmetry is not manifest if one expands $e^{\pm i\delta\phi/\Lambda}$ in a power series for perturbative calculations. As a result, late-time divergences are present in individual diagrams, and only cancel after summing over all diagrams at the same order.

We are free to perform field redefinitions of χ in the Lagrangian eq. (4.1) because the contribution to the amplitude in eq. (3.25) will remain unchanged. To avoid complications with late-time divergences, consider the field redefinition $\chi \mapsto \chi e^{-i\phi/\Lambda}$ that brings the Lagrangian

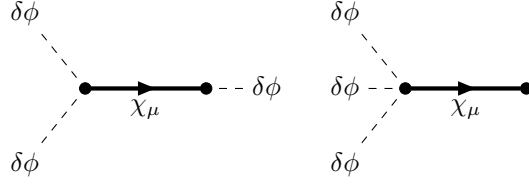


Figure 6. The effective tree-level diagrams from the spectral decomposition. There are another two diagrams with χ_μ flowing in the opposite direction. In the new basis described by eq. (4.8), only the first diagram is present.

back to its chemical potential form:

$$\begin{aligned}\mathcal{L}_\chi &= -\left(\nabla^\mu + i\frac{\nabla^\mu\phi}{\Lambda}\right)\bar{\chi}\left(\nabla_\mu - i\frac{\nabla_\mu\phi}{\Lambda}\right)\chi - M^2|\chi|^2 - \alpha\chi - \bar{\alpha}\bar{\chi} \\ &= -|\nabla\chi|^2 - M^2|\chi|^2 - \alpha\chi - \bar{\alpha}\bar{\chi} + \frac{1}{\Lambda}\nabla_\mu\phi J^\mu - \frac{1}{\Lambda^2}(\nabla\phi)^2|\chi|^2.\end{aligned}\quad (4.4)$$

Treating the last two terms as interactions, the equation of motion of χ at free field order is given by

$$\left[-\left(\nabla_\mu - i\frac{\nabla_\mu\phi_0}{\Lambda}\right)^2 + M^2\right]\chi = -\bar{\alpha}, \quad \phi_0 = \dot{\phi}_0 t = -\dot{\phi}_0 \log(-\eta). \quad (4.5)$$

The inhomogeneous term on the r.h.s. gives rise to a homogeneous classical background for χ :

$$\chi_0 = \frac{\bar{\alpha}}{\lambda^2 + 3i\lambda - M^2} = -\frac{\bar{\alpha}}{\left(\frac{3}{2} - i\lambda\right)^2 + \mu^2}. \quad (4.6)$$

Now, consider the following field redefinition:

$$\chi \mapsto \chi_0 + \delta\chi e^{i\phi/\Lambda}. \quad (4.7)$$

Substituting this into eq. (4.4) gives

$$\begin{aligned}\mathcal{L}_{\delta\chi} &= -|\nabla\delta\chi|^2 - M^2|\delta\chi|^2 - \frac{|\chi_0|^2}{\Lambda^2}(\nabla\phi)^2 + \mathcal{L}_{\delta\chi}^{(\text{int})} \\ &\supset -|\nabla\delta\chi|^2 - M^2|\delta\chi|^2 - \frac{|\chi_0|^2}{\Lambda^2}(\nabla\delta\phi)^2 + \mathcal{L}_{\delta\chi}^{(\text{int})},\end{aligned}\quad (4.8)$$

$$\begin{aligned}\mathcal{L}_{\delta\chi}^{(\text{int})} &= \bar{\chi}_0(-\eta)^{-i\lambda}\left[\frac{i}{\Lambda}\square\delta\phi + 2(-\eta)\frac{\lambda}{\Lambda}\delta\phi' - \frac{1}{\Lambda^2}(\nabla\delta\phi)^2\right]e^{i\delta\phi/\Lambda}\delta\chi + \text{c.c.} \\ &= \bar{\chi}_0(-\eta)^{-i\lambda}\left[\frac{i}{\Lambda}\square\delta\phi + 2(-\eta)\frac{\lambda}{\Lambda}\delta\phi' - \frac{1}{\Lambda^2}(\nabla\delta\phi)^2\right]\left(1 + \frac{i}{\Lambda}\delta\phi + \dots\right)\delta\chi + \text{c.c.},\end{aligned}\quad (4.9)$$

where we have dropped all constant terms and tadpoles in $\delta\phi$ at the second line of $\mathcal{L}_{\delta\chi}$. This new basis is advantageous over the exponential basis eq. (4.1) as at least one of the $\delta\phi$ in each

interaction has a derivative acting on it. This improves the late-time behavior and leads to finite results for each individual diagram.

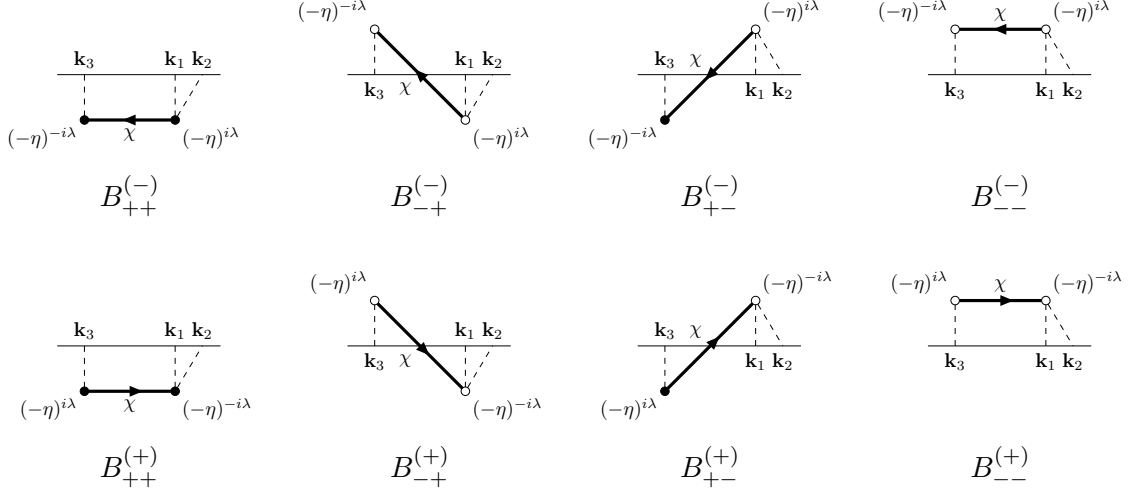


Figure 7. The various effective tree diagrams contributing to the bispectrum. The solid dots \bullet represent (+)-type vertices, while the empty dots \circ represent (-)-type vertices. For each diagram shown, there are also another two diagrams where \mathbf{k}_3 is permuted with \mathbf{k}_1 or \mathbf{k}_2 . Here we also use the upper/lower half plane notation for the two types of vertices to indicate the direction of time: (+)-type vertices are in the lower half plane with time direction pointing upward, while (-)-type vertices are in the upper half plane with time direction pointing downward. The sign in parentheses corresponds to the direction of χ number flow, indicated in the diagram by the arrow.

In the new basis eq. (4.8) only the first diagram in figure 6 contributes to the bispectrum. In the in-in formalism this breaks up into 8 Feynmann diagrams as illustrated in figure 7. The total contribution to the bispectrum at this order is thus given by

$$B(k_1, k_2, k_3) = \sum_{s_1, s_2, s_3 = \pm} B_{s_1 s_2}^{(s_3)}(k_1, k_2, k_3) + (k_3 \rightarrow k_1, k_2), \quad (4.10)$$

where s_1 gives the index of the 2-point vertex, s_2 gives the index of the 3-point vertex, and s_3 indicates the direction of χ number flow. One can derive the following two relations between the 8 contributions:

$$\begin{aligned} B_{-s_1, -s_2}^{(-s_3)}(k_1, k_2, k_3) &= B_{s_1 s_2}^{(s_3)*}(k_1, k_2, k_3), \\ B_{s_1 s_2}^{(-s_3)}(k_1, k_2, k_3) &= -B_{s_1 s_2}^{(s_3)}(k_1, k_2, k_3) \Big|_{\lambda \rightarrow -\lambda}. \end{aligned} \quad (4.11)$$

Therefore, only $B_{++}^{(+)}$ and $B_{-+}^{(-)}$ need to be evaluated explicitly. Nonetheless, since the approximated form relies on the sign of λ , $B_{++}^{(\pm)}$ and $B_{-+}^{(\pm)}$ will be treated separately in approximate

calculations. In both cases, we have

$$B_{-+}^{(\pm)} = \frac{\lambda |\chi_0|^2}{4k_1^3 k_2^3 \Lambda^3} \int_0^\infty dx_2 \int_0^\infty dx_1 \mathcal{I}_{1,-+}^{(\pm)}(\lambda; x_1) \mathcal{I}_{2,-+}^{(\pm)}(\lambda, p, \chi; x_2), \quad (4.12)$$

$$B_{++}^{(\pm)} = -\frac{\lambda |\chi_0|^2}{4k_1^3 k_2^3 \Lambda^3} \left[\int_0^\infty dx_2 \int_0^{x_2} dx_1 \mathcal{I}_{1,++}^{(\pm)}(\lambda; x_1) \mathcal{I}_{2,-+}^{(\pm)}(\lambda, p, \chi; x_2) \right. \\ \left. + \int_0^\infty dx_2 \int_{x_2}^\infty dx_1 \mathcal{I}_{1,-+}^{(\mp)*}(\lambda; x_1) \mathcal{I}_{2,++}^{(\mp)*}(\lambda, p, \chi; x_2) \right], \quad (4.13)$$

where we have made the substitution $x_{1,2} := -k_3 \eta_{1,2}$. The functions, $\mathcal{I}_{1,2}$, are given by

$$\mathcal{I}_{1,s_1+}^{(s_3)}(\lambda; x_1) := e^{-\pi\mu/2} \sqrt{\frac{\pi}{2}} x_1^{-1/2+is_3\lambda} e^{-is_1 x_1} H_{i\mu}^{(1)}(x_1), \\ \mathcal{I}_{2,s_1+}^{(s_3)}(\lambda, p, \chi; x_2) := e^{-\pi\mu/2} \sqrt{\frac{\pi}{2}} \sum_{n=0}^2 (-s_1 i)^n \cdot c_n^{s_3} \cdot x_2^{-1/2+n-is_3\lambda} e^{is_1 p x_2} H_{i\mu}^{(1)*}(x_2). \quad (4.14)$$

The coefficients inside \mathcal{I}_2 are given by

$$c_0^\pm := -\frac{\mathbf{k}_1 \cdot \mathbf{k}_2}{k_3^2} \pm i\lambda \frac{k_1^2 + k_2^2}{k_3^2} = \frac{1}{2} [(1 \pm 2i\lambda)(p^2 - 2Q) - 1], \\ c_1^\pm := -\frac{\mathbf{k}_1 \cdot \mathbf{k}_2 (k_1 + k_2)}{k_3^3} \pm \frac{i\lambda k_1 k_2 (k_1 + k_2)}{k_3^3} = \frac{1}{2} p [p^2 - 2(1 \mp i\lambda)Q - 1], \\ c_2^\pm := -\frac{(\mathbf{k}_1 \cdot \mathbf{k}_2) k_1 k_2}{k_3^4} + \frac{k_1^2 k_2^2}{k_3^4} = \frac{1}{2} Q (p^2 - 1), \quad (4.15)$$

where $Q := k_1 k_2 / k_3^2 = \frac{1}{4}(p^2 - \chi^2)$. Notice in eq. (4.14) that as $x_i \rightarrow 0$, the integrands go as $x_i^{-1/2+n\pm i\lambda}$ with $n \geq 0$. The amplitude is now expressed in a form that is manifestly free of late-time divergences.

4.2 Contributions from B_{-+}

For $\lambda, \mu, \lambda - \mu \gg 1$, the SPA can be used to calculate eqs. (4.12) and (4.13). Starting from the Hankel functions $H_{i\mu}^{(1)}(x)$ with $\mu \gg 1$, we have Debye's asymptotic representation of the Hankel function:

$$H_{i\mu}^{(1)}(x) \simeq \sqrt{\frac{2}{\pi}} e^{\pi\mu/2} \cdot \frac{e^{ih(x,\mu)}}{(x^2 + \mu^2)^{1/4}} \left\{ 1 + \mathcal{O}\left[\frac{\mu^2}{(x^2 + \mu^2)^{3/2}}\right] \right\}, \\ h(x, \mu) = -\frac{\pi}{4} + \sqrt{x^2 + \mu^2} - \mu \operatorname{arcsinh} \frac{\mu}{x}, \quad \frac{\partial h}{\partial x} = \sqrt{1 + \frac{\mu^2}{x^2}}, \quad (4.16)$$

which follows directly from the WKB method. Substituting into eq. (4.14), the two integrands factorize into slowly-varying parts and highly oscillatory parts:

$$\begin{aligned}\mathcal{I}_{1,s_1+}^{(s_3)}(\lambda; x_1) &\simeq \frac{1}{x_1^{1/2}(x_1^2 + \mu^2)^{1/4}} e^{ig_{1,s_1}^{(s_3)}(x_1, \lambda, \mu)}, \\ \mathcal{I}_{2,s_1+}^{(s_3)}(\lambda, p, \chi; x_2) &\simeq \frac{\sum_{n=0}^2 (-s_1 i x_2)^n c_n^{s_3}}{x_2^{1/2}(x_2^2 + \mu^2)^{1/4}} e^{ig_{2,s_1}^{(s_3)}(x_2, \lambda, \mu, p)},\end{aligned}\tag{4.17}$$

where the phases are given by

$$\begin{aligned}g_{1,s_1}^{(s_3)}(x_1, \lambda, \mu) &:= -s_1 x_1 + s_3 \lambda \log x_1 + h(x_1, \mu), & \frac{\partial g_{1,s_1}^{(s_3)}}{\partial x_1} &= -s_1 + \frac{s_3 \lambda}{x_1} + \sqrt{1 + \frac{\mu^2}{x_1^2}}, \\ g_{2,s_1}^{(s_3)}(x_2, \lambda, \mu, p) &:= s_1 p x_2 - s_3 \lambda \log x_2 - h(x_2, \mu), & \frac{\partial g_{2,s_1}^{(s_3)}}{\partial x_2} &= s_1 p - \frac{s_3 \lambda}{x_2} - \sqrt{1 + \frac{\mu^2}{x_2^2}}.\end{aligned}\tag{4.18}$$

The dominant contributions to eqs. (4.12) and (4.13) then come from those diagrams for which a stationary phase, $g'(x_*) = 0$, with $x_* > 0$, exists in both integrals. The stationary points, along with the condition for their existence, are tabulated in table 1. For the x_2 integrals the stationary point is given by

$$x_*^\pm := \frac{\lambda p \pm \sqrt{\lambda^2 + \mu^2(p^2 - 1)}}{p^2 - 1} \xrightarrow{p \gg \lambda/\mu} \frac{\lambda \pm \mu}{p}\tag{4.19}$$

in the squeezed limit. For ease of notation we give only the squeezed limit expression in table 1.

Integrand	Stationary phase point $x_{1,2}$	Conditions
$\mathcal{I}_{1,-+}^{(s_3)}$	$\frac{\lambda^2 - \mu^2}{2\lambda}$	$s_3 = -, \quad \lambda > \mu$
$\mathcal{I}_{1,++}^{(s_3)}$	$\frac{\mu^2 - \lambda^2}{2\lambda}$	$s_3 = -, \quad \lambda < \mu$
$\mathcal{I}_{2,-+}^{(s_3)}$	$\frac{\lambda - \mu}{p}$	$s_3 = -, \quad \lambda > \mu$
$\mathcal{I}_{2,++}^{(s_3)}$	$-\frac{\lambda - \mu}{p}$	$s_3 = -, \quad \lambda < \mu$
	$\frac{\lambda + \mu}{p}$	$s_3 = +$

Table 1. The stationary phase points for the integrands in eq. (4.17) in the squeezed limit. The third column states the conditions for a stationary phase point to exist on the positive real axis.

By comparing table 1 with eqs. (4.12) and (4.13), it is manifest that only $B_{-+}^{(-)}$ has

stationary points for both the x_1 - and the x_2 -integral, and is the dominant contribution to the whole B_{tree} . Using SPA

$$B_{\text{tree}}(k_1, k_2, k_3) \simeq B_{-+}^{(-)}(k_1, k_2, k_3) \simeq \frac{\pi}{4k_1^3 k_2^3} \frac{|\alpha|^2}{\Lambda^3} \frac{\lambda^{1/2} e^{i\vartheta(\lambda, \mu, p)}}{(\lambda^2 - \mu^2)[\lambda^2 + \mu^2(p^2 - 1)]^{1/4}} \sum_{n=0}^2 d_n (ix_*)^{n-2}, \quad (4.20)$$

where $x_* := x_*^-$ is defined by (4.19),

$$d_0 := 1, \quad d_1 := p, \quad d_2 := \frac{1}{4}(p^2 - \chi^2). \quad (4.21)$$

The phase, ϑ , is given by

$$\begin{aligned} \vartheta(\lambda, \mu, p) &= \lambda \log \frac{2\lambda x_*}{\lambda^2 - \mu^2} - \mu \log \frac{\lambda + \mu}{\lambda - \mu} + \mu \operatorname{arcsinh} \frac{\mu}{x_*} \\ &\simeq \begin{cases} -(\lambda - \mu) \log p + \vartheta_*(\lambda, \mu), & p \gg \lambda/\mu, \\ -\lambda \log \frac{p+1}{2}, & p \ll \lambda/\mu, \lambda \gg \mu. \end{cases} \end{aligned} \quad (4.22)$$

In the squeezed limit, this reduces to eq. (3.26).

The amplitude, $B_{-+}^{(-)}$, can also be calculated exactly by noting that the two time integrals in eq. (4.12) factorize and each of them can be reduced to a standard integral given in eq. (A.1)

$$\begin{aligned} B_{-+}^{(-)}(k_1, k_2, k_3) &= \frac{1}{4k_1^3 k_2^3} \frac{|\alpha|^2}{\Lambda^3} \frac{\lambda e^{\pi\lambda}}{(\lambda^2 - \mu^2 - \frac{9}{4})^2 + 9\lambda^2} \mathbf{F}_{i\mu}^{\frac{1}{2}-i\lambda}(1) \sum_{n=0}^2 \frac{c_n^-}{2^n} \mathbf{F}_{i\mu}^{\frac{1}{2}+n+i\lambda}(p) \\ &= -\frac{1}{2k_1^3 k_2^3} \frac{|\alpha|^2}{\Lambda^3} \frac{\lambda e^{\pi\lambda}}{(\frac{3}{2} + i\lambda)^2 + \mu^2} \mathbf{F}_{i\mu}^{\frac{1}{2}-i\lambda}(1) \sum_{n=0}^2 \frac{d_n}{2^n} \mathbf{F}_{i\mu}^{-\frac{3}{2}+n+i\lambda}(p), \end{aligned} \quad (4.23)$$

where⁷

$$\mathbf{F}_{i\mu}^\rho(p) := \Gamma\left(\rho + \frac{i\mu}{2}, \rho - \frac{i\mu}{2}\right) F\left(\rho + \frac{i\mu}{2}, \rho - \frac{i\mu}{2}; \frac{1-p}{2}\right), \quad (4.24)$$

and $F\left(\frac{a,b}{c}; z\right) = {}_2F_1(a, b, c; z)$ is the hypergeometric function. In the second line in eq. (4.23) the recurrence relation given in eq. (A.7) for $\mathbf{F}_{i\mu}^\rho(p)$ has been used, after which our result is equivalent to the one in ref. [22] evaluated in the basis in eq. (4.1). Our calculation is manifestly finite at every step compared to the one in the exponential basis.

The exact form in eq. (4.23) reduces back to the stationary form in eq. (4.20) for $\lambda, \mu, \lambda - \mu \gg 1$, as shown in figure 8. Meanwhile, the naive singularity at $\mu \rightarrow \lambda$ in eqs. (3.26) and

⁷We use the following compact notation for products of gamma functions:

$$\Gamma\left(\frac{a_1, a_2, \dots, a_m}{b_1, b_2, \dots, b_n}\right) := \frac{\Gamma(a_1)\Gamma(a_2)\cdots\Gamma(a_m)}{\Gamma(b_1)\Gamma(b_2)\cdots\Gamma(b_n)}.$$

(4.20) becomes a finite resonance peak in the exact expression. The other contribution, $B_{-+}^{(+)}$, can be obtained from $B_{-+}^{(-)}$ using eq. (4.11):

$$B_{-+}^{(+)}(k_1, k_2, k_3) = -B_{-+}^{(-)}(k_1, k_2, k_3) \Big|_{\lambda \rightarrow -\lambda} \sim e^{-2\pi\lambda} B_{-+}^{(-)}(k_1, k_2, k_3), \quad (4.25)$$

i.e. it is always exponentially suppressed for $\lambda \gg 1$.

4.3 Contributions from B_{++}

To derive the full tree-level amplitude, we must also evaluate $B_{++}^{(\pm)}$ as well as all permuted diagrams ($k_3 \rightarrow k_1, k_2$). We defer the discussion of the permuted diagrams to section 5.4.

Now we focus on the contribution from $B_{++}^{(\pm)}$, given by the integral eq. (4.13). We start by breaking this integral into two parts for calculation convenience:

$$B_{++}^{(\pm)}(k_1, k_2, k_3) = B_{++,\text{NA}}^{(\pm)}(k_1, k_2, k_3) + B_{++,\text{A}}^{(\pm)}(k_1, k_2, k_3), \quad (4.26)$$

$$B_{++,\text{NA}}^{(\pm)}(k_1, k_2, k_3) := -\frac{\lambda |\chi_0|^2}{4k_1^3 k_2^3 \Lambda^3} \int_0^\infty dx_2 \int_0^\infty dx_1 \mathcal{I}_{1,-+}^{(\mp)*}(\lambda; x_1) \mathcal{I}_{2,++}^{(\mp)*}(\lambda, p, \chi; x_2), \quad (4.27)$$

$$B_{++,\text{A}}^{(\pm)}(k_1, k_2, k_3) := -\frac{\lambda |\chi_0|^2}{4k_1^3 k_2^3 \Lambda^3} \left[\int_0^\infty dx_2 \int_0^{x_2} dx_1 \mathcal{I}_{1,++}^{(\pm)}(\lambda; x_1) \mathcal{I}_{2,-+}^{(\pm)}(\lambda, p, \chi; x_2) \right. \\ \left. - \int_0^\infty dx_2 \int_0^{x_2} dx_1 \mathcal{I}_{1,-+}^{(\mp)*}(\lambda; x_1) \mathcal{I}_{2,++}^{(\mp)*}(\lambda, p, \chi; x_2) \right]. \quad (4.28)$$

We will soon see that in the squeezed limit they correspond to the non-analytic and analytic contributions respectively. Since $B_{++,\text{NA}}^{(\pm)}(k_1, k_2, k_3)$ also factorizes into two time integrals, it can be evaluated using eq. (A.1):

$$B_{++,\text{NA}}^{(\pm)}(k_1, k_2, k_3) = \frac{1}{2k_1^3 k_2^3} \frac{|\alpha|^2}{\Lambda^3} \frac{\lambda e^{\pm\pi\lambda}}{(\frac{3}{2} \mp i\lambda)^2 + \mu^2} \mathbf{F}_{i\mu}^{\frac{1}{2} \pm i\lambda}(1) \sum_{n=0}^2 (-1)^n \frac{d_n}{2^n} \mathbf{F}_{i\mu}^{-\frac{3}{2} + n \mp i\lambda}(-p + i\epsilon). \quad (4.29)$$

As shown in ref. [22], $B_{++,\text{NA}}^{(+)}$ is suppressed by $e^{-\pi|\lambda-\mu|}$ and only becomes comparable to $B_{-+}^{(-)}$ when $\mu \simeq \lambda$, while one can similarly show that $B_{++,\text{NA}}^{(-)}$ is suppressed by $e^{-\pi \max\{\lambda, \mu\}}$ and can be always neglected.

The second part of eq. (4.13) defined by eq. (4.28) does not factorize between x_1 and x_2 , and we will leave its exact evaluation to appendix D. Here we will derive its approximate form in a different approach. As implied by table 1, the two time integrals in eq. (4.28) never have stationary phase points simultaneously. Therefore, it is expected that the heavy propagator is far off-shell, so that the amplitude is dominated by the $\eta_1 \rightarrow \eta_2$ limit and can be described

by an effective local Lagrangian of the inflaton⁸:

$$\begin{aligned}
\mathcal{L}_\phi &= |\alpha|^2 e^{i\phi/\Lambda} \frac{1}{-\square + M^2} e^{-i\phi/\Lambda} \\
&= |\alpha|^2 \left[- \left(\nabla^\mu - \frac{i\nabla^\mu \phi}{\Lambda} \right) \left(\nabla_\mu - \frac{i\nabla_\mu \phi}{\Lambda} \right) + M^2 \right]^{-1} \cdot 1 \\
&= -|\alpha|^2 \sum_{k=0}^{\infty} \frac{\left[-\square + \frac{2i\nabla^\mu \delta\phi \nabla_\mu + i\square \delta\phi}{\Lambda} + \frac{(\nabla\delta\phi)^2}{\Lambda^2} - 2\lambda \left(i\eta\partial_\eta - \frac{3i}{2} + \frac{\eta\delta\phi'}{\Lambda} \right) \right]^k}{(\lambda^2 - M^2)^{k+1}} \cdot 1. \tag{4.30}
\end{aligned}$$

For $|\lambda^2 - M^2| \gtrsim \mathcal{O}(\lambda^2)$, this becomes an expansion in λ^{-1} . The leading-order contribution to the 3-point function is given by

$$\mathcal{L}_{\delta\phi^3}^{(\text{loc})} = \frac{4\lambda|\alpha|^2}{\Lambda^3(\lambda^2 - M^2)^3} (-\eta)\delta\phi'(\nabla\delta\phi)^2 + \frac{8\lambda^3|\alpha|^2}{\Lambda^3(\lambda^2 - M^2)^4} (-\eta)^3\delta\phi'^3 + \mathcal{O}(\lambda^{-7}). \tag{4.31}$$

From this local Lagrangian we arrive at the following estimation for the analytic contribution:

$$B_{++} \simeq B_{++,\Lambda} \simeq B_{\text{loc}}(k_1, k_2, k_3) := B_{+,\text{loc}}(k_1, k_2, k_3) + (k_3 \rightarrow k_1, k_2) + \text{c.c.}, \tag{4.32}$$

$$\begin{aligned}
B_{+,\text{loc}}(k_1, k_2, k_3) &= \frac{1}{8k_1^3 k_2^3 k_3^3} \int_{-\infty_-}^0 \frac{d\eta}{\eta^4} e^{i(k_1+k_2+k_3)\eta} \left\{ \frac{8i\lambda|\alpha|^2}{\Lambda^3(\lambda^2 - M^2)^3} (-\eta)(k_3^2\eta) \right. \\
&\quad \times \eta^2 [-k_1^2 k_2^2 \eta^2 - (\mathbf{k}_1 \cdot \mathbf{k}_2)(1 - ik_1\eta)(1 - ik_2\eta)] \\
&\quad \left. + \frac{1}{3} \frac{48i\lambda^3|\alpha|^2}{\Lambda^3(\lambda^2 - M^2)^4} (-\eta)^3 (k_1^2 k_2^2 k_3^2 \eta^3) \right\} \\
&= -\frac{1}{k_1^3 k_2^3} \frac{|\alpha|^2}{\Lambda^3} \frac{\lambda}{(\lambda^2 - M^2)^3} \left[\frac{p^2}{p+1} - \frac{Q(p+2)}{(p+1)^2} - \frac{1}{2} - \frac{4\lambda^2}{\lambda^2 - M^2} \frac{Q^2}{(p+1)^3} \right], \tag{4.33}
\end{aligned}$$

where $Q := k_1 k_2 / k_3^2 = \frac{1}{4}(p^2 - \chi^2)$. At large p , eq. (4.33) becomes

$$B_{+,\text{loc}}(k_1, k_2, k_3) \xrightarrow{p \gg 1} -\frac{3}{4k_1^3 k_2^3} \frac{|\alpha|^2}{\Lambda^3} \frac{\lambda}{(\lambda^2 - M^2)^3} \left(1 - \frac{1}{3} \frac{\lambda^2}{\lambda^2 - M^2} \right) p, \tag{4.34}$$

$$F_{+,\text{loc}}(k_1, k_2, k_3) \xrightarrow{p \gg 1} 10 \left| \frac{\alpha}{\Lambda} \right|^2 \frac{\lambda^2}{(\lambda^2 - M^2)^3} \left(1 - \frac{1}{3} \frac{\lambda^2}{\lambda^2 - M^2} \right) p^{-2}. \tag{4.35}$$

Compared with eq. (3.26), we find that $B_{++}(k_1, k_2, k_3)$ is suppressed by λ^{-3} for $\lambda, \mu \gg 1$, except near $\mu \simeq \lambda$. It is also worth noting that the p^{-2} behavior in the squeezed limit of the

⁸For $M \gg \lambda$, χ decouples from the theory and this effective Lagrangian has the usual interpretation under effective field theory. For $\lambda > M$, such interpretation is obscured by the fact that χ are massively produced on-shell.

normalized bispectrum is a feature applied to all models of single-field inflation [48].

Figure 8 shows the sizes of $B_{-+}^{(-)}$, $B_{++,\text{NA}}^{(+)}$ and $B_{++,\text{A}}^{(\pm)}$ as functions of μ for $\lambda = 40$ and $p = 20$. It is obvious that $B_{++,\text{NA}}^{(+)}$ and $B_{++,\text{A}}^{(\pm)}$ are both negligible in magnitude compared to $B_{-+}^{(-)}$, except near $\mu \simeq \lambda$ where they become comparable. Since the one-loop amplitude involves integrating over, μ as in eq. (3.16), $B_{++,\text{NA}}^{(+)}$ and $B_{++,\text{A}}^{(\pm)}$ cannot be dropped in the full one-loop evaluation.

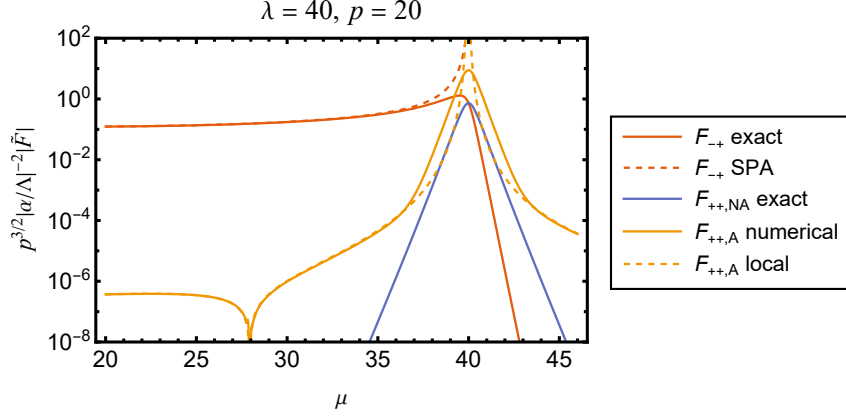


Figure 8. The magnitudes of contributions from $F_{-+}^{(-)}$, $F_{++,\text{NA}}^{(+)}$ and $F_{++,\text{A}}^{(\pm)}$ versus μ for $\lambda = 40$, and $p = 20$. For $F_{++,\text{A}}^{(\pm)}$ we take the average over permuted diagrams to make the numerical result and local estimation eq. (4.30) comparable. From this plot we can see all important contributions near $\mu = \lambda$, where most approximations break down. Note that there are other contributions that are exponentially suppressed by at least $e^{-\pi\lambda}$ and thus invisible on the plot.

5 Systematic Computation: One-loop Model

In this section we will compute the one-loop amplitude by performing the integral over the spectral representation in eq. (3.16), using the tree-level results of the previous section. We will first derive the signal and the background for general values of the squeezing parameter, p , using the same approximation as in section 3.3. We then demonstrate how the full amplitude at $\mathcal{O}(\alpha^2)$ can be evaluated, with the full results derived in appendix E. Finally, we will include the combinatorial backgrounds from permuted diagrams, and discuss higher order corrections in the last subsection.

5.1 Signal from the threshold limit

For $\lambda, \mu_1, \mu_2, \lambda - \mu_1 - \mu_2 \gg 1$, we have argued in section 3.3 that the B_{-+} amplitude is dominated by the region around $\mu = \mu_{12}$ and $\mu = \lambda$. Including both contribution gives the following approximation

$$B_{1\text{-loop}}(k_1, k_2, k_3) = \int_0^\infty \rho_{\mu_1\mu_2}^{\text{ds}}(\mu) B_{\text{tree}}(k_1, k_2, k_3; \mu)$$

$$\simeq B_{1\text{-loop}}^{(\mu_{12})}(k_1, k_2, k_3) + B_{1\text{-loop}}^{(\lambda)}(k_1, k_2, k_3). \quad (5.1)$$

To extract the $\mu \rightarrow \mu_{12}$ limit we use a slightly modified form of eq. (3.30)

$$B_{1\text{-loop}}^{(\mu_{12})}(k_1, k_2, k_3) \simeq B_{\text{tree,SPA}}(k_1, k_2, k_3; \mu_{12}) \int_{-\infty}^{\infty+} \rho_{\mu_1\mu_2}^{\text{dS}}(\mu_{12} + \varepsilon) \beta^{i\varepsilon} e^{\frac{i}{2}\gamma\varepsilon^2} d\varepsilon, \quad (5.2)$$

where

$$\begin{aligned} \beta &:= \exp\left(\frac{\partial\vartheta}{\partial\mu}\right)\Big|_{\mu=\mu_{12}} = \frac{\lambda - \mu_{12}}{\lambda + \mu_{12}} \sqrt{\frac{\lambda + \mu_{12} - px_*}{\lambda - \mu_{12} - px_*}} \xrightarrow{p \gg \lambda/\mu} \frac{2\mu_{12}p}{\lambda + \mu_{12}}, \\ \gamma &:= \frac{\partial^2\vartheta}{\partial\mu^2}\Big|_{\mu=\mu_{12}} = \frac{\lambda}{\lambda^2 - \mu_{12}^2} \left[\frac{\lambda p}{\sqrt{\lambda^2 + \mu_{12}^2(p^2 - 1)}} - 1 \right] \xrightarrow{p \gg \lambda/\mu} \frac{\lambda}{\mu_{12}(\lambda + \mu_{12})}. \end{aligned} \quad (5.3)$$

Note that compared to eq. (3.30), we have included the second order expansion of the phase ϑ near ε in eq. (5.2) to improve the estimation for moderate p . Similarly, we extract the $\mu \rightarrow \lambda$ background with

$$B_{1\text{-loop}}^{(\lambda)}(k_1, k_2, k_3) \simeq \rho_{\mu_1\mu_2}^{\text{Mink}}(\lambda) \int_{-\infty}^{\infty} B_{\text{tree}}(k_1, k_2, k_3; \lambda + \varepsilon) d\varepsilon. \quad (5.4)$$

In other words, we can use the SPA form of B_{tree} near $\mu \sim \mu_{12}$ and the Minkowski limit of $\rho_{\mu_1\mu_2}^{\text{dS}}(\mu)$ near $\mu \sim \lambda$ respectively.

The fact that the integrand $\rho_{\mu_1\mu_2}^{\text{dS}}(\mu) B_{\text{tree}}(\mu)$ drops rapidly to zero near $\mu \lesssim \mu_{12}$ and has a peak at $\mu \simeq \lambda$ has clear physical meanings: the former corresponds to the *threshold limit* where the mass μ of the multi-particle state is close to or drops below the total rest mass μ_{12} of the two components; the latter corresponds to the *resonance limit*, which can be traced back to the resonance behavior in the homogeneous background of the χ field given by eq. (4.6) as $\mu \rightarrow \lambda$. As has been argued in section 3.3, the threshold limit gives the non-analytic signal, while the resonance limit contributes to the analytic background.

For the signal, we can combine eq. (3.21) with eq. (5.2) to get a more accurate stationary phase estimation:

$$\begin{aligned} B_{1\text{-loop}}^{(\mu_{12})}(k_1, k_2, k_3) &\simeq \frac{1}{2\pi^{3/2}} \sqrt{\frac{\mu_1\mu_2}{\mu_{12}}} B_{\text{tree}}(k_1, k_2, k_3; \mu_{12}) \\ &\times e^{3\pi i/4} \sum_{k=0}^{\infty} \frac{(3/2)_k}{k!} \beta^{-3/2-2k} e^{-\frac{i}{2}\gamma(3/2+2k)^2}. \quad (\log \beta \gg \gamma) \end{aligned} \quad (5.5)$$

where $(a)_m := a(a+1)\cdots(a+m-1)$ is the Pochhammer symbol. Note that we have approximated the integral as a sum over residues of the poles in eq. (3.21), which is only valid up to corrections of order

$$\rho_{\mu_1\mu_2}^{\text{dS}}(\mu_{12} + \varepsilon) \Big|_{\gamma\varepsilon + \log \beta = 0} \sim e^{-\pi \log \beta / \gamma}. \quad (5.6)$$

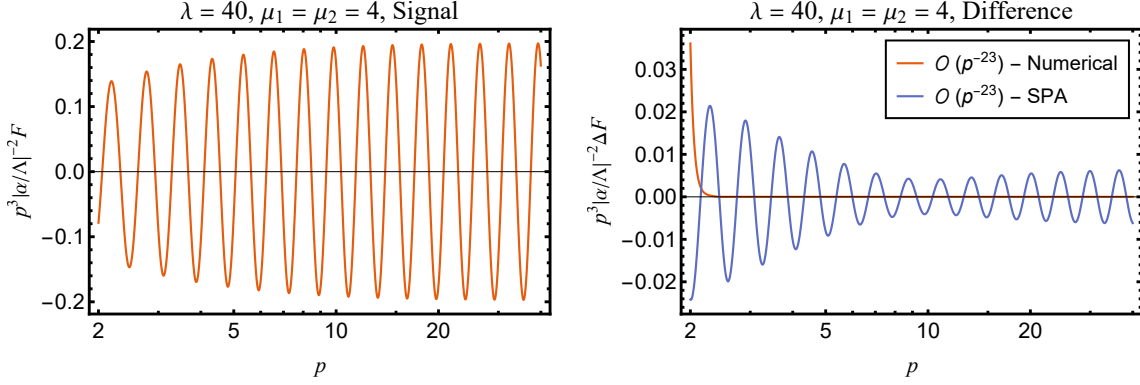


Figure 9. (Left) The one-loop oscillatory signal coming from the threshold limit for $\lambda = 40$ and $\mu = 4$, rescaled by p^3 . (Right) The difference between two approximate calculations and the numerical evaluation of eq. (3.16): (i) the analytic sum over poles up to $\mathcal{O}(p^{-23})$ (see section 5.3 and appendix E); (ii) the SPA result eq. (5.5). In calculating the difference between the analytic sum and the numerical result, the difference in the full $F_{-+}^{(-)}$ amplitude is computed, which includes both the signal and the analytic background in $F_{-+}^{(-)}$. For p away from 2, the numerical result agrees with the analytic sum, while the error for the improved SPA result is within 5%.

Eq. (5.5) reduces to eq. (3.32) in the squeezed limit with $\gamma \ll 1$. Figure 9 shows the shape of the non-analytic signal in terms of the bispectrum, F , and its comparison with the numerical result and the analytic form we will derive later in section 5.3. We also calculate the oscillating frequency at different p -value and the result is presented in figure 10. As argued in [22, 24], the frequency at small p and large p can be used together to infer both the total mass μ_{12} , and the chemical potential λ .

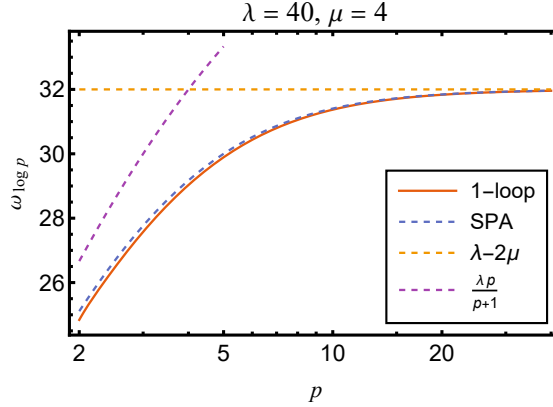


Figure 10. The oscillation frequency of the signal for $\lambda = 40$ and $\mu_1 = \mu_2 = 4$. The frequency of the signal is defined as $\omega_{\log p} := -\text{Im} \frac{\partial \log \tilde{F}}{\partial \log p}$. The SPA curve is given by $-\frac{\partial \vartheta}{\partial \log p}$ with ϑ defined by eq. (4.22). The other two lines are derived from the small p and the large p limits in eq. (4.22), showing that we are able to extract both the chemical potential and total mass independently from data, as emphasized in [22, 24].

5.2 Resonance backgrounds

The one-loop amplitude also differs from the tree-level amplitude by having an analytic background coming from the resonance production. Such a background cannot be neglected as the amplitude of the one-loop signal decays as $\mathcal{O}(p^{-3})$, which is faster than a typical analytic contribution, decreasing as $\mathcal{O}(p^{-2})$ in the large- p limit. In this subsection, we will approximately evaluate this background coming from the resonance limit of B_{-+} , given by eq. (5.4), as well as a similar one from B_{++} . Starting from eq. (5.4), we need to substitute terms singular near $\mu \simeq \lambda$ in the SPA form of eq. (4.20) by their exact form in eq. (4.23):

$$\frac{(ix_*)^{n-2}}{\lambda^2 - \mu^2} \rightarrow -\frac{1}{2\pi} \frac{\Gamma(\frac{1}{2} - i\lambda + i\mu)\Gamma(-\frac{3}{2} + n + i\lambda - i\mu)}{(\frac{3}{2} + i\lambda)^2 + \mu^2} \left(\frac{x_*}{\lambda - \mu}\right)^{n-2} e^{\pi(\lambda - \mu)}. \quad (5.7)$$

Note that $x_*/(\lambda - \mu) \rightarrow 1/p$ as $\mu \rightarrow \lambda$. For $\lambda - \mu \gg 1$ one can apply the Stirling approximation on the RHS and obtain the LHS, while this does not apply when $\mu \simeq \lambda$. Besides these terms, we can approximate all other slow-varying terms in eq. (4.20) by their values at $\mu = \lambda$,

$$B_{\text{tree},-+}^{(-)}(k_1, k_2, k_3; \lambda + \varepsilon) \simeq \frac{\pi}{8k_1^3 k_2^3} \frac{|\alpha|^2}{\Lambda^3} \frac{p^{3/2+i\varepsilon}}{2i\lambda(\frac{3}{2} - i\varepsilon)} \left(\frac{1}{\frac{3}{2} + i\varepsilon} - \frac{p^2 - \chi^2}{4p^2} \right) \frac{e^{-\pi\varepsilon}}{\cosh \pi\varepsilon}. \quad (5.8)$$

One can now evaluate the μ -integral analytically, closing the contour in the upper half plane and applying using the residue theorem:

$$\begin{aligned} & \int_{-\infty}^{\infty} \frac{p^{i\varepsilon}}{\frac{3}{2} - i\varepsilon} \left(\frac{1}{\frac{3}{2} + i\varepsilon} - \frac{p^2 - \chi^2}{4p^2} \right) \frac{e^{-\pi\varepsilon}}{\cosh \pi\varepsilon} d\varepsilon \\ &= -\frac{2i}{3} p^{-3/2} \left(p + \log p + \pi i - \sum_{k=0}^{\infty} \frac{p^{-1-k}}{k+1} + \frac{p^2 + 3\chi^2}{4} \sum_{k=0}^{\infty} \frac{p^{-1-k}}{k+2} \right), \\ &= -\frac{2i}{3} p^{-3/2} \left[p + \log(p-1) + \pi i - \frac{p^2 + 3\chi^2}{4} \left(1 + p \log \frac{p-1}{p} \right) \right], \end{aligned} \quad (5.9)$$

giving

$$\begin{aligned} B_{1\text{-loop},-+}^{(\lambda)}(k_1, k_2, k_3) &\simeq -\frac{1}{192\pi k_1^3 k_2^3} \frac{|\alpha|^2}{\Lambda^3} \frac{\prod_{\epsilon_1, \epsilon_2 = \pm} \sqrt{\lambda + \epsilon_1 \mu_1 + \epsilon_2 \mu_2}}{\lambda^2} \\ &\times \left[p + \log(p-1) + \pi i - \frac{p^2 + 3\chi^2}{4} \left(1 + p \log \frac{p-1}{p} \right) \right]. \end{aligned} \quad (5.10)$$

In terms of the properly normalized bispectrum:

$$\begin{aligned} F_{1\text{-loop},-+}^{(\lambda)} &\simeq \frac{5}{36\pi} \frac{|\alpha|^2}{\Lambda^2} \frac{\prod_{\epsilon_i} \sqrt{\lambda + \epsilon_1 \mu_1 + \epsilon_2 \mu_2}}{\lambda(p^3 + 3\chi^2 p + 4)} \left[p + \log(p-1) - \frac{p^2 + 3\chi^2}{4} \left(1 + p \log \frac{p-1}{p} \right) \right], \\ &\xrightarrow{p \gg 1} \frac{5}{32\pi} \frac{|\alpha|^2}{\Lambda^2} \frac{\prod_{\epsilon_i} \sqrt{\lambda + \epsilon_1 \mu_1 + \epsilon_2 \mu_2}}{\lambda p^2} \left(1 + \frac{2 + 24 \log p}{27p} - \frac{5 + 16\chi^2}{6p^2} + \dots \right), \end{aligned} \quad (5.11)$$

where we also include the contribution from the complex conjugate.

By combining eq. (5.5) with eq. (5.11) we have approximately B_{-+} . This contribution contains an oscillatory signal on top of a smooth background. If this was the tree level exchange of [22] or [24] then we would have successfully calculated the dominant contribution to the bispectrum. However, recall from section 4.3 that we B_{++} is not suppressed in the region $\mu \simeq \lambda$, which we must include in the loop integration. Therefore, we must take into account a further smooth background from the B_{++} diagram.

The tree level amplitude for B_{++} has been split into $B_{++,\text{NA}}^{(\pm)}$ and $B_{++,\text{A}}^{(\pm)}$ in eq. (4.26). According to section 4.3, $B_{++,\text{NA}}^{(-)}$ is always exponentially suppressed and can be neglected. For $B_{++,\text{NA}}^{(+)}$, we use the following hypergeometric function identity [49, eq. (15.8.4)]:

$$\begin{aligned} \mathbf{F}_{i\mu}^\rho(-p+i\epsilon) = & \Gamma\left(\frac{\rho+i\mu, \rho-i\mu}{\frac{1}{2}+\rho}\right) \left[\Gamma\left(\frac{\frac{1}{2}+\rho, \frac{1}{2}-\rho}{\frac{1}{2}+i\mu, \frac{1}{2}-i\mu}\right) F\left(\frac{\rho+i\mu, \rho-i\mu}{\frac{1}{2}+\rho}; \frac{1-p}{2}\right) \right. \\ & \left. + \Gamma\left(\frac{\frac{1}{2}+\rho, -\frac{1}{2}+\rho}{\rho+i\mu, \rho-i\mu}\right) \left(\frac{1-p}{2}+i\epsilon\right)^{1/2-\rho} F\left(\frac{\frac{1}{2}+i\mu, \frac{1}{2}-i\mu}{\frac{3}{2}-\rho}; \frac{1-p}{2}\right) \right]. \end{aligned} \quad (5.12)$$

For $\rho = -3/2 + n - i\lambda$, the Stirling approximation implies that

$$\begin{aligned} \Gamma\left(\frac{\frac{1}{2}+\rho, \frac{1}{2}-\rho}{\frac{1}{2}+i\mu, \frac{1}{2}-i\mu}\right) & \simeq -i(-1)^n e^{-\pi(\lambda-\mu)}, \\ \left| \Gamma\left(\frac{\frac{1}{2}+\rho, -\frac{1}{2}+\rho}{\frac{1}{2}+i\mu, \frac{1}{2}-i\mu}\right) \left(\frac{1-p}{2}+i\epsilon\right)^{1/2-\rho} \right| & \sim e^{-\pi(2\lambda-\mu)}. \end{aligned} \quad (5.13)$$

Consequently, the second term is suppressed by $e^{-\pi\lambda}$ compared to the first term, and we have

$$(-1)^n \mathbf{F}_{i\mu}^{-\frac{3}{2}+n-i\lambda}(-p+i\epsilon) \simeq -ie^{-\pi(\lambda-\mu)} \mathbf{F}_{i\mu}^{-\frac{3}{2}+n-i\lambda}(p) \quad (5.14)$$

$$B_{\text{tree},++,\text{NA}}^{(+)}(k_1, k_2, k_3; \lambda + \epsilon) \simeq ie^{\pi\epsilon} \bar{B}_{\text{tree},-+}^{(-)}(k_1, k_2, k_3; \lambda + \epsilon), \quad (5.15)$$

where we changed variables to $\mu = \lambda + \epsilon$, and in the last line we used eqs. (4.23) and (4.29) to relate the two amplitudes. The integral over ϵ can now be evaluated explicitly in a similar manner to give

$$\begin{aligned} F_{1\text{-loop},++,\text{NA}}^{(\lambda)} & \simeq \frac{5}{36\pi} \frac{|\alpha|^2}{\Lambda^2} \frac{\prod_{\epsilon_i} \sqrt{\lambda + \epsilon_1\mu_1 + \epsilon_2\mu_2}}{\lambda(p^3 + 3\chi^2 p + 4)} \left[p - \log(p+1) + \frac{p^2 + 3\chi^2}{4} \left(1 - p \log \frac{p+1}{p} \right) \right] \\ & \xrightarrow{p \gg 1} \frac{5}{32\pi} \frac{|\alpha|^2}{\Lambda^2} \frac{\prod_{\epsilon_i} \sqrt{\lambda + \epsilon_1\mu_1 + \epsilon_2\mu_2}}{\lambda p^2} \left(1 - \frac{2 + 24 \log p}{27p} - \frac{5 + 16\chi^2}{6p^2} \right). \end{aligned} \quad (5.16)$$

Finally, the tree level contribution to $B_{++,\text{A}}^{(\pm)}$ has been calculated exactly in appendix D. To obtain an approximate expression we expand eq. (D.2), with a useful identity derived in

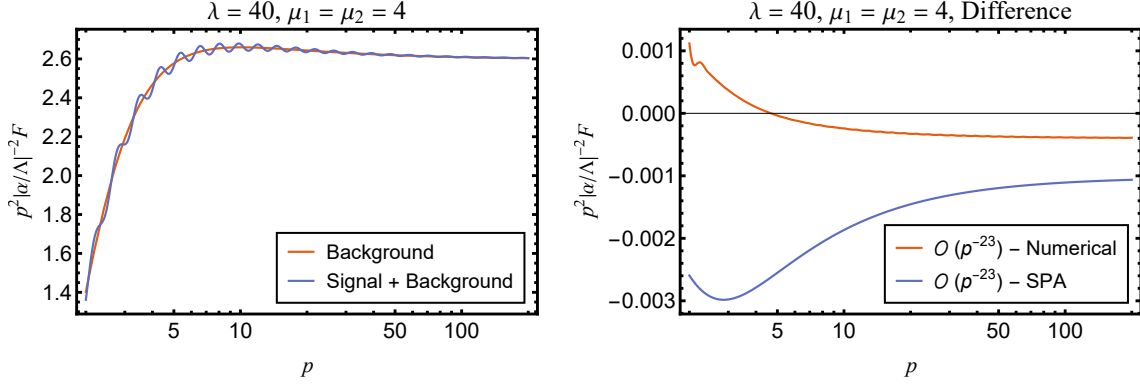


Figure 11. (Left) The one-loop smooth background coming from the resonance limit of F_{-+} , $F_{++,\text{NA}}$ and $F_{++,\text{A}}$ for $\lambda = 40$ and $\mu_1 = \mu_2 = 4$, rescaled by p^2 . (Right) The difference between three different calculations: (i) the analytic sum over poles up to $\mathcal{O}(p^{-23})$ (see section 5.3 and appendix E); (ii) numerical evaluation of eq. (3.16); (iii) the SPA result eq. (5.21). For p away from 2, both the numerical result and the improved SPA result agree with the analytic sum within 0.1%.¹⁰

eq. (D.12), around $\mu = \lambda + \varepsilon$. Assuming $\mu, \lambda \gg 1$ we obtain

$$B_{++,\text{A}}^{(\pm)}(k_1, k_2, k_3) \simeq \frac{1}{16k_1^3 k_2^3} \frac{|\alpha|^2}{\Lambda^3} \frac{p^{-1}}{\lambda(\frac{9}{4} + \varepsilon^2)(\frac{1}{2} \mp i\varepsilon)} \sum_{n=0}^1 \hat{c}_n F\left(1 + n, \frac{1}{2} \mp i\varepsilon; -\frac{1}{p}\right), \quad (5.17)$$

with $\hat{c}_0 := p^2 - 2Q$, $\hat{c}_1 := Q$, and $Q := \frac{1}{4}(p^2 - \chi^2)$. It turns out that the function

$$\frac{1}{\frac{1}{2} \mp i\varepsilon} F\left(1 + n, \frac{1}{2} \mp i\varepsilon; -\frac{1}{p}\right) \quad (5.18)$$

is meromorphic in ε with poles at $1/2 \pm i\varepsilon + n = 0$ ($n = 0, 1, 2, \dots$), and decays as $\mathcal{O}(\varepsilon^{-1})$ as $\varepsilon \rightarrow \infty$. The integration over ε can thus be closed on either the upper or the lower half plane:

$$\begin{aligned} \int_{-\infty}^{\infty} \frac{d\varepsilon}{(\frac{9}{4} + \varepsilon^2)(\frac{1}{2} \mp i\varepsilon)} F\left(1 + n, \frac{1}{2} \mp i\varepsilon; -\frac{1}{p}\right) &= \frac{\pi}{3} F\left(1 + n, 2; -\frac{1}{p}\right) \\ &= \frac{2\pi}{3} \begin{cases} 1 - p \log \frac{p+1}{p}, & n = 0, \\ -\frac{p^2}{p+1} + p^2 \log \frac{p+1}{p}, & n = 1. \end{cases} \end{aligned} \quad (5.19)$$

¹⁰The deviation in the orange line at large p is due to the $\tilde{F}_{++,\text{A},1\text{-loop}}^{(s_1, s_2 \mu_{12}, k)}$ series which, in principle, requires a full resummation even at $\mathcal{O}(p^{-2})$. In making the plot, we include terms up to $k = 40$. The details are discussed at the end of appendix E.

We thus have

$$F_{1\text{-loop}, ++, A}^{(\lambda)} \simeq -\frac{5}{72\pi} \frac{|\alpha|^2}{\Lambda^2} \frac{\prod_{\epsilon_i} \sqrt{\lambda + \epsilon_1 \mu_1 + \epsilon_2 \mu_2}}{\lambda(p^3 + 3\chi^2 p + 4)} \left[(p^2 + 3\chi^2) \left(1 - p \log \frac{p+1}{p} \right) + \frac{p^2 - \chi^2}{p+1} \right] \\ \xrightarrow{p \gg 1} -\frac{5}{48\pi} \frac{|\alpha|^2}{\Lambda^2} \frac{\prod_{\epsilon_i} \sqrt{\lambda + \epsilon_1 \mu_1 + \epsilon_2 \mu_2}}{\lambda p^2} \left(1 - \frac{8}{9p} + \frac{5 - 16\chi^2}{6p^2} + \dots \right). \quad (5.20)$$

Combining eqs. (5.11), (5.16) and (5.20) gives an approximate expression for the smooth background

$$F_{1\text{-loop}, \text{bkg}} \simeq \frac{5}{18\pi} \frac{|\alpha|^2}{\Lambda^2} \frac{\prod_{\epsilon_1, \epsilon_2 = \pm} \sqrt{\lambda + \epsilon_1 \mu_1 + \epsilon_2 \mu_2}}{\lambda(p^3 + 3\chi^2 p + 4)} \\ \times \left[p - \frac{1}{2} \log \frac{p+1}{p-1} - \frac{p^2 + 3\chi^2}{4} \left(1 - \frac{p}{2} \log \frac{p+1}{p-1} \right) - \frac{p^2 - \chi^2}{4(p+1)} \right] \\ \xrightarrow{p \gg 1} \frac{5}{24\pi} \frac{|\alpha|^2}{\Lambda^2} \frac{\prod_{\epsilon_1, \epsilon_2 = \pm} \sqrt{\lambda + \epsilon_1 \mu_1 + \epsilon_2 \mu_2}}{\lambda} p^{-2} \left(1 + \frac{4}{9p} - \frac{5 + 8\chi^2}{3p^2} + \dots \right). \quad (5.21)$$

The shape of the background is shown in figure 11 and the left panel of figure 12. One can see that the resonance background is an order of magnitude larger than the signal for $\lambda = 40$ and $\mu_1 = \mu_2 = 4$. It will thus be detected before the signal in the one-loop dominated scenario. Fortunately, since the background is a smooth function of p , the non-analytic signal can be separated from it as long as the experimental error is smaller than the amplitude of the oscillations. This detectability issue will be further discussed in section 5.4.

5.3 Beyond stationary phase approximation

Besides the SPA result eqs. (3.32) and (5.5), the spectral representation also allow us to expand the exact result for the one-loop amplitude as an infinite sum over analytic terms, which is effectively an expansion in $1/p$. To see how this works, we start with the integration for B_{-+} given by

$$B_{-+, 1\text{-loop}}^{(-)}(k_1, k_2, k_3) = \int_0^\infty \rho_{\mu_1 \mu_2}^{\text{dS}}(\mu) B_{-+, \text{tree}}^{(-)}(k_1, k_2, k_3; \mu) d\mu, \quad (5.22)$$

where $B_{-+, \text{tree}}^{(-)}$ is given by eq. (4.23).

There is one difficulty in applying the residue theorem to eq. (5.22): in the complex plane the integrand blows up as $\text{Im } \mu \rightarrow \pm\infty$. This is analogous to the situation in flat space where the integrand is a trigonometric function, i.e. $\cos(x) \sim e^{ix} + e^{-ix}$. The integrand blows up in both the upper and lower half plane, but once we split the integrand up into complex exponentials the contour can be closed in both terms individually.

To achieve such separation for the hypergeometric function we rewrite $\mathbf{F}_{i\mu}^\rho(p)$ in eq. (4.23)

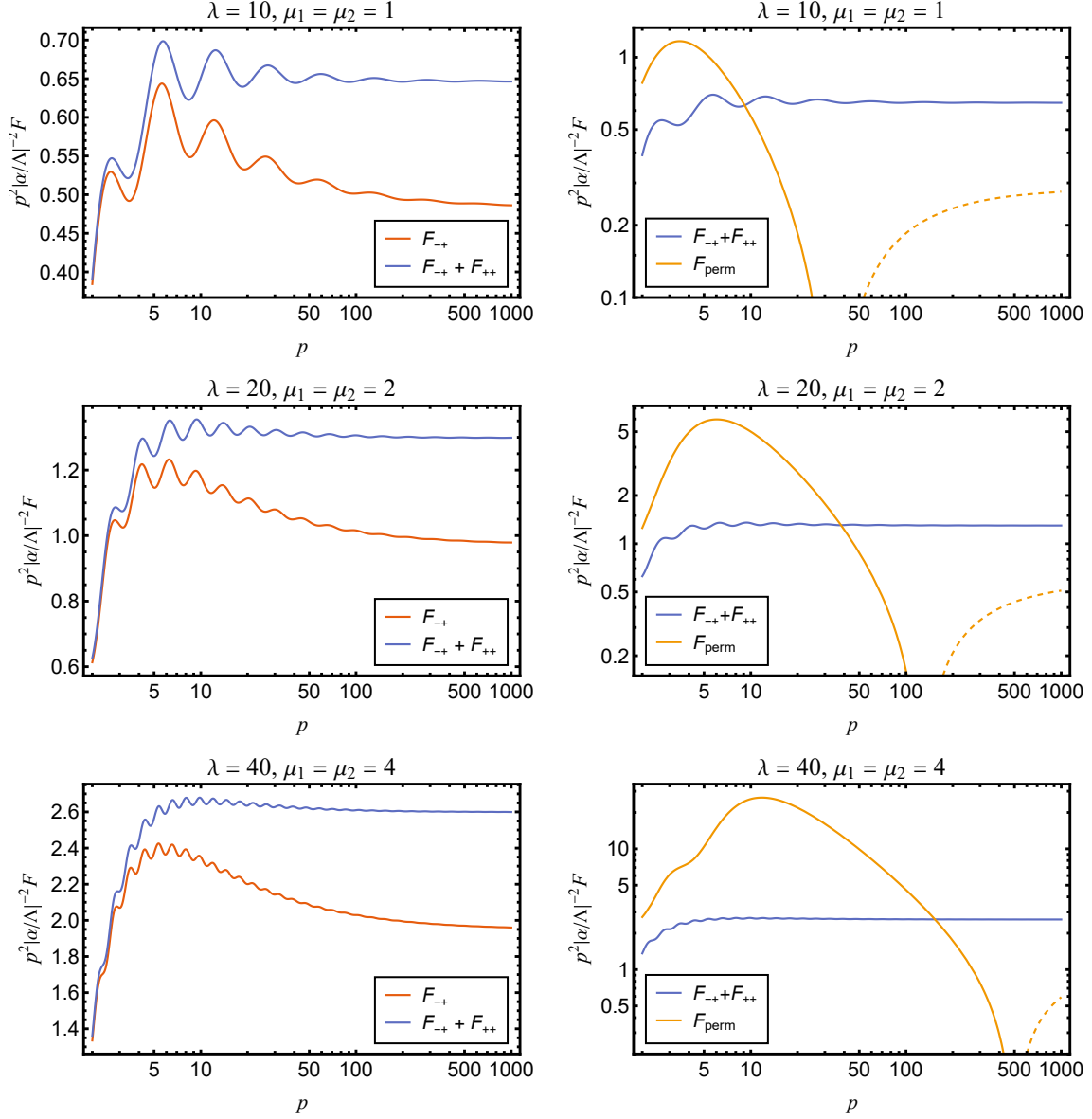


Figure 12. Different contributions to the one-loop correlators for various λ and μ_1, μ_2 , rescaled by p^2 . (Left) The contribution from F_{-+} and F_{++} . (Right) The contribution from the two permuted diagrams where the soft momentum k_3 is contracted with the 3-point vertex in figure 7. Negative values are shown in dashed lines.

using the following identity [49, eq. (15.8.2)]:

$$\mathbf{F}_{i\mu}^\rho(p) = \frac{1}{2\sqrt{\pi}} \left[2^{2i\mu} \Gamma(i\mu) \Gamma(\rho - i\mu) \tilde{\mathbf{F}}_{i\mu}^{\rho-i\mu}(p) + (\mu \rightarrow -\mu) \right], \quad (5.23)$$

where

$$\tilde{\mathbf{F}}_{i\mu}^s(p) := \left(\frac{p-1}{2}\right)^{-s} F\left(s, \frac{1}{2} - i\mu; \frac{2}{1-p}\right). \quad (5.24)$$

Since the integrand in eq. (5.22) is an even function in μ , we then have

$$B_{-+,1\text{-loop}}^{(-)}(k_1, k_2, k_3) = \int_{-\infty}^{\infty} \rho_{\mu_1\mu_2}^{\text{dS}}(\mu) \tilde{B}_{-+,\text{tree}}^{(-)}(k_1, k_2, k_3; \mu) d\mu, \quad (5.25)$$

$$\begin{aligned} \tilde{B}_{-+,\text{tree}}^{(-)}(k_1, k_2, k_3; \mu) := & -\frac{1}{4\sqrt{\pi}k_1^3k_2^3} \frac{|\alpha|^2}{\Lambda^3} \frac{2^{2i\mu}\lambda e^{\pi\lambda}}{\left(\frac{3}{2} + i\lambda\right)^2 + \mu^2} \sum_{n=0}^2 \frac{d_n}{2^n} \tilde{\mathbf{F}}_{i\mu}^{-\frac{3}{2}+n+i\lambda-i\mu}(p) \\ & \times \Gamma\left(\begin{matrix} i\mu, -\frac{3}{2} + n + i\lambda - i\mu, \frac{1}{2} - i\lambda + i\mu, \frac{1}{2} - i\lambda - i\mu \\ 1 - i\lambda \end{matrix}\right). \end{aligned} \quad (5.26)$$

The integrand in eq. (5.25) has improved asymptotic behavior compared to the one in eq. (5.22). In particular, for $p > 1$, $\text{Re } \mu = \mu_*$ and $\text{Im } \mu = M$, we have the following asymptotic bound as $M \rightarrow +\infty$ ¹¹:

$$\rho_{\mu_1\mu_2}^{\text{dS}}(\mu) \tilde{B}_{-+,\text{tree}}^{(-)}(k_1, k_2, k_3; \mu) \sim \mathcal{P}(\lambda, \mu, \mu_1, \mu_2) M^{-\frac{3}{2}-i\lambda} \left(p + \sqrt{p^2 - 1}\right)^{-M}, \quad (5.27)$$

where

$$\mathcal{P}(\lambda, \mu, \mu_1, \mu_2) = \frac{\sin \pi\left(\frac{3}{2} + i\mu\right)}{\sin \pi\left(\frac{1}{2} - i\lambda + i\mu\right) \prod_{\epsilon_1, \epsilon_2 = \pm} \sin \pi\left[\frac{3}{4} + \frac{i}{2}(\mu + \epsilon_1\mu_1 + \epsilon_2\mu_2)\right]} \quad (5.28)$$

is bounded if μ does not coincide with the zeros of any sine functions in the denominator. Therefore, we can close the contour in the upper μ -plane.

The analytic structure of the integrand in eq. (5.25) is illustrated in figure 13 and the position of the poles are listed in table 2, where the simplified notation $\Delta\mu := |\mu_1 - \mu_2|$ is used. The p -dependence of each pole for large p can be read off from (5.24) directly:

$$\text{Res}_{\mu_* + i\delta} \tilde{B}_{-+,\text{tree}}^{(-)} \xrightarrow{p \rightarrow \infty} p^{3/2 - \delta - i(\lambda - \mu_*)}, \quad (5.29)$$

where the imaginary part of the exponent is given by $\lambda - \mu_*$, while poles with larger imaginary part, δ , are more suppressed in the squeezed limit.

For $\lambda, \mu_1, \mu_2, \lambda - \mu_{12} \gg 1$, one can use the Stirling approximation on all the Γ functions in eq. (5.25). By doing so, we find that all but three series of poles are exponentially suppressed, where the unsuppressed poles have either $\mu_* = \lambda$ or $\mu_* = \mu_{12}$. The former case corresponds

¹¹For the gamma functions, the asymptotic property $\Gamma(a - i\mu) \sim (-i\mu)^a \Gamma(-i\mu)$ and the identity $\Gamma(a + i\mu)\Gamma(1 - a - i\mu) = \pi \csc \pi(a + i\mu)$ are used. For $\tilde{\mathbf{F}}_{i\mu}^{\rho - i\mu}$, the asymptotic expansion is given by eq. (B.5), where we leave its derivation to appendix B.

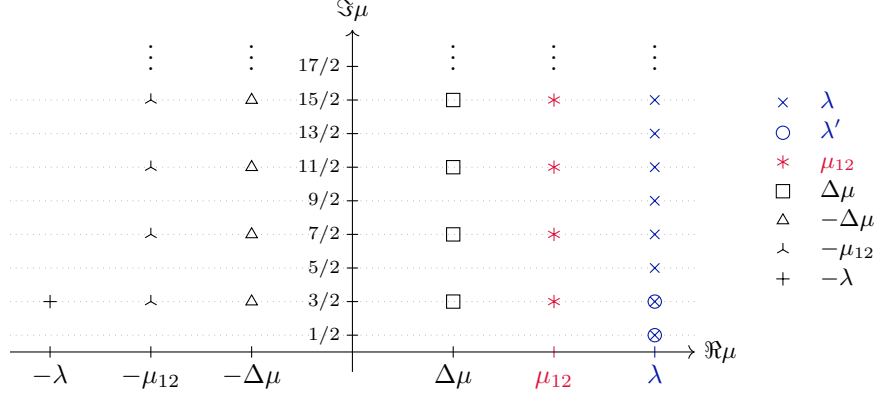


Figure 13. The analytic structure of the integrand in eq. (5.25) in the upper half plane. The two colored columns are poles with residues that are not exponentially suppressed. Given the bound eq. (5.27), the integral can be represented as a sum over the residues of all these poles for $p > 1$.

Series ($\text{Re } \mu$)	source	μ	residues
λ	$\tilde{B}_{-+, \text{tree}}^{(-)}$, $\Gamma(\frac{1}{2} - i\lambda + i\mu)$	$\lambda + (\frac{1}{2} + k)i$	$\mathcal{O}(1)$
λ'	$\tilde{B}_{-+, \text{tree}}^{(-)}$, $\Gamma(-\frac{3}{2} + n + i\lambda - i\mu)$	$\lambda + \frac{1}{2}i, \lambda + \frac{3}{2}i$	$\mathcal{O}(1)$
$-\lambda$	$\tilde{B}_{-+, \text{tree}}^{(-)}$, $\frac{1}{(3/2 + i\lambda)^2 + \mu^2}$	$-\lambda + \frac{3}{2}i$	$\mathcal{O}(e^{-\pi\lambda})$
μ_{12}	$\rho_{\mu_1\mu_2}^{\text{dS}}$, $\Gamma[\frac{3}{4} + \frac{i}{2}(\mu - \mu_{12})]$	$\mu_{12} + (\frac{3}{2} + 2k)i$	$\mathcal{O}(1)$
$-\mu_{12}$	$\rho_{\mu_1\mu_2}^{\text{dS}}$, $\Gamma[\frac{3}{4} + \frac{i}{2}(\mu + \mu_{12})]$	$-\mu_{12} + (\frac{3}{2} + 2k)i$	$\mathcal{O}(e^{-\pi\mu_{12}})$
$\Delta\mu$	$\rho_{\mu_1\mu_2}^{\text{dS}}$, $\Gamma[\frac{3}{4} + \frac{i}{2}(\mu - \Delta\mu)]$	$\Delta\mu + (\frac{3}{2} + 2k)i$	$\mathcal{O}(e^{-2\pi\mu_2})$
$-\Delta\mu$	$\rho_{\mu_1\mu_2}^{\text{dS}}$, $\Gamma[\frac{3}{4} + \frac{i}{2}(\mu + \Delta\mu)]$	$-\Delta\mu + (\frac{3}{2} + 2k)i$	$\mathcal{O}(e^{-\pi\mu_{12}})$

Table 2. The position of poles of the integrand in eq. (5.25) in the upper half plane and their sources ($n = 0, 1, 2$ and $k \in \mathbb{N}$). The residues at these poles are estimated logarithmically for $\lambda, \mu_1, \mu_2, \lambda - \mu_{12} \gg 1$, where $\mu_1 > \mu_2$ is assumed w.l.o.g. For the logarithmic estimation of all ranges of λ , see table 5.

to the resonance limit, and contributes to the bispectrum as¹²

$$F_{-+, 1\text{-loop}}^{(-, \lambda)} \xrightarrow{p \rightarrow \infty} p^{-2}, \quad p^{-3}, \quad p^{-3} \log p, \quad p^{-4}, \quad \dots, \quad (5.30)$$

while the latter case corresponds to the threshold limit, and contributes to the bispectrum as

$$F_{-+, 1\text{-loop}}^{(-, \mu_{12})} \xrightarrow{p \rightarrow \infty} p^{-3-i(\lambda-\mu_{12})}, \quad p^{-5-i(\lambda-\mu_{12})}, \quad p^{-7-i(\lambda-\mu_{12})}, \quad \dots. \quad (5.31)$$

In particular, when the contribution from one pole is considered, the rest of eq. (5.25) can be approximated as in eq. (3.28). This further justifies the use of eq. (5.2) as a leading-order

¹²The $\log p$ at p^{-3} comes from the overlapping pole at $\mu = \lambda + \frac{3}{2}i$, while the other apparent overlapping pole at $\mu = \lambda + \frac{1}{2}i$ does not contain $\log p$. See appendix E for more details.

approximation.

The same technique can also be used to evaluate $B_{++,\text{NA}}^{(\pm)}$ and $B_{++,\text{A}}^{(\pm)}$ for the one-loop model. For $B_{++,\text{NA}}^{(\pm)}$, the following identity is used to obtain an integrand with an improved asymptotic behavior:

$$\mathbf{F}_{i\mu}^\rho(-p+i\epsilon) = \frac{e^{-\rho\pi i}}{2\sqrt{\pi}} \left[2^{2i\mu} e^{-\pi\mu} \Gamma(i\mu) \Gamma(\rho-i\mu) \tilde{\mathbf{F}}_{i\mu}^{\rho-i\mu}(p) + (\mu \rightarrow -\mu) \right], \quad (5.32)$$

while for $B_{++,\text{A}}^{(\pm)}$, eq. (D.2) is already in the desired form. Eventually:

$$B_{++,\text{NA/A},1\text{-loop}}^{(\pm)}(k_1, k_2, k_3) = \int_{-\infty}^{\infty} \rho_{\mu_1\mu_2}^{\text{dS}}(\mu) \tilde{B}_{++,\text{NA/A},\text{tree}}^{(\pm)}(k_1, k_2, k_3; \mu) d\mu, \quad (5.33)$$

$$\begin{aligned} \tilde{B}_{++,\text{NA},\text{tree}}^{(\pm)}(k_1, k_2, k_3; \mu) &:= -\frac{i}{4\sqrt{\pi}k_1^3k_2^3} \frac{|\alpha|^2}{\Lambda^3} \frac{2^{2i\mu}\lambda e^{-\pi\mu}}{\left(\frac{3}{2} \mp i\lambda\right)^2 + \mu^2} \sum_{n=0}^2 \frac{d_n}{2^n} \tilde{\mathbf{F}}_{i\mu}^{-\frac{3}{2}+n \mp i\lambda-i\mu}(p) \\ &\quad \times \Gamma\left(\begin{matrix} i\mu, -\frac{3}{2}+n \mp i\lambda-i\mu, \frac{1}{2} \pm i\lambda+i\mu, \frac{1}{2} \pm i\lambda-i\mu \\ 1 \pm i\lambda \end{matrix}\right), \end{aligned} \quad (5.34)$$

$$\begin{aligned} \tilde{B}_{++,\text{A},\text{tree}}^{(\pm)}(k_1, k_2, k_3; \mu) &:= \frac{i}{8k_1^3k_2^3} \frac{|\alpha|^2}{\Lambda^3} \frac{\lambda}{\mu \left[(\lambda^2 - \mu^2 - \frac{9}{4})^2 + 9\lambda^2 \right]} \sum_{n=0}^2 \frac{c_n^\pm}{2^n} \mathbf{H}_{n,i\mu}^{\pm i\lambda}(p) \\ &= \frac{i}{8k_1^3k_2^3} \frac{|\alpha|^2}{\Lambda^3} \frac{\lambda}{\mu \left[(\lambda^2 - \mu^2 - \frac{9}{4})^2 + 9\lambda^2 \right]} \sum_{n=0}^2 \frac{c_n^\pm}{2^n} \\ &\quad \times \sum_{m=0}^{\infty} \frac{(-)^m(m+1)_n \left(\frac{1}{2}+i\mu\right)_m}{\left(\frac{1}{2}+m \pm i\lambda+i\mu\right)(1+2i\mu)_m} \tilde{\mathbf{F}}_{i\mu}^{1+n+m}(p). \end{aligned} \quad (p > 3) \quad (5.35)$$

The full results for both the signal and all the backgrounds have an intricate form and can be found in appendix E.

5.4 Combinatorial backgrounds from permuted diagrams

Finally, there are also *combinatorial backgrounds* from permuted diagrams, where the soft momentum k_3 is contracted with the 3-point vertex in figure 7. These contributions can be obtained from B_{-+} and B_{++} by permuting $k_3 \rightarrow k_1, k_2$. In terms of p and χ :

$$\begin{cases} p' = \frac{p-\chi+2}{p+\chi}, \\ \chi' = -\frac{p-\chi-2}{p+\chi} \end{cases} \quad \text{for } k_3 \rightarrow k_1; \quad \begin{cases} p' = \frac{p+\chi+2}{p-\chi}, \\ \chi' = \frac{p+\chi-2}{p-\chi} \end{cases} \quad \text{for } k_3 \rightarrow k_2. \quad (5.36)$$

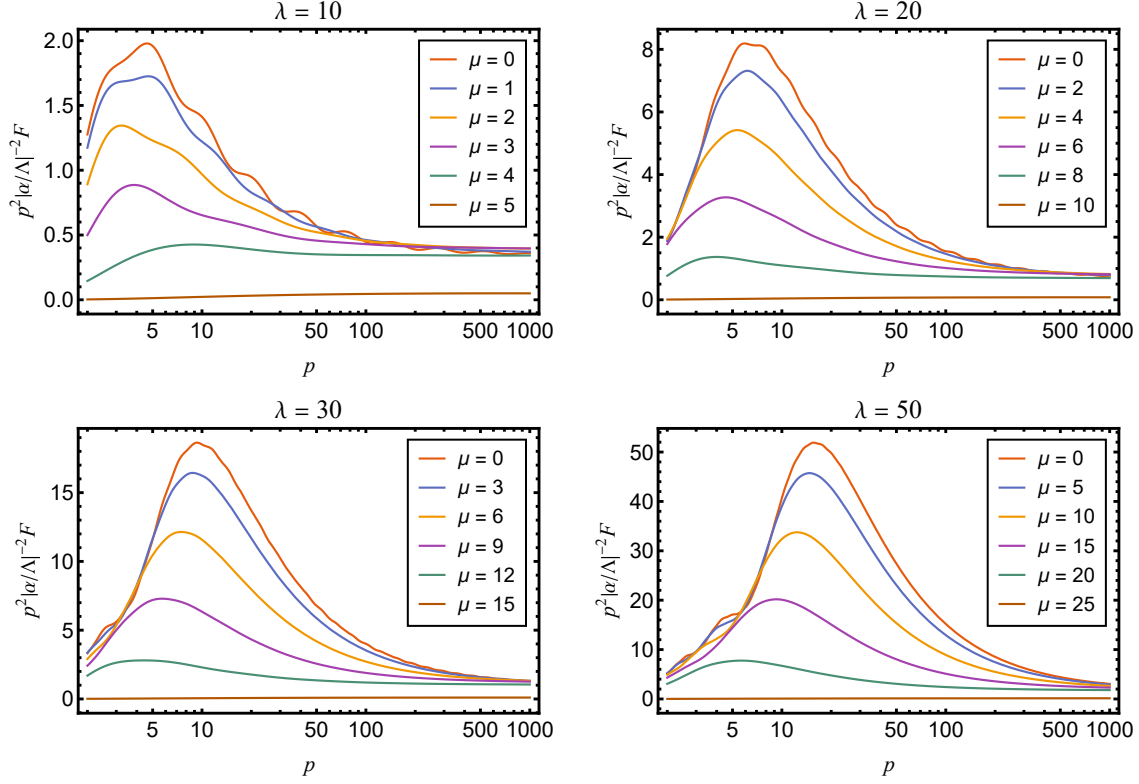


Figure 14. The full one-loop bispectrum including the combinatorial background for various λ and $\mu_1 = \mu_2 = \mu$ rescaled by p^2 . The bumps in the diagrams are artifacts of the p^2 rescaling.

Unfortunately, since large p corresponds to $p' \rightarrow 1$, both SPA and the analytic method described in previous sections do not apply. Instead, one needs to expand the tree-level amplitudes around $p' \rightarrow 1$. According to the analysis in section 4.2, in this limit, all stationary phase points either disappear or approach fixed values. In particular, the creation and annihilation time become coincident for B_{-+} . Consequently, $F(k_2, k_1, k_3) + F(k_3, k_1, k_2)$ does not oscillate but falls off as p^{-2} in the squeezed limit as local interactions, i.e. the permuted diagrams only contribute to the analytic part of the amplitude at large p .

Nevertheless, this expansion is only of theoretical interest, and we must resort to numerically integrating the exact tree level amplitudes over the spectral density. This is because unless $p \gg \lambda, \mu$, the number of terms needed to be included in the expansion is $\mathcal{O}(\lambda/p, \mu/p)$. For $\lambda, \mu \sim \mathcal{O}(10)$, this would require either $\mathcal{O}(10)$ numbers of higher order terms or $p \gg \mathcal{O}(10)$ as illustrated in the right panel of figure 12.

It is difficult in practice to detect the NG, and one has to identify the non-analyticity using data from moderate values of p , where the theory predicts a more complicated p -dependence as shown in figure 14.

Given the large analytic backgrounds from both the resonance limit and permuted diagrams, it is natural to ask whether the non-analytic signal can be separated from them. This

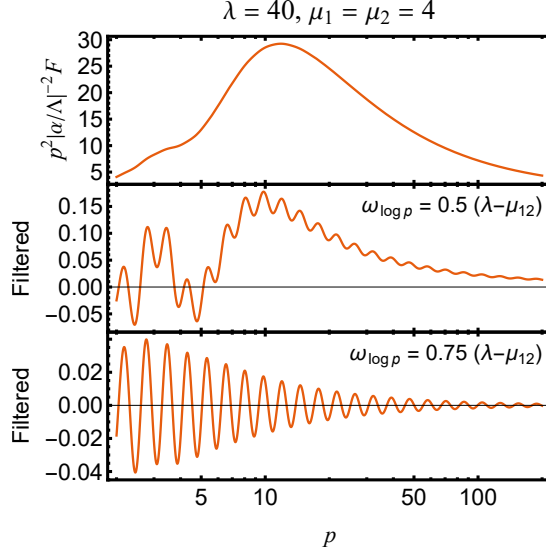


Figure 15. An example of applying high-pass filter to the full one-loop bispectrum. The Blackman-Harris window has been used in the filter. For details of how to implement the high pass filter, the reader may consult [26]. With a cutoff frequency at $0.5(\lambda - \mu_{12})$, oscillatory patterns from both the signal and the permuted diagrams can pass the filter, while a slightly higher cutoff frequency will only allow the oscillatory signal to pass.

turns out not to be a serious problem as both backgrounds are mostly smooth functions in p compared to the highly-oscillatory signal. As shown in ref. [26], one can apply a high-pass filter to extract the signal from the curve (figure 15). To observe the signal we only require that the experimental sensitivity, F_{\min} , be sufficient to resolve the oscillations, i.e.

$$|\tilde{F}_{\text{osc}}| \gtrsim F_{\min}, \quad (5.37)$$

which is not affected by the existence of backgrounds, except in the sense that the large signal to background ratio, combined with the fact that we are yet to identify any NGs, can set an upper bound on the signal.

5.5 Higher order corrections at one-loop

At one-loop there are also higher order contributions at each $\mathcal{O}(\alpha^{2n})$ from inserting equal numbers of $\chi_1 \chi_2$ and $\bar{\chi}_1 \bar{\chi}_2$ vertices. Resumming these contributions is equivalent to solving the full linearized equations of motion for $\chi_{1,2}$:

$$\left[-\square + \mathbf{M}^2(\eta) + \frac{9}{4} \right] \begin{pmatrix} \chi_1 \\ \bar{\chi}_2 \end{pmatrix} = 0, \quad \mathbf{M}^2(\eta) = \begin{bmatrix} \mu_1^2 & \bar{\alpha}(-\eta)^{i\lambda} \\ \alpha(-\eta)^{-i\lambda} & \mu_2^2 \end{bmatrix}. \quad (5.38)$$

In momentum space:

$$\left[\partial_\eta^2 - \frac{2}{\eta} \partial_\eta + k^2 + \frac{\mathbf{M}^2(\eta) + 9/4}{\eta^2} \right] \begin{pmatrix} \chi_1 \\ \bar{\chi}_2 \end{pmatrix} = 0. \quad (5.39)$$

It turns out that it is more intuitive to work with the proper time $t := -\log(-\eta)$, so that the equation becomes

$$[\partial_t^2 + k^2 \eta^2(t) + \mathbf{M}^2(t)] \begin{pmatrix} \chi_1 \\ \bar{\chi}_2 \end{pmatrix} = 0. \quad (5.40)$$

Consider the case when $\lambda, \mu_1, \mu_2 \gg 1$, so that the expansion of the universe can be neglected near a pivot time, η_* . In this case, the general solution is given by

$$\begin{bmatrix} \chi_1(t) \\ \bar{\chi}_2(t) \end{bmatrix} \simeq \sum_{n=1}^4 c_n \begin{bmatrix} \chi_1^{(n)} e^{-i(\omega_n + \lambda/2)t} \\ \bar{\chi}_2^{(n)} e^{-i(\omega_n - \lambda/2)t} \end{bmatrix}, \quad (5.41)$$

where ω_n are the four roots of the quartic equation

$$\left[\left(\omega + \frac{\lambda}{2} \right)^2 - \omega_{01}^2 \right] \left[\left(\omega - \frac{\lambda}{2} \right)^2 - \omega_{02}^2 \right] = |\alpha|^2, \quad \omega_{01,02} := \sqrt{k^2 \eta_*^2 + \mu_{1,2}^2}, \quad (5.42)$$

and $\chi_1^{(n)}, \bar{\chi}_2^{(n)}$ satisfy

$$\begin{bmatrix} (\omega_n + \frac{\lambda}{2})^2 - \omega_{01}^2 & -\bar{\alpha} \\ -\alpha & (\omega_n - \frac{\lambda}{2})^2 - \omega_{02}^2 \end{bmatrix} \begin{bmatrix} \chi_1^{(n)} \\ \bar{\chi}_2^{(n)} \end{bmatrix} = 0. \quad (5.43)$$

The structure of the solutions to eq. (5.42) for different values of λ , ω_{01} and ω_{02} are illustrated in figure 16.

Eq. (5.42) implies Parametric Resonance (PR) at some time during inflation [22]. This happens when any of ω_k has an imaginary part, i.e. $\lambda \simeq \omega_{01} + \omega_{02}$ or

$$-k\eta \simeq -k\eta_R := \frac{\prod_{\epsilon_1, \epsilon_2 = \pm} \sqrt{\lambda + \epsilon_1 \mu_1 + \epsilon_2 \mu_2}}{2\lambda}. \quad (5.44)$$

Physically, this corresponds to the time when λ can produce a $\chi_1 \chi_2$ pair on-shell. Around this time, ω_2 and ω_3 become nearly degenerate and are approximately given by

$$\omega_{2,3} \simeq -\frac{\omega_{01} - \omega_{02}}{2} \pm \frac{1}{2} \sqrt{(\lambda - \omega_{01} - \omega_{02})^2 - \frac{|\alpha|^2}{\omega_{01} \omega_{02}}}. \quad (5.45)$$

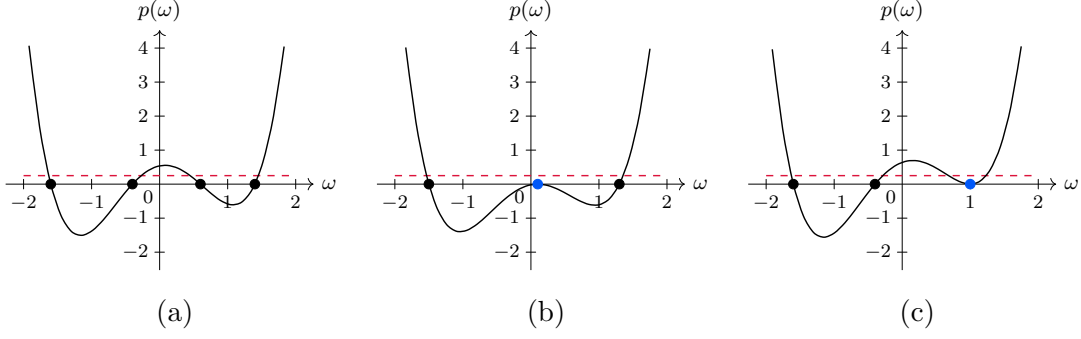


Figure 16. The condition for parametric resonance can be understood by the structure of the solutions to the quartic equation eq. (5.42). The solutions occur when the quartic crosses the dashed red line, and parametric resonance occurs when two of the solutions are complex. (a) For small α and general values of $\lambda, \omega_1, \omega_2$, there are 4 real solutions and the corrections to ω_k are $\mathcal{O}(\alpha^2)$; (b) when $\lambda = \omega_1 + \omega_2$, there are only two real solutions as the degenerate ω_k (blue) receives an $\mathcal{O}(\alpha)$ imaginary part (parametric resonance); (c) when $\lambda = |\omega_1 - \omega_2|$ or one of ω_{01}, ω_{02} is zero, there are 4 real solutions where the degenerate ω_k (blue) receives an $\mathcal{O}(\alpha)$ real part.

Therefore, the parametric oscillator is in resonance when

$$|\alpha|^2 \gtrsim \omega_{01}\omega_{02} |\lambda - \omega_{01} - \omega_{02}| \simeq \frac{\prod_{\epsilon_1, \epsilon_2 = \pm} (\lambda + \epsilon_1\mu_1 + \epsilon_2\mu_2)^2}{4[\lambda^2 - (\mu_1^2 - \mu_2^2)^2]} \delta t^2. \quad (5.46)$$

where we have plugged in $\eta = \eta_R e^{-\delta t}$. For α not too large, PR only persists over a finite period of time. During this period, the mode function is amplified by a factor $\mathcal{A}_R^{1/2}$, where:

$$\log \mathcal{A}_R \simeq 2 \int_{t_{\min}}^{t_{\max}} \omega_2(t) dt \simeq \frac{2\pi\lambda |\alpha|^2}{\prod_{\epsilon_1, \epsilon_2 = \pm} (\lambda + \epsilon_1\mu_1 + \epsilon_2\mu_2)}. \quad (5.47)$$

Consequently, for our calculations to be valid we should require this amplification to be small:

$$\log \mathcal{A}_R \ll 1, \quad \text{i.e. } |\alpha| \ll \alpha_{\text{PR}} := \sqrt{\frac{\prod_{\epsilon_1, \epsilon_2 = \pm} (\lambda + \epsilon_1\mu_1 + \epsilon_2\mu_2)}{2\pi\lambda}}. \quad (5.48)$$

For even larger α , PR may persist till the end of inflation, giving rise to a late-time behavior

$$|f_k(\eta)| \sim (-\eta)^{3/2 - \text{Im} \omega_n(0)}. \quad (5.49)$$

A simple power counting shows that, if any of $\text{Im} \omega_n(0) \geq 1$, i.e.:

$$|\alpha| \gtrsim \alpha_{\max} := \sqrt{\max_{-\frac{\lambda}{2} < \omega < \frac{\lambda}{2}} \left[\left(\omega + \frac{\lambda}{2} \right)^2 - \mu_1^2 \right] \left[\left(\omega - \frac{\lambda}{2} \right)^2 - \mu_2^2 \right]} \simeq \frac{\lambda^2}{4}, \quad (\mu_1, \mu_2 \ll \lambda), \quad (5.50)$$

there will be a late-time divergence in the perturbative calculation. This divergence will

eventually be cut off by the decrease of $\dot{\phi}_0$ over time until it can no longer sustain the resonance.

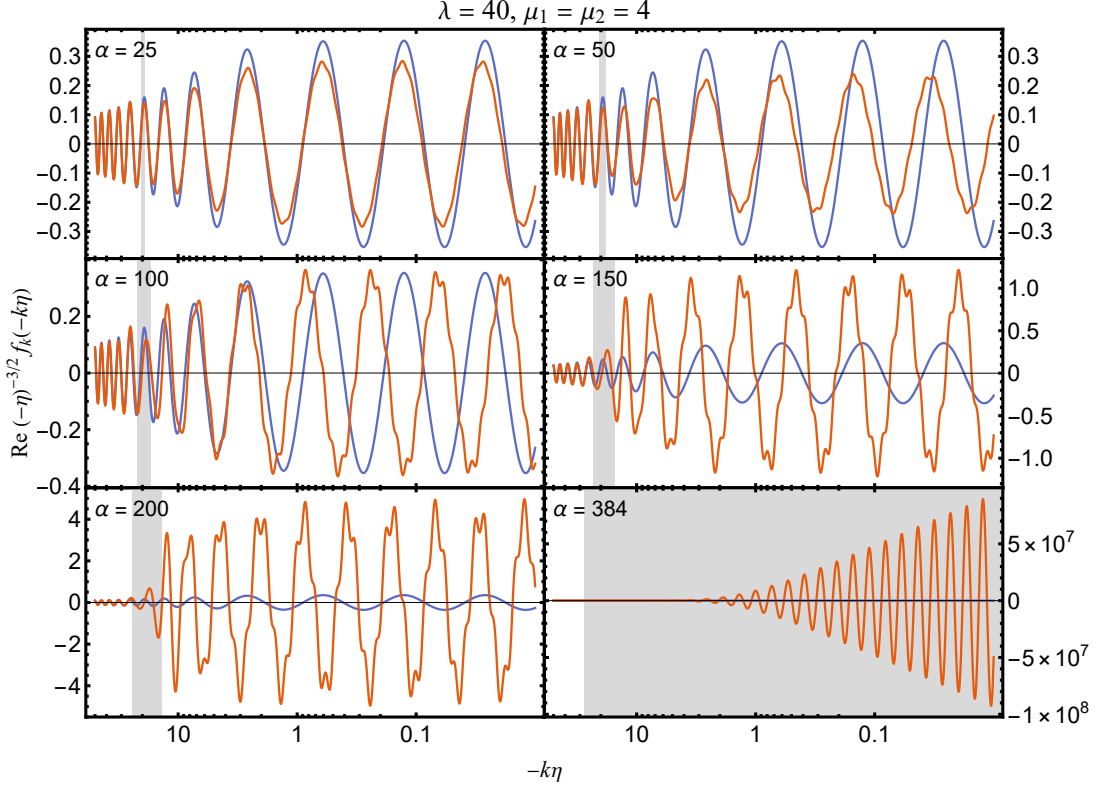


Figure 17. The numerical mode functions from the resummed equation of motion eq. (5.39) with $\lambda = 40$ and $\mu_1 = \mu_2 = 4$ for various α ($\alpha_{\text{PR}} \approx 99$, $\alpha_{\text{max}} = 384$). The blue line represents eq. (2.16) ($\alpha = 0$) for comparison. The regions of parametric resonance where eq. (5.42) has complex roots are marked gray.¹⁴

So far, we have been treating the universe expansion in the adiabatic approximation. This cannot predict the solutions near the beginning and the end of PR, where eq. (5.42) has degenerate roots and different modes evolve into each other. Here we also present the numerical solutions to eq. (5.39) in figure 17 for various α . This shows that our previous analysis applies qualitatively even beyond the adiabatic approximation.

To see how higher order corrections at one-loop affect the bispectrum, one has to evaluate eq. (3.10) with the corrected mode functions. Since de Sitter symmetry is badly broken by these corrections, the spectral representation method no longer applies. We can still understand its effects in the following two directions:

1. The energy as a function of time is corrected according to eq. (5.42). For $\mu_1 = \mu_2 = \mu$,

¹⁴For this particular parameter choice the late-time amplitude first decreases and then increases exponentially as α increases. This may not happen for other choices or parameters, e.g. $\lambda = 40$ and $\mu_1 = \mu_2 = 8$, where the amplitude always increases as α increases.

the corrected energies are explicitly given by

$$\omega_{\pm}^2 = \frac{\lambda^2}{4} + \omega_0^2 \pm \sqrt{\lambda^2 \omega_0^2 + |\alpha|^2} \simeq \begin{cases} \left(\frac{\lambda}{2} \pm \omega_0\right)^2 \pm \frac{|\alpha|^2}{2\lambda\omega_0}, & |\alpha| \ll \lambda\omega_0, \\ \frac{\lambda^2}{4} + \omega_0^2 \pm |\alpha|, & |\alpha| \gg \lambda\omega_0. \end{cases} \quad (5.51)$$

This changes the shape of the oscillatory signal as it depends on the phase accumulation during propagation. In particular, the corrected frequency at large p can be evaluated using the late-time limit, where we can set $k = 0$ for both particles and get

$$2\omega_- = \sqrt{\lambda^2 + 4\mu^2 - 4\sqrt{\lambda^2\mu^2 + |\alpha|^2}} \simeq \begin{cases} \lambda - 2\mu - \frac{|\alpha|^2}{\lambda\mu(\lambda - 2\mu)}, & |\alpha| \ll \lambda\mu, \\ \lambda - \frac{2|\alpha|}{\lambda}, & \lambda\mu \ll |\alpha| \ll \lambda^2. \end{cases} \quad (5.52)$$

Such corrections can be neglected if we insist that

$$|\alpha| \ll \lambda\mu. \quad (5.53)$$

2. PR increases the magnitude for both the non-analytic signal and the resonance background. Comparing η_R in eq. (5.44) with the particle production time from table 1, we have

$$\frac{\lambda^2 - \mu^2}{2\lambda} < -k\eta_c := \frac{\lambda^2 - \mu_{12}^2}{2\lambda}, \quad \frac{\eta_c}{\eta_R} = \sqrt{\frac{\lambda^2 - \mu_{12}^2}{\lambda^2 - \Delta\mu^2}} < 1, \quad (5.54)$$

i.e. particle production always happens after PR. Since there are two propagators with each of them containing two mode functions evaluated at the creation and annihilation times respectively, both the signal and the background are enhanced by a factor \mathcal{A}_R^2 .

Given the smallness of the one-loop signal, an enhancement from PR may be an attractive phenomenological possibility. Unfortunately a quantitative answer cannot be obtained within the spectral decomposition framework, so we leave this direction to future work.

6 Signal Size and Constraints

There are three parameters in the chemical potential model: the chemical potential, λ , the cut-off scale, Λ , and the symmetry breaking coupling, α . The chemical potential gives the maximal energy available for particle creation, and the other two are directly related to the signal strength. The value of λ is related to Λ by eq. (3.2) with $\dot{\phi}_0 \approx (60H)^2$ fixed by

measurements of the CMB power spectrum. Meanwhile, a consistent effective field theory treatment requires that

$$\Lambda > \sqrt{\dot{\phi}_0} \approx 60H. \quad (6.1)$$

This is because there are higher dimension operators with more powers of $(\nabla\phi/\Lambda^2)^2$, which give extra contributions suppressed by $(\dot{\phi}_0/\Lambda^2)^2$ after substituting $\phi = \dot{\phi}_0 t$. Consequently:

$$\lambda := \frac{\dot{\phi}}{\Lambda} < 60. \quad (6.2)$$

For the symmetry breaking coupling, α , the constraints are more subtle. Firstly, there is an experimental bound on the equilateral NG from CMB data. Depending on the shape, it is given by $f_{\text{NL}} < \mathcal{O}(10)$ [43]. Given that the non-analytic signal is small compared to the big analytic background, the f_{NL} constraint on the background will also effectively constrain the size of the signal. Besides this, there are also several constraints from the theory side:

1. **Higher order corrections at one-loop:** These corrections are similar to figure 2 but with more insertions of $\exp(\pm i\delta\phi/\Lambda)$. As has been discussed in section 5.5, the smallness of these corrections require both eqs. (5.53) and (5.48). In later analysis, we will assume that these two conditions are satisfied so that the de Sitter symmetry is not seriously broken.
2. **Corrections to the power spectrum:** Another constraint comes from the correction to the power spectrum:

$$\langle \delta\phi_{\mathbf{k}} \delta\phi'_{\mathbf{k}'} \rangle = \mathcal{P}_\varphi(k) \cdot (2\pi)^3 \delta^3(\mathbf{k} - \mathbf{k}'). \quad (6.3)$$

Such corrections can also be evaluated using the spectral representation, with the tree-level contributions shown in figure 18.

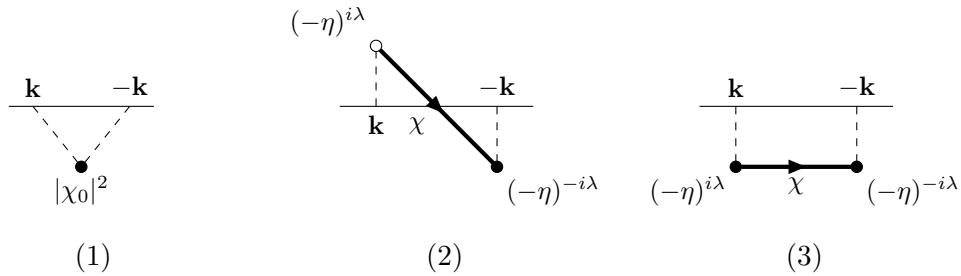


Figure 18. Corrections to the power spectrum at $\mathcal{O}(\alpha^2)$. For each diagram, there is another diagram with opposite vertex types which is omitted here.

Here we quote the crude estimation eq. (F.6) for the corrections to the power spectrum,

and leave their calculation to appendix F:

$$\begin{aligned}
2k^3 \delta \mathcal{P}_\phi^{(1,1\text{-loop})}(\mu_1, \mu_2) &\simeq -\frac{|\alpha|^2}{\Lambda^2} \cdot \frac{\pi}{3\lambda^2} \rho_{\mu_1\mu_2}^{\text{Mink}}(\lambda), \\
2k^3 \delta \mathcal{P}_\phi^{(2,1\text{-loop})}(\mu_1, \mu_2) &\simeq \frac{|\alpha|^2}{\Lambda^2} \cdot \frac{\pi^2}{3\lambda} \rho_{\mu_1\mu_2}^{\text{Mink}}(\lambda), \\
2k^3 \delta \mathcal{P}_\phi^{(3,1\text{-loop})}(\mu_1, \mu_2) &\simeq \frac{|\alpha|^2}{\Lambda^2} \cdot \frac{1}{\lambda^2} \left\{ \frac{\pi}{12} \rho_{\mu_1\mu_2}^{\text{Mink}}(\lambda) + 0.482 \left[\rho_{\mu_1\mu_2}^{\text{Mink}}(\lambda) - \lambda \rho'_{\mu_1\mu_2}(\lambda) \right] \right\}.
\end{aligned} \tag{6.4}$$

Since these corrections are proportional to the zeroth-order $1/2k^3$, as required by scale invariance, they can be regarded as a pure renormalization from an observational point of view. However, there are some other physical effects associated with these corrections:

- Figure 18 (2) produces $\chi_1\chi_2$ -pairs that survive until the end of inflation. If it dominates over the power spectrum from the free field theory, the number density of χ_1, χ_2 will be as large as the one of $\delta\phi$, while the energy density will be $\mathcal{O}(\mu/k\eta)$ larger for each k mode.
- Figure 18 (3) corrects the *sound speed* of the inflaton fluctuations. This follows from the observation that $\delta\chi$ is coupled only to $\delta\phi'$ at the 2-point vertex in eq. (4.8).

To avoid these complications we require that

$$2k^3 \delta \mathcal{P}_\phi^{(1\text{-loop})} \ll 1. \tag{6.5}$$

In figures 19 and 20 we take into account all the theoretical and experimental constraints discussed above. In these plots we compare F_{\min} at $p = 2$ with the maximal signal size from various constraints. We did not consider the signal at larger p since for most values of λ and μ_1, μ_2 we consider, the oscillation is at frequency $\lambda - \mu_{12} \sim \mathcal{O}(10)$ and only requires data from a small range of p to be identified. From the diagrams, we see that with $\lambda \gtrsim 40$, a signal observable with $F_{\min} = 0.01$ is possible within all the constraints. This parameter space could be probed in future 21 cm experiments.

Some further features of these constraints worth noting:

- It turns out that the most stringent constraint comes from the parametric resonance constraint eq. (5.48), which combined with $\Lambda = \dot{\phi}/\lambda$ gives

$$\frac{|\alpha|^2}{\Lambda^2} \lesssim \frac{\lambda^5}{2\pi(60)^2} \approx 4.4 \times 10^{-5} \lambda^5. \tag{6.6}$$

The maximum allowed value of the interaction strength, α , is thus proportional to λ^5 . This explains why the signal size is small for small λ .

- Another important constraint comes from f_{NL} , which becomes increasingly important for large λ . Since the background is larger than the signal, the f_{NL} constraint curve is

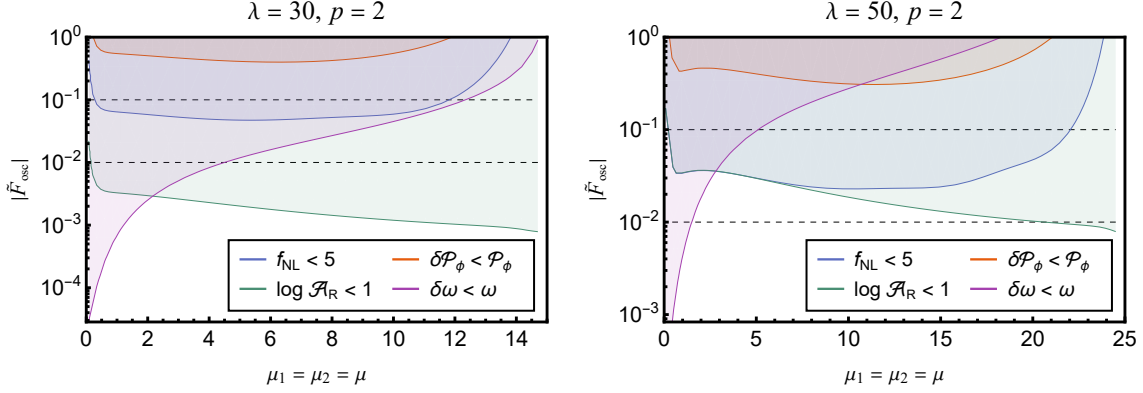


Figure 19. The maximal signal size at $p = 2$ with various constraints. The 4 constraints shown by the shaded regions are (i) $f_{\text{NL}} < 5$ from CMB data [43], (ii) the power spectrum constraint eq. (6.5), (iii) the parametric resonance constraint eq. (5.48) and (iv) the frequency correction constraint eq. (5.53). Note that the last 3 constraints are only to ensure the validity of our calculations and do not imply the breakdown of the theory on their own.

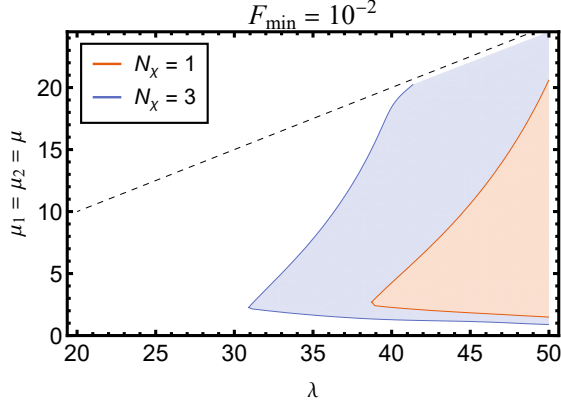


Figure 20. The parameter space for λ and $\mu_1 = \mu_2 = \mu$ assuming the largest α . The shaded regions are allowed by all the 4 constraints. The dashed line is $\lambda = 2\mu$, above which the signal is exponentially suppressed. N_χ is the multiplicity of χ_1 and χ_2 .

roughly proportional to the signal-to-background ratio

$$r_{\text{sbr}} := \lim_{p \rightarrow \infty} \frac{p|\tilde{F}_{\text{osc}}|}{F_{\text{bkg}}} \simeq \sqrt{\frac{\pi}{2}} \frac{\lambda^{5/2}(\mu_1\mu_2)^{1/2}}{\mu_{12}^{5/2}(\lambda - \mu_{12})^{3/2}(\lambda^2 - \Delta\mu^2)^{1/2}}, \quad (6.7)$$

following from eqs. (3.34) and (5.21). For $\mu_1, \mu_2 \sim \mathcal{O}(\lambda)$, $r_{\text{sbr}} \sim \mathcal{O}(\lambda^{-1})$. This explains why the f_{NL} constraint is more stringent at large λ . Note that for a typical point in the parameter region, $r_{\text{sbr}} \sim \mathcal{O}(0.1)$.

Up to this point, we have been considering χ_1, χ_2 as single complex scalars charged under some $U(1)_V$ group. This can easily be promoted to the case where χ_1, χ_2 are \mathbf{N}_χ

and $\overline{\mathbf{N}}_\chi$ multiplets under some non-abelian group. In this case, the bispectrum will be larger by a factor of N_χ , i.e. the constraint curves from parametric resonance eq. (5.48) will be multiplied by N_χ , while the curves from f_{NL} and the power spectrum constraint eq. (6.5) will stay unchanged as both the smooth background and the contribution to the power spectrum are also enhanced by N_χ . In figure 20 we plot the allowed parameter space for $N_\chi = 1, 3$ to illustrate how the added multiplicity can open up new regions of parameter space.

7 Application: Colored Higgs in SUSY Orbifold GUTs

Supersymmetric (SUSY) Grand Unified Theories (GUTs) (for a review, see [50]) provide natural candidates for the pair of charged scalars appearing in the loop. It is well known that SUSY requires the existence of a pair of Higgs doublet chiral superfields (H_u, H_d) with conjugate quantum numbers to give masses to up-type and down-type quarks respectively. At energies above the unification scale, M_U , these Higgses must be embedded into a larger multiplet ($\mathbf{h}_u, \mathbf{h}_d$) to form a representation of the GUT gauge group.

For example, in the simplest SU(5) GUTs, the $\mathbf{h}_{u,d}$ multiplets are in the $\mathbf{5}$ and $\overline{\mathbf{5}}$ representation respectively, which include both the electroweak Higgs and the *colored Higgs* bosons:

$$\mathbf{h}_u = \begin{pmatrix} \chi_u \\ h_u \end{pmatrix}, \quad \mathbf{h}_d = \begin{pmatrix} \chi_d \\ h_d \end{pmatrix}. \quad (7.1)$$

While being far too heavy for direct detection at colliders, these particles may have been produced on-shell during inflation through the chemical potential mechanism and manifest themselves in non-Gaussianities. In particular, since they carry color charge and hypercharge, they can only be pair-produced by the singlet inflaton, and contribute to non-Gaussianities at the one-loop level.

In the minimal supersymmetric SU(5) GUT the unification of gauge couplings predicts $M_U \sim 10^{16}$ GeV, and the masses of the colored Higgs masses are around this scale, which is somewhat higher than the reach of the chemical potential mechanism. Another problem with SUSY GUTs emerges once proton decay is considered: if the colored Higgs bosons obtain their masses through a $\mathbf{h}_u \mathbf{h}_d$ term in the superpotential, they will lead to too rapid proton decay unless their masses are $\mathcal{O}(10)$ times larger than M_U [50].

There is however a well-known variant called *orbifold* SUSY GUTs [35–37] that can naturally avoid the proton decay problem. In these models, the GUT partners are Kaluza-Klein (KK) excitations from a compact extra dimension. The colored Higgs bosons then appear at the lower compactification scale $M_C \sim 10^{14-16}$ GeV [37, 51–53] and become suitable targets for the cosmological collider.

7.1 SUSY inflation and the fifth dimension

In this section we will briefly review the basic setup of SUSY inflation, as well as the extra dimension. For our purposes we will follow the construction in ref. [54, 55] for realizing the

inflaton potential in SUSY. As a phenomenological discussion, we will not attempt to address any deeper origin behind the inflaton potential.

Inflation necessarily breaks SUSY as it is incompatible with the de Sitter isometries. Meanwhile, since the electroweak hierarchy problem suggests a SUSY breaking scale $M_{\text{SUSY}} \gtrsim \text{TeV}$ today, much lower than the Hubble constant $H \sim 10^{14} \text{ GeV}$ during a high-scale inflation, we can think of SUSY as approximately restored at the end of the inflation, i.e. SUSY is *spontaneously broken* by the classical background of the inflaton.

To realize such a scenario, consider an inflaton chiral superfield, Φ , with its scalar component given by

$$\Phi = \frac{\sigma + i\phi}{\sqrt{2}}, \quad (7.2)$$

where ϕ will be the inflaton scalar field, and the other components of Φ are its various superpartners. To main the approximate shift symmetry in ϕ , Φ must appear in the Kähler potential in the combination $\Phi + \bar{\Phi}$. This ensures that ϕ has no potential, even with (spontaneously) broken SUSY. In comparison, the real component σ , called the *sinflaton*, is only massless under when SUSY is unbroken and acquires a mass typically of $\mathcal{O}(H)$ after spontaneous SUSY breaking [55].

We introduce the inflaton slow-roll potential by adding an extra chiral superfield, S , and coupling it to the inflaton through the following superpotential:

$$\mathcal{L} \supset - \int d^2\theta S f(-i\sqrt{2}\Phi) + \text{c.c.} = -F_S f(\phi) + \dots + \text{c.c.}, \quad (7.3)$$

where $f(\phi)$ is some model-dependent holomorphic function. After integrating out F_S , the scalar potential, the expectation value of F_S , and the Hubble constant are related by

$$V_{\text{inf}}(\phi_0) = |\langle F_S \rangle|^2 = |f(\phi_0)|^2 \simeq 3M_{\text{pl}}^2 H^2, \quad (7.4)$$

with $M_{\text{pl}} \gtrsim 4 \times 10^4 H$ from eq. (1.1). Finally, to avoid extra complications due to a light sinflaton, or the scalar component of S (denoted as s), one can make them heavy by including the following term in the Kähler potential:

$$\begin{aligned} \mathcal{L} \supset & - \int d^4\theta \left[\frac{\kappa_\sigma}{2\Lambda^2} |S|^2 (\Phi + \bar{\Phi})^2 + \frac{\kappa_S}{4\Lambda^2} |S|^4 \right] \\ & \supset - \frac{\kappa_\sigma}{\Lambda^2} |F_S|^2 \sigma^2 - \frac{\kappa_S}{\Lambda^2} |F_S|^2 |s|^2. \end{aligned} \quad (7.5)$$

This can gives them masses as large as $\mathcal{O}(M_{\text{pl}} H / \Lambda) \gtrsim \lambda = (60H)^2 / \Lambda$.

Note that for simplification we have considered global supersymmetry only and ignored supergravity corrections. This can be justified because supergravity effects are suppressed by

$1/M_{\text{pl}}^2$, so they can only shift particle masses by [55]

$$\Delta m_{\text{SUGRA}}^2 \sim \frac{V_{\text{inf}}(\phi_0)}{M_{\text{pl}}^2} = \mathcal{O}(H^2). \quad (7.6)$$

This is negligible if all particles we considered are assumed to be heavy compared to H , except for the inflaton, for which the approximate shift symmetry eliminates such contributions.

Particles	Boundary conditions	KK spectrum	$U(1)_R$
h_u, h_d	$(+, +)$	nM_C	0
χ_u, χ_d	$(-, +)$	$(n + 1/2)M_C$	0
h_u^c, h_d^c	$(+, -)$	$(n + 1/2)M_C$	2
χ_u^c, χ_d^c	$(-, -)$	$(n + 1)M_C$	2

Table 3. The boundary conditions, masses and $U(1)_R$ charges for the Higgs bosons in the orbifold SUSY GUT ($n = 0, 1, 2, \dots$). For boundary conditions, plus signs represent essentially Neumann boundary conditions while negative signs represent essentially Dirichlet boundary conditions. The KK spectrum is obtained with a flat 5D geometry.

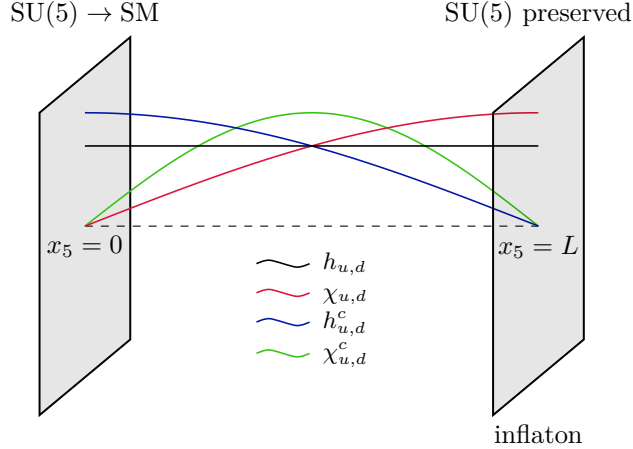


Figure 21. The 5D spacetime with two boundaries in orbifold SUSY GUTs and the 5D profiles of the lightest KK excitations of the Higgs bosons. The left boundary at $x_5 = 0$ breaks $SU(5)$ down to the standard model gauge group, while the right boundary at $x_5 = L$ preserves $SU(5)$ but reduces the 5D $\mathcal{N} = 1$ SUSY down to 4D $\mathcal{N} = 1$ SUSY. The inflaton is chosen to live on the second boundary where $\chi_{u,d}$ have the largest 5D profiles.

In order to couple the inflaton to the colored Higgs bosons in orbifold SUSY GUTs, the extra dimension should also be taken into account. We consider the simplest model in (4+1)D with the extra dimension being an interval of length $L = \pi/M_C$, suggested by [37, 51–53]. In this model, \mathbf{h}_u and \mathbf{h}_d live in the bulk and, together with \mathbf{h}_u^c and \mathbf{h}_d^c , form two hypermultiplets

of the 5D $\mathcal{N} = 1$ SUSY. The boundary conditions at the left endpoint are chosen to break $SU(5)$ down to the standard model gauge symmetry, while the boundary conditions at the right endpoint are chosen to respect the full GUT symmetry, but reduce the 5D $\mathcal{N} = 1$ SUSY down to 4D $\mathcal{N} = 1$ SUSY. The boundary conditions are tabulated in table 3, and illustrated in figure 21. Note that we assume an approximately flat 5D geometry for simplicity, which can easily be generalized to warped 5D geometries if necessary.

While the profile of the inflaton in the extra dimension is unclear, here we discuss a simple possibility that it lives on one of the 4D boundaries as in ref. [38]. To maximize the couplings, we put the inflaton on the right boundary where the 5D profiles of χ_u , and χ_d are their largest. As has been discussed in [38], the inflationary 4D boundary has significant gravitational back-reaction on the 5D geometry if $M_C \lesssim H$, the case one would consider without a chemical potential. Fortunately, the chemical potential allows us to work in the $M_C \gg H$ region, where the back-reaction can be negligible.

7.2 Realizing the chemical potential

In the setup described above it is more natural to write down the chemical potential model in the basis in eq. (3.7). In particular, the $U(1)$ breaking $\chi_u \chi_d$ -term can be implemented via an interaction localized on the boundary

$$S_{U(1)} = - \int_{x_5=L} d^4x \left(\alpha_{5D} \chi_u \chi_d e^{i\phi/\Lambda} + \text{c.c.} \right), \quad (7.7)$$

where α_{5D} is a dimension one coupling. After plugging in the KK decomposition of χ_u and χ_d :

$$\chi_{u,d}(x, x_5) = \sqrt{\frac{2}{L}} \sum_{n=0}^{\infty} \chi_{u,d}^{(n)}(x) \sin \left[\left(n + \frac{1}{2} \right) \frac{\pi x_5}{L} \right], \quad (7.8)$$

we have

$$\mathcal{L}_{U(1)} = - \frac{2\alpha_{5D} M_C}{\pi} \chi_u^{(0)} \chi_d^{(0)} e^{i\phi/\Lambda} + \text{c.c.} + \dots \quad (7.9)$$

When SUSY is taken into account, we consider the supermultiplet $X_{u,d}$ containing $\chi_{u,d}$ as scalar components. It turns out that a term like eq. (7.7) cannot be obtained without breaking SUSY. Combined with the requirement that SUSY breaking be spontaneous during inflation, the naive way to implement the coupling between $\chi_u \chi_d$ and F_S would be to include the following term in the superpotential:

$$\begin{aligned} \mathcal{L}_{U(1)} &= - \int d^2\theta \frac{\kappa_1}{\Lambda_{5D}} X_u X_d S \exp \left(\frac{\sqrt{2}\Phi}{\Lambda} \right) + \text{c.c.} \\ &= - \frac{2\kappa_1}{\pi} \frac{M_C}{\Lambda_{5D}} F_S \chi_u^{(0)} \chi_d^{(0)} e^{i\phi/\Lambda} + \dots + \text{c.c.} \end{aligned} \quad (7.10)$$

This implementation is flawed as it breaks the $U(1)_R$ symmetry of the SUSY GUT theory explicitly, under which θ has +1 charge and the charges of Higgs bosons are listed in ta-

ble 3. This $U(1)_R$ symmetry has been utilized in [51–53] to eliminate dangerous dimension-5 operators that can mediate proton decay.

To fix this, one can consider the Giudice-Masiero mechanism [56], where the interaction now comes from the following term in the Kähler potential:

$$\begin{aligned}\mathcal{L}_{\mathcal{U}(1)} &= - \int d^4\theta \left[\frac{\kappa'_1}{\Lambda_{5D}^3} X_u X_d \bar{S} S \exp\left(\frac{\sqrt{2}\Phi}{\Lambda}\right) + \text{c.c.} \right] \\ &= - \frac{2\kappa'_1}{\pi} \frac{M_C}{\Lambda_{5D}^3} |F_S|^2 \chi_u^{(0)} \chi_d^{(0)} e^{i\phi/\Lambda} + \dots + \text{c.c.}\end{aligned}\quad (7.11)$$

This new Lagrangian renders the $U(1)_R$ breaking spontaneous by $\langle F_S \rangle$ and restores it at the end of the inflation. We now have the following expression for α :

$$\alpha = \frac{2\kappa'_1}{\pi} \frac{M_C |\langle F_S \rangle|^2}{\Lambda_{5D}^3} \lesssim \left(\frac{M_C}{\Lambda_{5D}}\right)^3 \left(\frac{M_{\text{pl}}}{M_C}\right)^2, \quad (7.12)$$

where $M_{\text{pl}} \gtrsim 4 \times 10^4 H$.

There is another way to obtain the chemical potential coupling. We can couple $\chi_u \chi_d$ to $-(\nabla_\mu \phi)^2 \supset \dot{\phi}_0^2 = (60H)^4$ through the following Kähler potential term:

$$\begin{aligned}\mathcal{L}_{\mathcal{U}(1)} &= - \int d^4\theta \left[\frac{\kappa_2}{\Lambda_{5D}^3} X_u X_d (\Phi + \bar{\Phi})^2 \exp\left(\frac{\sqrt{2}\Phi}{\Lambda}\right) + \text{c.c.} \right] \\ &= \frac{2\kappa_2}{\pi} \frac{M_C}{\Lambda_{5D}^3} (\nabla_\mu \phi)^2 \chi_u^{(0)} \chi_d^{(0)} e^{i\phi/\Lambda} + \dots + \text{c.c.}\end{aligned}\quad (7.13)$$

After plugging in $\sigma = 0$ and $\phi = \dot{\phi}_0 t$, we have the following relation

$$\alpha = \frac{2\kappa_2}{\pi} \frac{M_C \dot{\phi}_0^2}{\Lambda_{5D}^3} \lesssim \left(\frac{M_C}{\Lambda_{5D}}\right)^3 \left(\frac{60H}{M_C}\right)^2 (60H)^2. \quad (7.14)$$

In this realization, there are extra couplings between $\chi_u \chi_d$ (or the effective χ_μ) and $\delta\phi$ in addition to those described by eq. (4.8):

$$\delta\mathcal{L}_{\delta\chi}^{(\text{int})} = -\frac{\alpha}{\lambda^2} (-\eta)^{-i\lambda} \left[2(-\eta) \frac{\lambda}{\Lambda} \delta\phi' - \frac{1}{\Lambda^2} (\nabla\delta\phi)^2 \right] e^{i\delta\phi/\Lambda} \delta\chi_\mu + \text{c.c.} \quad (7.15)$$

This will make the parametric dependence somewhat different in the bispectrum.

If we set $\Lambda_{5D} \simeq \Lambda$, and $M_C = 2\mu H$, the upper-bounds on α in both scenarios are higher than the two constraints from eqs. (5.48) and (5.53), sufficient to cover all the parameter region in figure 20 with $N_\chi = 3$. Consequently, a non-analytic signal of order $f_{\text{NL}} \gtrsim \mathcal{O}(0.01)$ can be used to probe these colored Higgs bosons with $M_u = M_d = M_C/2$ lighter than $30H \lesssim 1.5 \times 10^{15} \text{ GeV}$.

8 Discussion and Conclusions

In this paper we have studied the chemical potential mechanism for a pair of charged scalars at the one-loop level. We have shown that the leading-order contribution to the bispectrum can be computed using the de Sitter spectral representation, where one integrates a fictitious tree-level amplitude against the spectral density function. We have demonstrated that the non-analytic signal comes from the threshold limit of the integral with the invariant mass $\mu \simeq \mu_1 + \mu_2$, while there is also a smooth background coming from the resonance limit when $\mu \simeq \lambda$.

In the limit of a large chemical potential, λ , and masses μ_1, μ_2 , both the non-analytic signal and the analytic background have simple forms given by eq. (3.34) and eq. (5.21) respectively. We have that a minimal model can satisfy all constraints, and generate an oscillatory signal in the bispectrum of order $f_{\text{NL}} \gtrsim \mathcal{O}(0.01)$, which could be within the sensitivity of future 21 cm experiments. This mechanism may apply to the colored Higgs bosons in orbifold SUSY GUTs up to $M_u = M_d \lesssim 10^{15}$ GeV.

In this work, we have been considering the exchange of two scalars as a spin-0 multi-particle state. It may be interesting to considering the generalization to nonzero spin exchange. One can consider two heavy particles with spin s_1, s_2 exchanged as a spin- s multi-particle state, where:

$$\mathbf{s} \in \mathbf{s}_1 \oplus \mathbf{s}_2 \oplus \mathbf{j} \quad (8.1)$$

for some $j = 0, 1, 2, \dots$ (the orbital angular momentum). The amplitude is then given by integrating the tree-level amplitude of a spin- s particle times the corresponding spectral density.

Another direction for future work could be relaxing the parametric resonance constraints. The spectral decomposition approach requires treating the breaking of de Sitter isometry down to scale invariance perturbatively. This put very stringent constraints on the coupling α in the scalar model. However, parametric resonance might be desirable as it can induce a provide a large enhancement of the non-analytic signal. Thus, it will be helpful to compute the bispectrum in this regime, and study its phenomenology.

Finally, while our model predicts a striking oscillatory signal, it is accompanied by a large smooth background. It would be interesting to see if some variant of the minimal model can improve the signal-to-background ratio.

Acknowledgments

AB is supported by DOE grant DE-SC-0013642 at the University of Chicago and the Fermi Forward Discovery Group, LLC, under Contract No. 89243024CSC000002 with the DOE Office of Science, Office of High Energy Physics. EB, RS, and ZX are supported by the NSF grant PHY-2210361 and the Maryland Center for Fundamental Physics.

A Integrals and Identities Involving Special Functions

In this appendix, we collect some integrals involving special functions used in the main text and subsequent sections. For $\text{Re } \rho > 0$:

$$e^{-\pi\mu/2} \sqrt{\frac{\pi}{2}} \int_0^{\infty+} x^{\rho-1} e^{ipx} H_{i\mu}^{(1)}(x) dx = \frac{e^{(\rho-1)\pi i/2}}{2^{\rho-1/2}} \mathbf{F}_{i\mu}^\rho(p), \quad p > -1, \quad (\text{A.1})$$

$$e^{-\pi\mu/2} \sqrt{\frac{\pi}{2}} \int_0^{\infty-} x^{\rho-1} e^{ipx} H_{i\mu}^{(1)}(x) dx = \frac{e^{(\rho-1)\pi i/2}}{2^{\rho-1/2}} \mathbf{F}_{i\mu}^\rho(p + i\epsilon), \quad p < -1, \quad (\text{A.2})$$

$$e^{-\pi\mu/2} \sqrt{\frac{\pi}{2}} \int_0^x x^{\rho-1} e^{\pm ix} H_{i\mu}^{(1)}(x) dx = \frac{e^{(\rho-1)\pi i/2}}{2^{\rho-1/2}} \left[\mathbf{G}_{i\mu}^{\rho,\pm}(x) + \mathbf{G}_{-i\mu}^{\rho,\pm}(x) \right]. \quad (\text{A.3})$$

where the function on the RHS of the first two equations is given by

$$\mathbf{F}_{i\mu}^\rho(p) := \Gamma\left(\rho + \frac{i\mu}{2}, \rho - \frac{i\mu}{2}\right) F\left(\rho + \frac{i\mu}{2}, \rho - \frac{i\mu}{2}; \frac{1-p}{2}\right), \quad (\text{A.4})$$

with Γ, F defined as in footnote 7. In the final equation

$$\begin{aligned} \mathbf{G}_{i\mu}^{\rho,\pm}(x) &:= \frac{1}{\rho + i\mu} \Gamma\left(\frac{-2i\mu}{2} - i\mu\right) (-2ix)^{\rho+i\mu} {}_2F_2\left(\frac{1}{2} + i\mu, \rho + i\mu; 1 + 2i\mu, 1 + \rho + i\mu; \pm 2ix\right) \\ &= \frac{(-2ix)^{\rho+i\mu}}{4\pi \sinh \pi\mu} \int_L \frac{(\mp 2ix)^t}{\rho + i\mu + t} \Gamma\left(-t, \frac{1}{2} + i\mu + t\right) dt, \end{aligned} \quad (\text{A.5})$$

where $L : -i\infty \rightarrow i\infty$ is some path separating poles of $\Gamma(-t)$ from other poles of the integrand. The first two equations (A.1) and (A.2) can be derived from eq. (10.43.22) in [49] after Wick rotations (also see the appendices of ref. [22] and [57]). For the second equation, we can first use the following power expansion of $H_{i\mu}^{(1)}(x)$:

$$e^{-\pi\mu/2 \pm ix} H_{i\mu}^{(1)}(x) = -\frac{2i}{\sqrt{\pi}} \left[\Gamma\left(\frac{-2i\mu}{2} - i\mu\right) (-2ix)^{i\mu} \sum_{n=0}^{\infty} \frac{(\frac{1}{2} + i\mu)_n}{(1 + 2i\mu)_n} \frac{(\pm 2ix)^n}{n!} + (\mu \rightarrow -\mu) \right] \quad (\text{A.6})$$

and then integrate term-by-term.

The $\mathbf{F}_{i\mu}^\rho(p)$ in eq. (A.4) also satisfies the following recurrence relation [49, eq. (15.5.19)]:

$$\frac{1}{4}(p^2 - 1) \mathbf{F}_{i\mu}^{2+\rho}(p) - \left(\frac{1}{2} + \rho\right) p \mathbf{F}_{i\mu}^{1+\rho}(p) + (\rho^2 + \mu^2) \mathbf{F}_{i\mu}^\rho(p) = 0. \quad (\text{A.7})$$

This has been used to prove the equivalence of the two forms in eq. (4.23), where the latter form is equivalent to the one in ref. [22].

Finally, to extract the non-analytic piece of the integral over the spectral density, we

made use of the identity [49, eq. (5.13.1)]

$$\int_L \Gamma(a+s)\Gamma(b-s)z^{-s}ds = \Gamma(a+b) \cdot \frac{z^a}{(1+z)^{a+b}}, \quad (\text{A.8})$$

where $L : -i\infty \rightarrow i\infty$ is some path separating the poles of $\Gamma(a+s)$ from the poles of $\Gamma(b-s)$.

B Asymptotic Expansions of $\tilde{\mathbf{F}}_{i\mu}^s(p)$

In eq. (5.23) we split the integrand into two pieces to facilitate use of the residue theorem. In this appendix, we collect identities needed to justify that step. Firstly, the $\tilde{\mathbf{F}}_{i\mu}^s(p)$ defined in eq. (5.24) has the following integral representation [49, eq. (15.6.1)]:

$$\tilde{\mathbf{F}}_{i\mu}^s(p) = \frac{2^{-2i\mu}}{\sqrt{\pi}} \Gamma\left(\frac{1-i\mu}{2}\right) \int_0^1 [t(1-t)]^{-1/2-i\mu} \left(\frac{p-1}{2} + t\right)^{-s} dt. \quad (\text{B.1})$$

In this appendix, we will use this to derive the asymptotic approximation of $\tilde{\mathbf{F}}_{i\mu}^s$ in three limits assuming $p > 1$.

The first limit is when $s = \rho - i\mu$ and $\mu \rightarrow \infty$ with $\text{Im } \mu \geq 0$:

$$2^{2i\mu} \tilde{\mathbf{F}}_{i\mu}^{\rho-i\mu}(p) = \frac{1}{\sqrt{\pi}} \Gamma\left(\frac{1-i\mu}{2}\right) \int_0^1 [t(1-t)]^{-1/2} \left(\frac{p-1}{2} + t\right)^{-\rho} e^{-i\mu g(t;p)} dt, \quad (\text{B.2})$$

where

$$g(t;p) = \log t(1-t) - \log\left(\frac{p-1}{2} + t\right). \quad (\text{B.3})$$

For $p > 1$, $g'(t;p) = 0$ has a unique solution between $(0, 1)$ at

$$t_* = \frac{1}{2} \left(1 - p + \sqrt{p^2 - 1}\right), \quad g''(t_*; p) = -\frac{4}{\sqrt{p^2 - 1} \left(p - \sqrt{p^2 - 1}\right)} < 0. \quad (\text{B.4})$$

Therefore, as $\mu \rightarrow \infty$, the integral above can be approximated as

$$\begin{aligned} 2^{2i\mu} \tilde{\mathbf{F}}_{i\mu}^{\rho-i\mu}(p) &\simeq \frac{e^{\pi i/4}}{\sqrt{\pi}} \Gamma\left(\frac{1-i\mu}{2}\right) \sqrt{\frac{2\pi}{-\mu g''(t_*; p)}} [t_*(1-t_*)]^{-1/2-i\mu} \left(\frac{p-1}{2} + t_*\right)^{-\rho+i\mu} \\ &\simeq \frac{1}{\sqrt{2}} \left(\frac{\sqrt{p^2 - 1}}{2}\right)^{-\rho} \left(p - \sqrt{p^2 - 1}\right)^{-i\mu}. \end{aligned} \quad (\text{B.5})$$

In the main text we use the asymptotic expansion of (B.5) to demonstrate that we can close the contour in the upper half plane.

There are other two limits that will be used to calculate B_{++} in appendix D. The second limit is when $s \rightarrow \infty$, with $\text{Re } s > 0$. In this limit, the integration is dominated by the $t = 0$

boundary:

$$\begin{aligned}
2^{2i\mu} \tilde{\mathbf{F}}_{i\mu}^s(p) &\simeq \frac{1}{\sqrt{\pi}} \Gamma\left(\frac{1-i\mu}{\frac{1}{2}-i\mu}\right) \int_0^\infty t^{-1/2-i\mu} \left(\frac{p-1}{2} + t\right)^{-s} dt \\
&= \frac{1}{\sqrt{\pi}} \Gamma\left(\frac{1-i\mu, -\frac{1}{2}+i\mu+s}{s}\right) \left(\frac{p-1}{2}\right)^{1/2-i\mu-s} \\
&\simeq \frac{\Gamma(1-i\mu)}{\sqrt{\pi}} s^{-1/2+i\mu} \left(\frac{p-1}{2}\right)^{1/2-i\mu-s}.
\end{aligned} \tag{B.6}$$

The third limit is when $|\mu| \rightarrow \infty$ with $\text{Im } \mu \geq 0$:

$$\tilde{\mathbf{F}}_{i\mu}^s(p) = \frac{2^{-2i\mu}}{\sqrt{\pi}} \Gamma\left(\frac{1-i\mu}{\frac{1}{2}-i\mu}\right) \int_0^1 [t(1-t)]^{-1/2} \left(\frac{p-1}{2} + t\right)^{-s} e^{-i\mu h(t)} dt, \tag{B.7}$$

where $h(t) := \log t(1-t)$. In this case:

$$\begin{aligned}
\tilde{\mathbf{F}}_{i\mu}^s(p) &\simeq \frac{2^{-2i\mu} e^{\pi i/4}}{\sqrt{\pi}} \Gamma\left(\frac{1-i\mu}{\frac{1}{2}-i\mu}\right) \sqrt{\frac{2\pi}{-\mu h''(t)}} [t(1-t)]^{-1/2-i\mu} \left(\frac{p-1}{2} + t\right)^{-s} \Big|_{t=1/2} \\
&\simeq \left(\frac{p}{2}\right)^{-s}.
\end{aligned} \tag{B.8}$$

C Spectral Density in Non-relativistic Limit of de Sitter Spacetime

In this section, we will derive eq. (3.21) directly using the non-relativistic limit of de Sitter spacetime without referring to eq. (3.17). To begin with, we first show that the non-relativistic limit of de Sitter spacetime is described by the *quantum inverted harmonic oscillator* with Hamiltonian

$$\mathcal{H} = \frac{\mathbf{P}^2}{2M} - \frac{1}{2} M \mathbf{X}^2. \tag{C.1}$$

The equivalence can either be established at the level of isometry groups or metrics. For a derivation using group contractions readers may refer to ref. [58]. We will take the second approach. We start from the expression for the de Sitter metric in the *static coordinates* with the speed-of-light c restored¹⁵

$$ds^2 = -\left(1 - \frac{R^2}{c^2}\right) c^2 dT^2 + \left(1 - \frac{R^2}{c^2}\right)^{-1} dR^2 + R^2 d\Omega^2. \tag{C.2}$$

¹⁵The coordinate transformation from the static coordinate to the conformal coordinates eq. (2.1) we have been using so far is given by

$$X^i = -\frac{x^i}{\eta}, \quad e^{-T} = \sqrt{\eta^2 - \frac{x^2}{c^2}}.$$

The nontrivial Christoffel symbols are as follows:

$$\Gamma_{RR}^R = -\Gamma_{RT}^T = \frac{R}{c^2} \left(1 - \frac{R^2}{c^2}\right)^{-1}, \quad \Gamma_{TT}^R = -R \left(1 - \frac{R^2}{c^2}\right). \quad (\text{C.3})$$

In the limit $c \rightarrow \infty$, only Γ_{TT}^R survives and the geodesic equation becomes

$$\frac{d^2 X^i}{dT^2} + \Gamma_{TT}^R \hat{R}^i = \frac{d^2 X^i}{dT^2} - X^i = 0, \quad (\text{C.4})$$

which is exactly the Newtonian equation of motion from eq. (C.1).

In the non-relativistic limit, the scalar propagator can be approximated as

$$G_{-+}(X_1, X_2) \simeq \frac{1}{2M} G_{\text{NR}}(\mathbf{X}_1, \mathbf{X}_2, T_1 - T_2) e^{-iMc^2(T_1 - T_2)}, \quad (\text{C.5})$$

where

$$G_{\text{NR}}(\mathbf{X}_1, \mathbf{X}_2, T) := \left(\frac{M}{2\pi i \sinh T} \right)^{3/2} \exp \left\{ \frac{iM}{2 \sinh T} [(\mathbf{X}_1^2 + \mathbf{X}_2^2) \cosh T - 2\mathbf{X}_1 \cdot \mathbf{X}_2] \right\} \quad (\text{C.6})$$

is the propagator of the inverted harmonic oscillator eq. (C.1)¹⁶. Now, we rewrite the spectral decomposition eq. (3.15) using $M \simeq \mu$ as

$$G_{-+}(X_1, X_2; M_1) G_{-+}(X_1, X_2; M_2) \simeq \int_0^\infty \rho_{M_1 M_2}^{\text{dS}}(M) G_{-+}(X_1, X_2; M) dM. \quad (\text{C.7})$$

Given that $G_{-+}(X_1, X_2; M)$ contains the highly oscillatory $e^{-iMc^2(T_1 - T_2)}$ term and $\rho_{M_1 M_2}^{\text{dS}}(M)$ changes rapidly around $M = M_{12} := M_1 + M_2$, we can approximate the integration as

$$\text{RHS} \simeq G_{-+}(X_1, X_2; M_{12}) \int_{-M_{12}}^\infty \rho_{M_1 M_2}^{\text{dS}}(M_{12} + \varepsilon) e^{-i\varepsilon c^2(T_1 - T_2)} d\varepsilon, \quad (\text{C.8})$$

i.e.

$$\begin{aligned} \int_{-M_{12}}^\infty \rho_{M_1 M_2}^{\text{dS}}(M_{12} + \varepsilon) e^{-i\varepsilon c^2 T} d\varepsilon &\simeq \frac{G_{-+}(X_1, X_2; M_1) G_{-+}(X_1, X_2; M_2)}{G_{-+}(X_1, X_2; M_{12})} \Big|_{T_1 - T_2 = T} \\ &= \frac{(2M_{12})}{(2M_1)(2M_2)} \frac{G_{-+}^{\text{NR}}(\mathbf{X}_1, \mathbf{X}_2, T; M_1) G_{-+}^{\text{NR}}(\mathbf{X}_1, \mathbf{X}_2, T; M_2)}{G_{-+}^{\text{NR}}(\mathbf{X}_1, \mathbf{X}_2, T; M_{12})} \end{aligned}$$

¹⁶The readers may be more familiar with the propagator of the quantum harmonic oscillator given by

$$G(\mathbf{X}_1, \mathbf{X}_2, T) := \left(\frac{M\omega}{2\pi i \sin \omega T} \right)^{3/2} \exp \left\{ \frac{iM\omega}{2 \sin \omega T} [(\mathbf{X}_1^2 + \mathbf{X}_2^2) \cos \omega T - 2\mathbf{X}_1 \cdot \mathbf{X}_2] \right\},$$

following from path integral. The propagator of the inverted harmonic oscillator can be obtained in the same manner, or by analytic continuation $\omega \rightarrow iH$, where we have then set $H = 1$.

$$= \frac{e^{-3\pi i/4}}{2^{5/2}\pi^{3/2}} \sqrt{\frac{M_1 M_2}{M_{12}}} (\sinh T)^{-3/2}. \quad (\text{C.9})$$

The spectral density near $M = M_{12}$ can thus be recovered using the inverse Fourier transformation ($c = 1$):

$$\begin{aligned} \rho_{M_1 M_2}^{\text{dS}}(M_{12} + \varepsilon) &\simeq \frac{1}{2^{5/2}\pi^{3/2}} \sqrt{\frac{M_1 M_2}{M_{12}}} \left[e^{-3\pi i/4} \int_0^\infty \frac{dT}{2\pi} (\sinh T)^{-3/2} e^{i\varepsilon T} \right. \\ &\quad \left. + e^{3\pi i/4} \int_{-\infty}^0 \frac{dT}{2\pi} (-\sinh T)^{-3/2} e^{i\varepsilon T} \right] \\ &= \frac{1}{4\pi^{5/2}} \sqrt{\frac{M_1 M_2}{M_{12}}} \left[e^{-3\pi i/4} \int_0^1 \frac{t^{1/2-i\varepsilon} dt}{(1-t^2)^{3/2}} + \text{c.c.} \right] \\ &= \frac{1}{4\pi^3} \sqrt{\frac{M_1 M_2}{M_{12}}} \Gamma\left(\frac{3}{4} + \frac{i\varepsilon}{2}\right) \Gamma\left(\frac{3}{4} - \frac{i\varepsilon}{2}\right) e^{\pi\varepsilon/2}, \end{aligned} \quad (\text{C.10})$$

where the divergence at $T = 0$ cancels between the $T > 0$ and $T < 0$ integral. This agrees with eq. (3.21).

The quantum inverted harmonic oscillator naturally explains why $\rho_{\mu_1 \mu_2}^{\text{dS}}$ does not drop to zero, but is only exponentially suppressed, when $M < M_1 + M_2$. This is because a particle can decay into two particles with a higher total mass by extracting energy from the expanding universe and going through a quantum tunneling process.

D Exact Form of $B_{++,A}$

In this subsection, we provide an analytic evaluation of the integral eq. (4.28) and derive some of its properties. We first complete the x_1 -integral using eq. (A.3):

$$\begin{aligned} \int_0^{x_2} dx_1 \mathcal{I}_{1,++}^{(\pm)}(\lambda; x_1) &= \frac{e^{-\pi i/4} e^{\mp \pi \lambda/2}}{2^{\pm i\lambda}} \left[\mathbf{G}_{i\mu}^{\frac{1}{2} \pm i\lambda, -}(x_2) + \mathbf{G}_{-i\mu}^{\frac{1}{2} \pm i\lambda, -}(x_2) \right], \\ \int_0^{x_2} dx_1 \mathcal{I}_{1,-+}^{(\mp)*}(\lambda; x_1) &= \frac{e^{\pi i/4} e^{\pm \pi \lambda/2}}{2^{\pm i\lambda}} \left[\mathbf{G}_{i\mu}^{\frac{1}{2} \mp i\lambda, +*}(x_2) + \mathbf{G}_{-i\mu}^{\frac{1}{2} \mp i\lambda, +*}(x_2) \right], \end{aligned} \quad (\text{D.1})$$

where $\mathbf{G}_{i\mu}^{\rho, \pm}(x)$ is defined in eq. (A.5) with the contour L shown by the contour L_1 in figure 22. Using the integral representation from eq. (A.5), the x_2 -integration can be evaluated first using eqs. (A.1) and (A.2), leaving

$$B_{++,A}^{(\pm)}(k_1, k_2, k_3) = \frac{i}{8k_1^3 k_2^3} \frac{|\alpha|^2}{\Lambda^3} \frac{\lambda}{\mu [(\lambda^2 - M^2)^2 + 9\lambda^2]} \sum_{n=0}^2 \frac{c_n^\pm}{2^n} \left[\mathbf{H}_{n, i\mu}^{\pm i\lambda}(p) - \mathbf{H}_{n, -i\mu}^{\pm i\lambda}(p) \right], \quad (\text{D.2})$$

where we have used eq. (5.23) and the function $\tilde{\mathbf{F}}_{i\mu}^s(p)$ defined in eq. (5.24) to write

$$\mathbf{H}_{n,i\mu}^{i\lambda}(p) := \frac{1}{2\pi i} \Gamma\left(\frac{1+2i\mu}{\frac{1}{2}+i\mu}\right) \int_L \frac{\tilde{\mathbf{F}}_{i\mu}^{1+n+t}(p) dt}{\frac{1}{2}+i\lambda+i\mu+t} \Gamma\left(\frac{-t, 1+n+t, \frac{1}{2}+i\mu+t}{1+2i\mu+t}\right). \quad (\text{D.3})$$

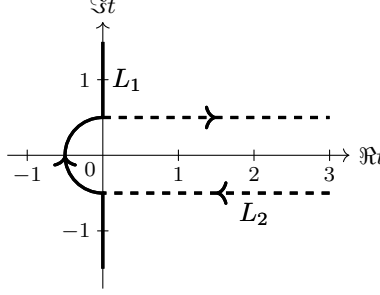


Figure 22. Two contours used to perform the integration in eq. (D.3).

Although the t -integral in eq. (D.3) cannot be evaluated analytically, it can be represented as an infinite sum over the residues of $\Gamma(-t)$ if the path L can be deformed to start and end at $+\infty$, as shown by the contour L_2 in figure 22. To see when such a deformation is allowed, we need the following asymptotic bound on the integrand as $t \rightarrow \infty$ with $\text{Re } t \geq 0$ ¹⁷:

$$\begin{aligned} \frac{\tilde{\mathbf{F}}_{i\mu}^{1+n+t}(p)}{\frac{1}{2}+i\lambda+i\mu+t} \Gamma\left(\frac{-t, 1+n+t, \frac{1}{2}+i\mu+t}{1+2i\mu+t}\right) &\sim t^{-2+n} \left(\frac{p-1}{2}\right)^{-t} \csc \pi t \\ &\lesssim \begin{cases} t^{-2+n} \left(\frac{p-1}{2}\right)^{-t}, & t \rightarrow \pm i\tau + \infty, \\ t^{-2+n} e^{-\pi|t|}, & t \rightarrow \pm i\infty. \end{cases} \end{aligned} \quad (\text{D.4})$$

From this it follows that, for $p > 3$, the integral converges exponentially for L_2 in figure 22 and can be expressed as a sum over the residues of $\Gamma(-t)$:

$$\mathbf{H}_{n,i\mu}^{i\lambda}(p) = \sum_{m=0}^{\infty} \frac{(-)^m (m+1)_n (\frac{1}{2}+i\mu)_m}{(\frac{1}{2}+m+i\lambda+i\mu)(1+2i\mu)_m} \tilde{\mathbf{F}}_{i\mu}^{1+n+m}(p), \quad (p > 3). \quad (\text{D.5})$$

In particular, this shows that $B_{++,A}^{(\pm)}$ are analytic functions at $p \rightarrow \infty$, and in the squeezed limit:

$$B_{++,A}^{(\pm)}(k_1, k_2, k_3) \xrightarrow{p \rightarrow \infty} \frac{3}{8k_1^3 k_2^3} \frac{|\alpha|^2}{\Lambda^3} \frac{\lambda(1 \pm i\lambda)}{\left[\left(\frac{1}{2} \pm i\lambda\right)^2 + \mu^2\right] \left[\left(\lambda^2 - \mu^2 - \frac{9}{4}\right)^2 + 9\lambda^2\right]} p, \quad (\text{D.6})$$

¹⁷For the gamma functions, the asymptotic property $\Gamma(a+t) \sim t^a \Gamma(t)$ and the identity $\Gamma(-t)\Gamma(1+t) = -\pi \csc \pi t$ are used. For $\tilde{\mathbf{F}}_{i\mu}^{1+n+t}(p)$, the asymptotic expansion is given by eq. (B.6) in appendix B.

$$B_{++,A}(k_1, k_2, k_3) := B_{++,A}^{(+)}(k_1, k_2, k_3) + B_{++,A}^{(-)}(k_1, k_2, k_3) \\ \xrightarrow{p \rightarrow \infty} \frac{3}{4k_1^3 k_2^3} \frac{|\alpha|^2}{\Lambda^3} \frac{\lambda(\mu^2 + \frac{1}{4})}{\left[(\lambda^2 - \mu^2 - \frac{1}{4})^2 + \lambda^2\right] \left[(\lambda^2 - \mu^2 - \frac{9}{4})^2 + 9\lambda^2\right]} p. \quad (\text{D.7})$$

On the other hand, eq. (D.4) also shows that the integral always converges exponentially for L_1 in figure 22. Therefore, $\mathbf{H}_{n,i\mu}^{i\lambda}(p)$ can always be evaluated numerically along L_1 . In practice, the contour should be far from all poles of the integrand for numerical stability. We choose the radius of the semicircle in figure 22 to be $1/4$ in our numerical evaluation.

Returning to eq. (D.2), in the limit when both $|\lambda \pm \mu|, \mu \gg 1$, we can approximate $\mathbf{H}_{n,i\mu}^{i\lambda}(p)$ using eq. (B.8) as

$$\mathbf{H}_{n,i\mu}^{i\lambda}(p) \simeq \frac{1}{\frac{1}{2} + i\lambda + i\mu} \cdot \frac{1}{2\pi i} \int_L \left(1 - \frac{t}{\frac{1}{2} + i\lambda + i\mu}\right) \Gamma(-t) \Gamma(1+n+t) 2^{-t} \left(\frac{p}{2}\right)^{-1-n-t} dt \\ = \frac{1}{\frac{1}{2} + i\lambda + i\mu} \left(\frac{p}{2}\right)^{-1-n} \sum_{k=0}^{\infty} \left(1 - \frac{k}{\frac{1}{2} + i\lambda + i\mu}\right) \frac{(n+k)!}{k!} (-p)^{-k} \\ = \frac{1}{\frac{1}{2} + i\lambda + i\mu} \left(\frac{p+1}{2}\right)^{-1-n} \left[n! + \frac{1}{\frac{1}{2} + i\lambda + i\mu} \frac{(n+1)!}{p+1} \right]. \quad (\text{D.8})$$

Therefore:

$$B_{++,A}^{(\pm)}(k_1, k_2, k_3) \simeq \frac{1}{2k_1^3 k_2^3} \frac{|\alpha|^2}{\Lambda^3} \frac{\lambda}{(\lambda^2 - \mu^2)^2 \left[\left(\frac{1}{2} \pm i\lambda\right)^2 + \mu^2\right]} \\ \times \sum_{n=0}^2 \left[n! \mp \frac{2i\lambda}{\lambda^2 - \mu^2} \frac{(n+1)!}{p+1} \right] c_n^{\pm} (p+1)^{-1-n} \\ \simeq \frac{1}{2k_1^3 k_2^3} \frac{|\alpha|^2}{\Lambda^3} \frac{\lambda}{(\lambda^2 - \mu^2)^2 \left[\left(\frac{1}{2} \pm i\lambda\right)^2 + \mu^2\right]} \left[\frac{(1 \pm i\lambda)p^2}{p+1} \right. \\ \left. - \frac{(1 \pm i\lambda)(p+2)Q}{(p+1)^2} - \frac{1}{2} + \frac{2\lambda^2}{\lambda^2 - \mu^2} \frac{1}{(p+1)^2} \left(p^2 - \frac{2Q}{p+1}\right) \right], \quad (\text{D.9})$$

$$B_{++,A}(k_1, k_2, k_3) := B_{++,A}^{(+)}(k_1, k_2, k_3) + B_{++,A}^{(-)}(k_1, k_2, k_3) \\ \simeq \frac{1}{k_1^3 k_2^3} \frac{|\alpha|^2}{\Lambda^3} \frac{\lambda}{(\lambda^2 - \mu^2)^4} \left\{ \frac{\mu^2}{p+1} \left[p^2 - \frac{(p+2)Q}{p+1} \right] + \frac{1}{2} (\lambda^2 - \mu^2) \right. \\ \left. - \frac{2\lambda^2}{(p+1)^2} \left(p^2 - \frac{2Q}{p+1} \right) \right\}. \quad (\text{D.10})$$

This does not agree with eq. (4.33) in its naïve form. However, after summing over permutations of external momenta and using $\mu := \sqrt{M^2 - 9/4} \simeq M$, both expressions are equal

to

$$\begin{aligned}
& B_{++,\text{A}}(k_1, k_2, k_3) + (k_3 \rightarrow k_1, k_2) \\
& \simeq \frac{1}{k_1^3 k_2^3 k_3^3} \frac{|\alpha|^2}{\Lambda^3} \frac{\lambda}{(\lambda^2 - \mu^2)^3} \left[k_1 k_2 k_3 - \frac{k_1^3 + k_2^3 + k_3^3}{2} \right. \\
& \quad \left. + \frac{2(k_1^2 k_2^2 + k_2^2 k_3^2 + k_1^2 k_3^2)}{k_{123}} - \frac{k_1 k_2 k_3 (k_1^2 + k_2^2 + k_3^2)}{k_{123}^2} - \frac{12\lambda^2}{\lambda^2 - \mu^2} \frac{k_1^2 k_2^2 k_3^2}{k_{123}^3} \right]. \tag{D.11}
\end{aligned}$$

This confirms eq. (4.33) as the leading-order approximation of eq. (D.2).

Finally, even for $|\lambda \pm \mu| \sim \mathcal{O}(1)$ with $\mu \gg 1$, eqs. (B.8) and (D.3) still imply that

$$\begin{aligned}
\mathbf{H}_{n,i\mu}^{i\lambda}(p) & \simeq \frac{1}{2\pi i} \int_L \frac{\Gamma(-t)\Gamma(1+n+t)}{\frac{1}{2} + i\lambda + i\mu + t} 2^{-t} \left(\frac{p}{2}\right)^{-1-n-t} dt \\
& = \frac{n!}{\frac{1}{2} + i\lambda + i\mu} \left(\frac{p}{2}\right)^{-1-n} F\left(\begin{matrix} 1+n, \frac{1}{2} + i\lambda + i\mu \\ \frac{3}{2} + i\lambda + i\mu \end{matrix}; -\frac{1}{p}\right), \tag{D.12}
\end{aligned}$$

this allows the corresponding one-loop amplitude being calculated approximately.

E Full Evaluation of the One-loop Model

In this section, we present the full evaluation of the one-loop bispectrum. Section 5.3 has shown that all contributions to the bispectrum can be written as integrations of the following form:

$$F_{X,1\text{-loop}}^{(\pm)}(k_1, k_2, k_3) = \int_{-\infty}^{\infty} \rho_{\mu_1 \mu_2}^{\text{dS}}(\mu) \tilde{F}_X^{(\pm)}(k_1, k_2, k_3; \mu) d\mu + \text{c.c.}, \tag{E.1}$$

where $F_X \in \{F_{-+}, F_{++,\text{NA}}, F_{++,\text{A}}\}$ and

$$\begin{aligned}
\tilde{F}_{-+}^{(\pm)}(k_1, k_2, k_3; \mu) & := \frac{\mathcal{F}}{\sqrt{\pi}} \frac{2^{2i\mu} e^{\mp \pi \lambda}}{\left(\frac{3}{2} \mp i\lambda\right)^2 + \mu^2} \sum_{n=0}^2 \frac{d_n}{2^n} \tilde{\mathbf{F}}_{i\mu}^{-\frac{3}{2}+n \mp i\lambda - i\mu}(p) \\
& \quad \times \Gamma\left(\begin{matrix} i\mu, -\frac{3}{2} + n \mp i\lambda - i\mu, \frac{1}{2} \pm i\lambda + i\mu, \frac{1}{2} \pm i\lambda - i\mu \\ 1 \pm i\lambda \end{matrix}\right), \tag{E.2}
\end{aligned}$$

$$\tilde{F}_{++,\text{NA}}^{(\pm)}(k_1, k_2, k_3; \mu) := i e^{\pi(\pm\lambda - \mu)} \tilde{F}_{-+}^{(\pm)}(k_1, k_2, k_3; \mu), \tag{E.3}$$

$$\begin{aligned}
\tilde{F}_{++,\text{A}}^{(\pm)}(k_1, k_2, k_3; \mu) & := -\frac{i\mathcal{F}}{2} \frac{1}{\mu \left[(\lambda^2 - \mu^2 - \frac{9}{4})^2 + 9\lambda^2 \right]} \sum_{n=0}^2 \frac{c_n^{\pm}}{2^n} \mathbf{H}_{n,i\mu}^{\pm i\lambda}(p) \\
& = -\frac{i\mathcal{F}}{4} \frac{1}{\mu \left[(\lambda^2 - \mu^2 - \frac{9}{4})^2 + 9\lambda^2 \right]} \sum_{n=0}^2 \frac{c_n^{\pm}}{2^n}
\end{aligned}$$

$$\times \sum_{m=0}^{\infty} \frac{(-)^m (m+1)_n \left(\frac{1}{2} + i\mu\right)_m}{\left(\frac{1}{2} + m \pm i\lambda + i\mu\right)(1 + 2i\mu)_m} \tilde{\mathbf{F}}_{i\mu}^{1+n+m}(p). \quad (p > 3) \quad (\text{E.4})$$

Here we have extracted the common factor:

$$\mathcal{F} := \frac{5\lambda^2}{6} \left| \frac{\alpha}{\Lambda} \right|^2 \frac{4}{p^3 + 3\chi^2 p + 4} \quad (\text{E.5})$$

and introduce the following notations:

$$\begin{cases} d_0 := 1, \\ d_1 := p, \\ d_2 := Q, \end{cases} \quad \begin{cases} c_0^\pm := \frac{1}{2} [(1 \pm 2i\lambda)(p^2 - 2Q) - 1], \\ c_1^\pm := \frac{1}{2} p [p^2 - 2(1 \mp i\lambda)Q - 1], \\ c_2^\pm := \frac{1}{2} Q (p^2 - 1), \end{cases} \quad (\text{E.6})$$

where $Q := \frac{1}{4}(p^2 - \chi^2)$. All of these integrations can be expressed as sums over residues at poles with $\text{Im } \mu > 0$. Such poles are summarized in table 2 and table 4. Consequently,

$$F_{1\text{-loop}} = \sum_{\mu_*, s_1 = \pm} \left[\tilde{F}_{-,1\text{-loop}}^{(s_1, \mu_*)} + \tilde{F}_{++,\text{NA},1\text{-loop}}^{(s_1, \mu_*)} + \tilde{F}_{++,\text{A},1\text{-loop}}^{(s_1, \mu_*)} \right] + (k_1 \rightarrow k_2, k_3) + \text{c.c.}, \quad (\text{E.7})$$

where $\mu_* = \pm\lambda, \pm\mu_{12}, \pm\Delta\mu$ are the real parts of the poles and $\tilde{F}_{X,1\text{-loop}}^{(s_1, \mu_*)}$ are the some of residues at these poles.

\tilde{F}	$\text{Re } \mu = \lambda$		$\text{Re } \mu = -\lambda$	
	source	μ	source	μ
$\tilde{F}_{-+}^{(-)}$	$\Gamma\left(\frac{1}{2} - i\lambda + i\mu\right),$ $\Gamma\left(-\frac{3}{2} + n + i\lambda - i\mu\right)$	$\lambda + \left(\frac{1}{2} + k\right)i$	$\frac{1}{(3/2 + i\lambda)^2 + \mu^2}$	$-\lambda + \frac{3}{2}i$
$\tilde{F}_{++,\text{NA}}^{(+)}$	$\frac{1}{(3/2 - i\lambda)^2 + \mu^2}$	$\lambda + \frac{3}{2}i$	$\Gamma\left(\frac{1}{2} + i\lambda + i\mu\right),$ $\Gamma\left(-\frac{3}{2} + n - i\lambda - i\mu\right)$	$-\lambda + \left(\frac{1}{2} + k\right)i$
$\tilde{F}_{++,\text{A}}^{(+)}$	$\frac{1}{(\lambda^2 - \mu^2 - 9/4)^2 + 9\lambda^2}$	$\lambda + \frac{3}{2}i$	$\frac{1}{\frac{1}{2} + m + i\lambda + i\mu},$ $\frac{1}{(\lambda^2 - \mu^2 - 9/4)^2 + 9\lambda^2}$	$-\lambda + \left(\frac{1}{2} + k\right)i$

Table 4. The position of poles of the integrand in eqs. (5.25) and (5.33) over the upper complex- μ plane and their sources ($n = 0, 1, 2$ and $m, k \in \mathbb{N}$). The positions of poles at $\text{Re } \mu = \pm\mu_{12}, \Delta\mu$ are from the spectral density and are the same for all amplitudes, given in table 2. For other amplitudes, e.g. $\tilde{F}_{++,\text{A}}^{(-)}$, the position of poles can be obtained using eq. (4.11).

Assuming $\mu_1 \geq \mu_2$ w.l.o.g., we have the estimation of orders for all 36 terms in table 5 with the Stirling approximation. For $\lambda, \lambda - \mu_{12}, \mu_1, \mu_2$ all much larger than 1, only the following

\tilde{F}	s_1	$\text{Re } \mu$	$\lambda > \mu_{12}$	$\Delta\mu < \lambda < \mu_{12}$	$\lambda < \Delta\mu$
$-+$	$-$	λ	$\mathbf{0}$	$-\pi(\mu_{12} - \lambda)$	$-2\pi(\mu_1 - \lambda)$
		μ_{12}	$\mathbf{0}$	$-2\pi(\mu_{12} - \lambda)$	
		$\Delta\mu$	$-2\pi\mu_2$		$-2\pi(\mu_1 - \lambda)$
		$-\Delta\mu$	$-\pi\mu_{12}$		$-\pi(2\mu_1 - \lambda)$
		$-\mu_{12}$	$-\pi\mu_{12}$	$-\pi(2\mu_{12} - \lambda)$	
		$-\lambda$	$-\pi\lambda$	$-\pi\mu_{12}$	$-\pi(2\mu_1 - \lambda)$
	$+$	any μ_*	$-2\pi\lambda + (\text{the one with } -\mu_* \text{ above})$		
$++$, NA	$+$	$-\lambda$	$\mathbf{0}$	$-\pi(\mu_{12} - \lambda)$	$-2\pi(\mu_1 - \lambda)$
		$-\mu_{12}$	$-\pi(\lambda - \mu_{12})$	$-\pi(\mu_{12} - \lambda)$	
		$-\Delta\mu$	$-\pi(\lambda + 3\mu_2 - \mu_1)$		$-\pi(\mu_{12} - \lambda)$
		$\Delta\mu$	$-\pi(\lambda + 2\mu_1)$		$-\pi(3\mu_1 - \mu_2)$
		μ_{12}	$-\pi(\lambda + 2\mu_{12})$	$-3\pi\mu_{12}$	
		λ	$-3\pi\lambda$	$-\pi(2\lambda + \mu_{12})$	$-\pi(\lambda + 2\mu_1)$
	$-$	any μ_*	$2\pi\mu_* + (\text{the one with } -\mu_* \text{ above})$		
$++$, A	both	$\pm\lambda$	$\mathbf{0}$		
		$\pm\mu_{12}$	$\mathbf{0}^*$		
		$\pm\Delta\mu$	$-2\mu_2$		

Table 5. Estimates of the exponential suppression factors for all contributions to \tilde{F} , assuming $p \gg 1$ and $\mu_1 \geq \mu_2$. For brevity, we only show the exponents of the suppression factors. Note that $\tilde{F}_{++,\text{A}}^{(s_1, s_2 \mu_{12})}$ is polynomially suppressed and is indicated by the * sign.

terms are not exponentially suppressed ($s_1, s_2 = \pm$):

$$\tilde{F}_{-+,1\text{-loop}}^{(-,\mu_{12})}, \quad \tilde{F}_{-+,1\text{-loop}}^{(-,\lambda)}, \quad \tilde{F}_{++,\text{NA},1\text{-loop}}^{(+,-\lambda)}, \quad \tilde{F}_{++,\text{A},1\text{-loop}}^{(s_1, s_2 \lambda)}, \quad \tilde{F}_{++,\text{A},1\text{-loop}}^{(s_1, s_2 \mu_{12})}. \quad (\text{E.8})$$

Among these terms, the non-analytic signal is given by

$$\tilde{F}_{-+,1\text{-loop}}^{(-,\mu_{12})} = \sum_{k=0}^{\infty} \tilde{F}_{-+,1\text{-loop}}^{(-,\mu_{12},k)}, \quad \tilde{F}_{-+,1\text{-loop}}^{(-,\mu_{12},k)} := \tilde{F}_{-+}^{(-)} \left(\mu_{12} + 2ik + \frac{3i}{2} \right) \hat{\rho}_k(\mu_1, \mu_2), \quad (\text{E.9})$$

where

$$\hat{\rho}_k(\mu_1, \mu_2) := 2\pi i \text{Res} \left[\rho_{\sigma_1 \sigma_2}(\mu), \mu_{12} + 2ik + \frac{3i}{2} \right]$$

$$= \frac{(-)^k (2k+1)!!}{2^{k+2} \pi^{5/2} k!} \frac{\prod_{i=1,2,12} \Gamma(-k+i\mu_i) \Gamma(\frac{3}{2}+k-i\mu_i)}{\Gamma(-\frac{3}{2}-2k+i\mu_{12}) \Gamma(\frac{3}{2}+2k-i\mu_{12}) \Gamma(-2k+i\mu_{12}) \Gamma(3+2k-i\mu_{12})}. \quad (\text{E.10})$$

The remaining four terms are all resonance backgrounds. The background terms from \tilde{F}_{-+} are given by

$$\tilde{F}_{-+,1\text{-loop}}^{(-,\lambda)} = \sum_{k=0}^{\infty} \tilde{F}_{-+,1\text{-loop}}^{(-,\lambda,k)} := \sum_{k=0}^{\infty} \tilde{F}_{-+}^{(-,\lambda,k)} \rho_{\mu_1 \mu_2}^{\text{dS}} \left(\lambda + ik + \frac{i}{2} \right), \quad (\text{E.11})$$

$$\tilde{F}_{-+}^{(-,\lambda,k)} := 2\pi i \text{Res} \left[\tilde{F}_{-+}^{(-,\lambda,k)}(\mu), \lambda + ik + \frac{i}{2} \right]. \quad (\text{E.12})$$

where the residues are explicitly given by¹⁸

$$\tilde{F}_{-+}^{(-,\lambda,0)} := -\frac{\sqrt{\pi}\mathcal{F}}{8} \Gamma \left(\frac{1-2i\lambda, -\frac{1}{2}+i\lambda}{2-i\lambda} \right) \frac{2^{2i\lambda} e^{\pi\lambda}}{1+2i\lambda} \left[(1-2i\lambda)p + \frac{c_1^+}{p} \tilde{\mathbf{F}}_{-\frac{1}{2}+i\lambda}^1(p) \right], \quad (\text{E.15})$$

$$\begin{aligned} \tilde{F}_{-+}^{(-,\lambda,1)} &:= -\frac{\sqrt{\pi}\mathcal{F}}{12} \Gamma \left(\frac{2-2i\lambda, -\frac{3}{2}+i\lambda}{1-i\lambda} \right) \frac{2^{2i\lambda} e^{\pi\lambda}}{2i\lambda} \left\{ \frac{\partial}{\partial s} \tilde{\mathbf{F}}_{-\frac{3}{2}+i\lambda-s}^s(p) \Big|_{s=0} \right. \\ &\quad + \sum_{n=1}^2 \frac{d_n}{2^n} \tilde{\mathbf{F}}_{-\frac{3}{2}+i\lambda}^n(p) - \frac{1}{2} \sum_{\epsilon, \epsilon_1, \epsilon_2 = \pm 1} \epsilon \psi \left[\frac{3(1-\epsilon)}{4} + \frac{i}{2} \epsilon (\lambda + \epsilon_1 \mu_1 + \epsilon_2 \mu_2) \right] \\ &\quad \left. + \psi(i\lambda) - \psi(2-2i\lambda) - \frac{1}{1-i\lambda} - \frac{1}{2-i\lambda} + \frac{1}{2i\lambda} - \frac{4}{3} \right\}, \end{aligned} \quad (\text{E.16})$$

$$\begin{aligned} \tilde{F}_{-+}^{(-,\lambda,k \geq 2)} &:= \frac{(-)^k \sqrt{\pi}\mathcal{F}}{2^{2k} k! (k+2)} \Gamma \left(\frac{1+k-2i\lambda, -\frac{1}{2}-k+i\lambda}{1-i\lambda} \right) \\ &\quad \times \frac{2^{2i\lambda} e^{\pi\lambda}}{1-k+2i\lambda} \sum_{n=0}^2 \frac{(n+k-2)! d_n}{2^n} \tilde{\mathbf{F}}_{-\frac{1}{2}-k+i\lambda}^{-1+n+k}(p). \end{aligned} \quad (\text{E.17})$$

¹⁸ $\psi(z) =: \frac{\Gamma'(z)}{\Gamma(z)}$ is the digamma function. The derivative of hypergeometric function in $\tilde{F}_{-+}^{(-,\lambda,1)}$ can be expressed in terms of Meijer-G functions as

$$\begin{aligned} \frac{\partial}{\partial s} \tilde{\mathbf{F}}_{-\frac{3}{2}+i\lambda-s}^s(p) \Big|_{s=0} &= -\frac{\Gamma(4-2i\lambda)}{\Gamma(2-i\lambda)} G_{33}^{22} \left(\begin{matrix} 0, -1+i\lambda; 1 \\ 0, 0; -3+2i\lambda \end{matrix}; \frac{2}{p-1} \right) + \psi(4-2i\lambda) - \psi(2-i\lambda) \\ &= -\log \frac{p}{2} + \frac{1}{2(5-2i\lambda)p^2} + \frac{3}{4(5-2i\lambda)(7-2i\lambda)p^4} + \dots \end{aligned} \quad (\text{E.13})$$

To prove this, one uses the eq. (16.17.2) in [49] to convert

$$G_{33}^{22} \left(\begin{matrix} 0, -1+i\lambda; 1 \\ 0, z; -3+2i\lambda \end{matrix}; \frac{2}{p-1} \right) \quad (\text{E.14})$$

into hypergeometric functions, and then take the limit $z \rightarrow 0$.

The background terms from $\tilde{F}_{++,\text{NA}}$ can be expressed in term of those from \tilde{F}_{-+} as

$$\tilde{F}_{++,\text{NA},1\text{-loop}}^{(+,-\lambda)} = \sum_{k=0}^{\infty} \tilde{F}_{++,\text{NA},1\text{-loop}}^{(+,-\lambda,k)} := \sum_{k=0}^{\infty} \tilde{F}_{++,\text{NA}}^{(+,-\lambda,k)} \rho_{\mu_1\mu_2}^{\text{dS}} \left(-\lambda + ik + \frac{i}{2} \right), \quad (\text{E.18})$$

$$\tilde{F}_{++,\text{NA}}^{(+,-\lambda,k)} = (-)^k e^{2\pi\lambda} \tilde{F}_{-+}^{(+,-\lambda,k)} + \delta_{k1} \cdot \frac{i\pi^{3/2}\mathcal{F}}{12} \Gamma\left(\frac{2+2i\lambda, -\frac{3}{2}-i\lambda}{1+i\lambda} \right) \frac{2^{-2i\lambda} e^{\pi\lambda}}{2i\lambda}, \quad (\text{E.19})$$

where $\tilde{F}_{-+}^{(+,-\lambda,k)}$ is equal to $\tilde{F}_{-+}^{(-,\lambda,k)}$ with λ replaced by $-\lambda$. Finally, the background terms from $\tilde{F}_{++,\text{A}}$ are given by

$$\begin{aligned} \tilde{F}_{++,\text{A},1\text{-loop}}^{(s_1,-s_1\lambda)} &= \sum_{k=0,k \neq 1}^{\infty} \tilde{F}_{++,\text{A}}^{(s_1,-s_1\lambda,k)} \tilde{F}_{++,\text{A},1\text{-loop}}^{(s_1,-s_1\lambda,k)} + \sum_{m=0}^{\infty} \tilde{F}_{++,\text{A},1\text{-loop}}^{(s_1,-s_1\lambda,1,m)} \\ &:= \sum_{k=0,k \neq 1}^{\infty} \tilde{F}_{++,\text{A}}^{(s_1,-s_1\lambda,k)} \rho_{\mu_1\mu_2}^{\text{dS}} \left(-s_1\lambda + ik + \frac{i}{2} \right) \\ &\quad + \sum_{m=0}^{\infty} \tilde{F}_{++,\text{A}}^{(s_1,-s_1\lambda,1,m)} \rho_{\mu_1\mu_2}^{\text{dS}} \left(-s_1\lambda + \frac{3i}{2} \right), \end{aligned} \quad (\text{E.20})$$

$$\tilde{F}_{++,\text{A},1\text{-loop}}^{(s_1,s_1\lambda)} = \sum_{m=0}^{\infty} \tilde{F}_{++,\text{A},1\text{-loop}}^{(s_1,s_1\lambda,m)} := \sum_{m=0}^{\infty} \tilde{F}_{++,\text{A}}^{(s_1,s_1\lambda,m)} \rho_{\mu_1\mu_2}^{\text{dS}} \left(s_1\lambda + \frac{3i}{2} \right), \quad (\text{E.21})$$

$$\tilde{F}_{++,\text{A},1\text{-loop}}^{(s_1,s_2\mu_{12})} = \sum_{k=0}^{\infty} \tilde{F}_{++,\text{A},1\text{-loop}}^{(s_1,s_2\mu_{12},k)} := \sum_{k=0}^{\infty} \tilde{F}_{++,\text{A}}^{(s_1)} \left(s_2\mu_{12} + 2ik + \frac{3i}{2} \right) \hat{\rho}_k(s_2\mu_1, s_2\mu_2), \quad (\text{E.22})$$

where, for $s_1 = +$,

$$\begin{aligned} \tilde{F}_{++,\text{A}}^{(+,-\lambda,k \neq 1)} &:= \frac{2\pi\mathcal{F}}{(k-1)(k+2)} \frac{(-)^k}{(1-k-2i\lambda)(1+2k+2i\lambda)(2+k+2i\lambda)} \\ &\quad \times \frac{(-k-i\lambda)_k}{(-2k-2i\lambda)_k} \sum_{n=0}^2 \frac{(k+1)_n c_n^+}{2^n} \tilde{\mathbf{F}}_{-\frac{1}{2}-k-i\lambda}^{1+n+k}(p), \end{aligned} \quad (\text{E.23})$$

$$\tilde{F}_{++,\text{A}}^{(+,-\lambda,1,m \neq 1)} := \frac{2\pi\mathcal{F}}{3(m-1)} \frac{(-)^m}{2i\lambda(3+2i\lambda)^2} \frac{(-1-i\lambda)_m}{(-2-2i\lambda)_m} \sum_{n=0}^2 \frac{(m+1)_n c_n^+}{2^n} \tilde{\mathbf{F}}_{-\frac{3}{2}-i\lambda}^{1+n+m}(p), \quad (\text{E.24})$$

$$\begin{aligned} \tilde{F}_{++,\text{A}}^{(+,-\lambda,1,1)} &:= \frac{2\pi\mathcal{F}}{3} \frac{1}{2i\lambda(3+2i\lambda)} \left\{ \frac{-1}{3+2i\lambda} \sum_{n=0}^1 \frac{f_n}{2^n(p-1)} \tilde{\mathbf{F}}_{-\frac{3}{2}-i\lambda}^{1+n}(p) \right. \\ &\quad \left. - \frac{1}{2} \sum_{\epsilon, \epsilon_1, \epsilon_2 = \pm 1} \epsilon \psi \left[\frac{3(1-\epsilon)}{4} + \frac{i}{2} \epsilon (-\lambda + \epsilon_1\mu_1 + \epsilon_2\mu_2) \right] \right. \\ &\quad \left. - \frac{2\pi i}{\tanh 2\pi\lambda} + \frac{1}{3+2i\lambda} - \frac{1}{2+i\lambda} - \frac{1}{1+i\lambda} - \frac{1}{2i\lambda} - \frac{1}{3} \right\}, \end{aligned} \quad (\text{E.25})$$

$$\tilde{F}_{++,A}^{(+,\lambda,m)} := \frac{2\pi\mathcal{F}}{3} \frac{(-)^{1+m}}{2i\lambda(3-2i\lambda)^2} \frac{(-1+i\lambda)_m}{(-2+2i\lambda)_m} \sum_{n=0}^2 \frac{(m+1)_n c_n^+}{2^n (-1+m+2i\lambda)} \tilde{\mathbf{F}}_{-\frac{3}{2}+i\lambda}^{1+n+m}(p), \quad (\text{E.26})$$

and

$$\begin{cases} f_0 := p^2 - 2Q, \\ f_1 := 2pQ. \end{cases} \quad (\text{E.27})$$

For $s_1 = -$, one simply replaces all λ with $-\lambda$.

The asymptotic estimation eq. (5.27) implies that the infinite sum over residues is also an series expansion over $1/p$ with the following power-counting rules:

$$\tilde{F}_{-+,1\text{-loop}}^{(-,\mu_{12},k)} \sim \mathcal{O}(p^{-3-2k}), \quad (\text{E.28})$$

$$\tilde{F}_{-+,1\text{-loop}}^{(-,\lambda,k)} \sim \tilde{F}_{++,\text{NA},1\text{-loop}}^{(+,-\lambda,k)} \sim \begin{cases} \mathcal{O}(p^{-2-k}), & k \neq 1, \\ \mathcal{O}(p^{-3} \log p), & k = 1, \end{cases} \quad (\text{E.29})$$

$$\tilde{F}_{++,A,1\text{-loop}}^{(s_1,-s_1\lambda,k)} \sim \mathcal{O}(p^{-2-k}), \quad (\text{E.30})$$

$$\tilde{F}_{++,A,1\text{-loop}}^{(s_1,-s_1\lambda,1,m)} \sim \tilde{F}_{++,A,1\text{-loop}}^{(s_1,s_1\lambda,m)} \sim \mathcal{O}(p^{-2-m}), \quad (\text{E.31})$$

$$\tilde{F}_{++,A,1\text{-loop}}^{(s_1,s_2\mu_{12},k)} \sim \mathcal{O}(p^{-2}). \quad (\text{E.32})$$

For F_{-+} and $F_{-+,\text{NA}}$, the series is convergent for any $p > 1$, while for $F_{++,A}$, the series is at least convergent for $p > 3$ as indicated by eq. (E.4). Note that $\tilde{F}_{++,A,1\text{-loop}}^{(s_1,s_2\mu_{12},k)}$ are $\mathcal{O}(p^{-2})$ for all k . This explains why the difference between the numerical result and the sum over poles does not approach zero in figure 11 at large p .

F Corrections to the Power Spectrum

In this appendix, we evaluate the corrections to the power spectrum by our model. We first evaluate the correction for the tree-level model given by (4.8). At $\mathcal{O}(|\alpha|^2)$, there are three diagrams contributing to the power spectrum as shown in figure 18. The first diagram is simply given by

$$2k^3 \delta \mathcal{P}_\phi^{(1)} = -\frac{2|\chi_0|^2}{\Lambda^2}. \quad (\text{F.1})$$

The second diagram is given by

$$\begin{aligned} 2k^3 \delta \mathcal{P}_\phi^{(2)} &= 2k^3 |\chi_0|^2 \left| e^{-\pi\mu/2} \sqrt{\frac{\pi}{2}} \int_{-\infty+}^0 \frac{d\eta}{\eta^{5/2}} \cdot 2(-\eta)^{1-i\lambda} \frac{\lambda}{\Lambda} \partial_\eta D_-(k, \eta) H_{i\mu}^{(1)}(-k\eta) \right|^2 \\ &\quad + (\lambda \rightarrow -\lambda) + \text{c.c.} \\ &= \frac{2\lambda^2 |\chi_0|^2}{\Lambda} \left| \int_0^{\infty+} \mathcal{I}_{1,-+}^{(-)}(\lambda; x) dx \right|^2 + (\lambda \rightarrow -\lambda) \end{aligned}$$

$$\begin{aligned}
&= \frac{4\lambda^2 |\chi_0|^2 \cosh \pi \lambda}{\Lambda^2} \left| \mathbf{F}_{i\mu}^{\frac{1}{2}-i\lambda}(1) \right|^2 \\
&= \frac{2 |\chi_0|^2}{\Lambda^2} \frac{2\pi \lambda \sinh 2\pi \lambda}{\cosh 2\pi \lambda + \cosh 2\pi \mu},
\end{aligned} \tag{F.2}$$

where $\mathcal{I}_{1,\pm\pm}^{(\pm)}$ is defined by eq. (4.14). Finally, the third diagram can be evaluated in the same manner as in section 4.3, except now we can utilize the symmetry between the two vertices and write

$$\begin{aligned}
2k^3 \delta \mathcal{P}_\phi^{(3)} &= -2k^3 |\chi_0|^2 \int_{-\infty+}^0 \frac{d\eta_2}{\eta_2^4} \int_{-\infty+}^0 \frac{d\eta_1}{\eta_1^4} \cdot 2(-\eta_1)^{1-i\lambda} \frac{\lambda}{\Lambda} \partial_{\eta_1} D_+(k, \eta_1) \\
&\quad \times 2(-\eta_2)^{1+i\lambda} \frac{\lambda}{\Lambda} \partial_{\eta_2} D_+(k, \eta_2) G_{++}(k, \eta_1, \eta_2) + (\lambda \rightarrow -\lambda) + \text{c.c.} \\
&= -\frac{\lambda^2 |\chi_0|^2}{\Lambda^2} \int_0^{\infty+} dx_2 \int_0^{x_2} dx_1 \left[\mathcal{I}_{1,++}^{(-)}(\lambda; x_1) \mathcal{I}_{1,-+}^{(-)*}(\lambda; x_2) + (\lambda \rightarrow -\lambda) \right] + \text{c.c.} \tag{F.3}
\end{aligned}$$

Then, by applying eqs. (A.1) and (A.3), we obtain

$$\begin{aligned}
2k^3 \delta \mathcal{P}_\phi^{(3)} &= \frac{i\lambda^2 |\chi_0|^2}{4\pi\Lambda^2} \frac{e^{\pi\mu}}{\sinh \pi\mu} \int_L \frac{dt}{\frac{1}{2} - i\lambda + i\mu + t} \Gamma\left(-t, 1+t, \frac{1}{2} + i\mu + t\right) \\
&\quad + (\lambda \rightarrow -\lambda, \mu \rightarrow -\mu) + \text{c.c.} \\
&= -\frac{\lambda^2 |\chi_0|^2}{2\Lambda^2} \frac{e^{\pi\mu}}{\sinh \pi\mu} \sum_{n=0}^{\infty} \frac{(-)^n}{\left(\frac{1}{2} + n + i\mu\right) \left(\frac{1}{2} + n - i\lambda + i\mu\right)} \\
&\quad + (\lambda \rightarrow -\lambda, \mu \rightarrow -\mu) + \text{c.c.} \\
&= \frac{i |\chi_0|^2}{\Lambda^2} \frac{\lambda e^{\pi\mu}}{4 \sinh \pi\mu} \left[\psi\left(\frac{1}{4} - \frac{i\lambda - i\mu}{2}\right) - \psi\left(\frac{3}{4} - \frac{i\lambda - i\mu}{2}\right) \right] \\
&\quad + (\lambda \rightarrow -\lambda, \mu \rightarrow -\mu) + \text{c.c.} \tag{F.4}
\end{aligned}$$

Note that a similar calculation without chemical potential has been carried out in ref. [3]. Our results for the second and the third diagrams agree with their expressions in the limit $\lambda \rightarrow 0$.

For the one-loop model, the correction can also be derived from the tree-level one using the Källén–Lehmann representation:

$$\delta \mathcal{P}_\phi^{(1\text{-loop})}(\mu_1, \mu_2) = \int_0^\infty \delta \mathcal{P}_\phi^{(\text{tree})}(\mu) \rho_{\mu_1 \mu_2}^{\text{dS}}(\mu) d\mu. \tag{F.5}$$

For $\lambda, \mu_1, \mu_2, \lambda - \mu_{12} \gg 1$, all three contributions peak around $\mu \simeq \lambda$ and we can expand the

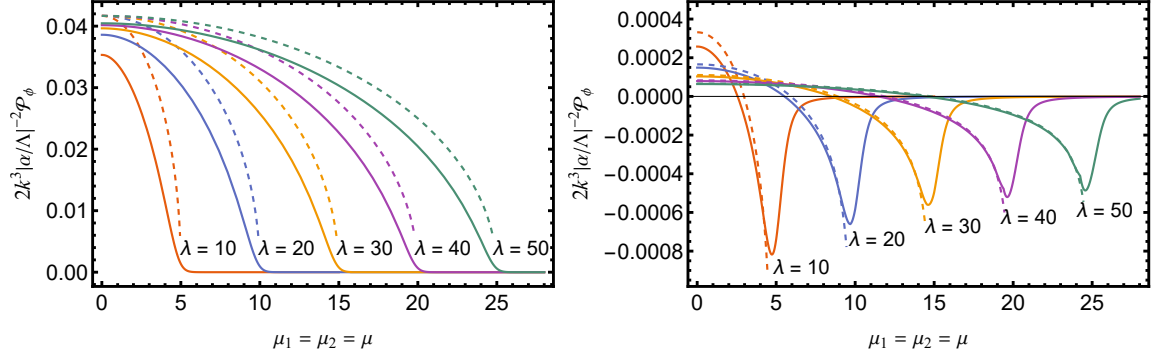


Figure 23. The corrections to the power spectrum in the one-loop model for various λ and $\mu_1 = \mu_2 = \mu$ from $\delta\mathcal{P}_\phi^{(2)}$ (left) and $\delta\mathcal{P}_\phi^{(3)}$ (right). The dashed lines are estimations from eq. (F.6).

integrand around this point, giving:

$$\begin{aligned}
2k^3\delta\mathcal{P}_\phi^{(1,1\text{-loop})}(\mu_1, \mu_2) &\simeq -\frac{|\alpha|^2}{\Lambda^2} \cdot \frac{\pi}{3\lambda^2} \rho_{\mu_1\mu_2}^{\text{Mink}}(\lambda), \\
2k^3\delta\mathcal{P}_\phi^{(2,1\text{-loop})}(\mu_1, \mu_2) &\simeq \frac{|\alpha|^2}{\Lambda^2} \cdot \frac{\pi^2}{3\lambda} \rho_{\mu_1\mu_2}^{\text{Mink}}(\lambda), \\
2k^3\delta\mathcal{P}_\phi^{(3,1\text{-loop})}(\mu_1, \mu_2) &\simeq \frac{|\alpha|^2}{\Lambda^2} \cdot \frac{1}{\lambda^2} \left\{ \frac{\pi}{12} \rho_{\mu_1\mu_2}^{\text{Mink}}(\lambda) + \zeta \left[\rho_{\mu_1\mu_2}^{\text{Mink}}(\lambda) - \lambda \rho_{\mu_1\mu_2}'^{\text{Mink}}(\lambda) \right] \right\},
\end{aligned} \tag{F.6}$$

where

$$\zeta := \frac{1}{4} \int_{-\infty}^{\infty} \frac{-ix \left[\psi\left(\frac{1}{4} + \frac{ix}{2}\right) - \psi\left(\frac{3}{4} + \frac{ix}{2}\right) \right]}{\frac{9}{4} + x^2} dx = 0.482003 \dots \tag{F.7}$$

For a more accurate result, one has to carry out numerical calculations and the results are presented in figure 23 for $\delta\mathcal{P}_\phi^{(2)}$ and $\delta\mathcal{P}_\phi^{(3)}$.

References

- [1] X. Chen and Y. Wang, *Quasi-Single Field Inflation and Non-Gaussianities*, *JCAP* **04** (2010) 027, [[arXiv:0911.3380](#)].
- [2] V. Assassi, D. Baumann, and D. Green, *On Soft Limits of Inflationary Correlation Functions*, *JCAP* **11** (2012) 047, [[arXiv:1204.4207](#)].
- [3] X. Chen and Y. Wang, *Quasi-Single Field Inflation with Large Mass*, *JCAP* **09** (2012) 021, [[arXiv:1205.0160](#)].
- [4] T. Noumi, M. Yamaguchi, and D. Yokoyama, *Effective field theory approach to quasi-single field inflation and effects of heavy fields*, *JHEP* **06** (2013) 051, [[arXiv:1211.1624](#)].
- [5] N. Arkani-Hamed and J. Maldacena, *Cosmological Collider Physics*, [arXiv:1503.08043](#).
- [6] H. Lee, D. Baumann, and G. L. Pimentel, *Non-Gaussianity as a Particle Detector*, *JHEP* **12** (2016) 040, [[arXiv:1607.03735](#)].

- [7] M. Alvarez et al., *Testing Inflation with Large Scale Structure: Connecting Hopes with Reality*, [arXiv:1412.4671](#).
- [8] **SPHEREx** Collaboration, O. Doré et al., *Cosmology with the SPHEREx All-Sky Spectral Survey*, [arXiv:1412.4872](#).
- [9] S. Camera, M. G. Santos, and R. Maartens, *Probing primordial non-Gaussianity with SKA galaxy redshift surveys: a fully relativistic analysis*, *Mon. Not. Roy. Astron. Soc.* **448** (2015), no. 2 1035–1043, [[arXiv:1409.8286](#)]. [Erratum: *Mon. Not. Roy. Astron. Soc.* 467, 1505–1506 (2017)].
- [10] A. Moradinezhad Dizgah and C. Dvorkin, *Scale-Dependent Galaxy Bias from Massive Particles with Spin during Inflation*, *JCAP* **01** (2018) 010, [[arXiv:1708.06473](#)].
- [11] A. Moradinezhad Dizgah, H. Lee, J. B. Muñoz, and C. Dvorkin, *Galaxy Bispectrum from Massive Spinning Particles*, *JCAP* **05** (2018) 013, [[arXiv:1801.07265](#)].
- [12] K. Kogai, K. Akitsu, F. Schmidt, and Y. Urakawa, *Galaxy imaging surveys as spin-sensitive detector for cosmological colliders*, *JCAP* **03** (2021) 060, [[arXiv:2009.05517](#)].
- [13] A. Loeb and M. Zaldarriaga, *Measuring the small-scale power spectrum of cosmic density fluctuations through 21 cm tomography prior to the epoch of structure formation*, *Phys. Rev. Lett.* **92** (2004) 211301, [[astro-ph/0312134](#)].
- [14] J. B. Muñoz, Y. Ali-Haïmoud, and M. Kamionkowski, *Primordial non-gaussianity from the bispectrum of 21-cm fluctuations in the dark ages*, *Phys. Rev. D* **92** (2015), no. 8 083508, [[arXiv:1506.04152](#)].
- [15] P. D. Meerburg, M. Münchmeyer, J. B. Muñoz, and X. Chen, *Prospects for Cosmological Collider Physics*, *JCAP* **03** (2017) 050, [[arXiv:1610.06559](#)].
- [16] **Planck** Collaboration, Y. Akrami et al., *Planck 2018 results. X. Constraints on inflation*, *Astron. Astrophys.* **641** (2020) A10, [[arXiv:1807.06211](#)].
- [17] N. Barnaby, R. Namba, and M. Peloso, *Phenomenology of a Pseudo-Scalar Inflaton: Naturally Large Nongaussianity*, *JCAP* **04** (2011) 009, [[arXiv:1102.4333](#)].
- [18] X. Chen, Y. Wang, and Z.-Z. Xianyu, *Neutrino Signatures in Primordial Non-Gaussianities*, *JHEP* **09** (2018) 022, [[arXiv:1805.02656](#)].
- [19] P. Adshead, L. Pearce, M. Peloso, M. A. Roberts, and L. Sorbo, *Phenomenology of fermion production during axion inflation*, *JCAP* **06** (2018) 020, [[arXiv:1803.04501](#)].
- [20] L.-T. Wang and Z.-Z. Xianyu, *In Search of Large Signals at the Cosmological Collider*, *JHEP* **02** (2020) 044, [[arXiv:1910.12876](#)].
- [21] L.-T. Wang and Z.-Z. Xianyu, *Gauge Boson Signals at the Cosmological Collider*, *JHEP* **11** (2020) 082, [[arXiv:2004.02887](#)].
- [22] A. Bodas, S. Kumar, and R. Sundrum, *The Scalar Chemical Potential in Cosmological Collider Physics*, *JHEP* **02** (2021) 079, [[arXiv:2010.04727](#)].
- [23] X. Tong and Z.-Z. Xianyu, *Large spin-2 signals at the cosmological collider*, *JHEP* **10** (2022) 194, [[arXiv:2203.06349](#)].
- [24] A. Bodas, E. Broadberry, and R. Sundrum, *Grand unification at the cosmological collider with chemical potential*, *JHEP* **01** (2025) 115, [[arXiv:2409.07524](#)].

- [25] X. Chen, Y. Wang, and Z.-Z. Xianyu, *Standard Model Mass Spectrum in Inflationary Universe*, *JHEP* **04** (2017) 058, [[arXiv:1612.08122](#)].
- [26] L.-T. Wang, Z.-Z. Xianyu, and Y.-M. Zhong, *Precision calculation of inflation correlators at one loop*, *JHEP* **02** (2022) 085, [[arXiv:2109.14635](#)].
- [27] D. Marolf and I. A. Morrison, *The IR stability of de Sitter: Loop corrections to scalar propagators*, *Phys. Rev. D* **82** (2010) 105032, [[arXiv:1006.0035](#)].
- [28] Z. Qin and Z.-Z. Xianyu, *Phase information in cosmological collider signals*, *JHEP* **10** (2022) 192, [[arXiv:2205.01692](#)].
- [29] Z.-Z. Xianyu and H. Zhang, *Bootstrapping one-loop inflation correlators with the spectral decomposition*, *JHEP* **04** (2023) 103, [[arXiv:2211.03810](#)].
- [30] T. Cohen, D. Green, and Y. Huang, *Operator origin of anomalous dimensions in de Sitter space*, *Phys. Rev. D* **111** (2025), no. 10 103513, [[arXiv:2407.08581](#)].
- [31] Z. Qin, *Cosmological correlators at the loop level*, *JHEP* **03** (2025) 051, [[arXiv:2411.13636](#)].
- [32] J. C. Pati and A. Salam, *Unified Lepton-Hadron Symmetry and a Gauge Theory of the Basic Interactions*, *Phys. Rev. D* **8** (1973) 1240–1251.
- [33] H. Georgi and S. L. Glashow, *Unity of All Elementary Particle Forces*, *Phys. Rev. Lett.* **32** (1974) 438–441.
- [34] **Particle Data Group** Collaboration, R. L. Workman et al., *Review of Particle Physics*, *PTEP* **2022** (2022) 083C01.
- [35] Y. Kawamura, *Gauge symmetry breaking from extra space $S^{*1}/Z(2)$* , *Prog. Theor. Phys.* **103** (2000) 613–619, [[hep-ph/9902423](#)].
- [36] Y. Kawamura, *Triplet doublet splitting, proton stability and extra dimension*, *Prog. Theor. Phys.* **105** (2001) 999–1006, [[hep-ph/0012125](#)].
- [37] L. J. Hall and Y. Nomura, *Grand unification in higher dimensions*, *Annals Phys.* **306** (2003) 132–156, [[hep-ph/0212134](#)].
- [38] S. Kumar and R. Sundrum, *Seeing Higher-Dimensional Grand Unification In Primordial Non-Gaussianities*, *JHEP* **04** (2019) 120, [[arXiv:1811.11200](#)].
- [39] D. Baumann and D. Green, *Signatures of Supersymmetry from the Early Universe*, *Phys. Rev. D* **85** (2012) 103520, [[arXiv:1109.0292](#)].
- [40] S. Alexander, S. J. Gates, L. Jenks, K. Koutrolikos, and E. McDonough, *Higher Spin Supersymmetry at the Cosmological Collider: Sculpting SUSY Ripples in the CMB*, *JHEP* **10** (2019) 156, [[arXiv:1907.05829](#)].
- [41] J. M. Bardeen, P. J. Steinhardt, and M. S. Turner, *Spontaneous Creation of Almost Scale - Free Density Perturbations in an Inflationary Universe*, *Phys. Rev. D* **28** (1983) 679.
- [42] S. Kumar and R. Sundrum, *Heavy-Lifting of Gauge Theories By Cosmic Inflation*, *JHEP* **05** (2018) 011, [[arXiv:1711.03988](#)].
- [43] **Planck** Collaboration, Y. Akrami et al., *Planck 2018 results. IX. Constraints on primordial non-Gaussianity*, *Astron. Astrophys.* **641** (2020) A9, [[arXiv:1905.05697](#)].

- [44] S. Weinberg, *Quantum contributions to cosmological correlations*, *Phys. Rev. D* **72** (2005) 043514, [[hep-th/0506236](#)].
- [45] J. Bros, H. Epstein, M. Gaudin, U. Moschella, and V. Pasquier, *Triangular invariants, three-point functions and particle stability on the de Sitter universe*, *Commun. Math. Phys.* **295** (2010) 261–288, [[arXiv:0901.4223](#)].
- [46] M. Loparco, J. Penedones, K. Salehi Vaziri, and Z. Sun, *The Källén-Lehmann representation in de Sitter spacetime*, *JHEP* **12** (2023) 159, [[arXiv:2306.00090](#)].
- [47] M. Hogervorst, J. a. Penedones, and K. S. Vaziri, *Towards the non-perturbative cosmological bootstrap*, *JHEP* **02** (2023) 162, [[arXiv:2107.13871](#)].
- [48] P. Creminelli and M. Zaldarriaga, *Single field consistency relation for the 3-point function*, *JCAP* **10** (2004) 006, [[astro-ph/0407059](#)].
- [49] F. Olver, D. Lozier, R. Boisvert, and C. Clark, *The NIST Handbook of Mathematical Functions*. Cambridge University Press, New York, NY, 2010-05-12 00:05:00, 2010.
- [50] R. N. Mohapatra, *Supersymmetric grand unification: An Update*, in *ICTP Summer School in Particle Physics*, pp. 336–394, 6, 1999. [hep-ph/9911272](#).
- [51] L. J. Hall and Y. Nomura, *Gauge unification in higher dimensions*, *Phys. Rev. D* **64** (2001) 055003, [[hep-ph/0103125](#)].
- [52] L. J. Hall and Y. Nomura, *Gauge coupling unification from unified theories in higher dimensions*, *Phys. Rev. D* **65** (2002) 125012, [[hep-ph/0111068](#)].
- [53] L. J. Hall and Y. Nomura, *A Complete theory of grand unification in five-dimensions*, *Phys. Rev. D* **66** (2002) 075004, [[hep-ph/0205067](#)].
- [54] M. Kawasaki, M. Yamaguchi, and T. Yanagida, *Natural chaotic inflation in supergravity*, *Phys. Rev. Lett.* **85** (2000) 3572–3575, [[hep-ph/0004243](#)].
- [55] R. Kallosh, A. Linde, and T. Rube, *General inflaton potentials in supergravity*, *Phys. Rev. D* **83** (2011) 043507, [[arXiv:1011.5945](#)].
- [56] G. F. Giudice and A. Masiero, *A Natural Solution to the μ Problem in Supergravity Theories*, *Phys. Lett. B* **206** (1988) 480–484.
- [57] C. Sleight, *A Mellin Space Approach to Cosmological Correlators*, *JHEP* **01** (2020) 090, [[arXiv:1906.12302](#)].
- [58] H. Bacry and J. Levy-Leblond, *Possible kinematics*, *J. Math. Phys.* **9** (1968) 1605–1614.